



**BIOMASS TORREFACTION UNDER HIGH INTENSITY
ACOUSTIC FIELDS**

DIEGO NEVES KALATALO

**Dissertação de Mestrado
Ciências Mecânicas**

UNIVERSIDADE DE BRASÍLIA

**Faculdade de Tecnologia
Departamento de Engenharia Mecânica**

UNIVERSIDADE DE BRASÍLIA
FACULDADE DE TECNOLOGIA
DEPARTAMENTO DE ENGENHARIA MECÂNICA

BIOMASS TORREFACTION UNDER HIGH INTENSITY
ACOUSTIC FIELDS

DIEGO NEVES KALATALO

Orientador: Carlos Alberto Gurgel Veras, Dr. (ENM/FT/UnB)

Coorientador: Edgar Amaral Silveira, Dr. (ENM/FT/UnB)

DISSERTAÇÃO DE MESTRADO

PUBLICAÇÃO: PCMEC.DM – XXX.AAAA

BRASÍLIA/DF, 28 de fevereiro de 2023

UNIVERSIDADE DE BRASÍLIA
FACULDADE DE TECNOLOGIA
DEPARTAMENTO DE ENGENHARIA MECÂNICA

BIOMASS TORREFACTION UNDER HIGH INTENSITY ACOUSTIC
FIELDS

DIEGO NEVES KALATALO

Dissertação de mestrado submetida ao Departamento de Engenharia Mecânica da Faculdade de Tecnologia da Universidade de Brasília, como parte dos requisitos para obtenção do grau de Mestre em Ciências Mecânicas.

Aprovada por:

Carlos Alberto Gurgel Veras, Dr. (ENM/FT/UnB)
(Orientador)

Fábio Alfaia da Cunha, Dr. (FGA/UnB)
(Examinador Interno)

Cristiane Aparecida Martins, Dr. (ITA)
(Examinador Externo)

Brasília/DF, 28 de fevereiro de 2023

FICHA CATALOGRÁFICA

Kalatalo, D. N.

Biomass Torrefaction Under High Intensity Acoustic Fields

[Distrito Federal] 2023.

xviii, 88p. (ENM/FT/UnB, Mestre, Ciências Mecânicas, 2023.

Dissertação de Mestrado – Universidade de Brasília.

Faculdade de Tecnologia.

Departamento de Engenharia Mecânica.

Palavras-chave:

1. Biomass Energy

2. Acoustic Field

3. Torrefaction

4. Pyrolysis

5. Finite Difference

I. ENM/FT/UnB

II. Título (série)

REFERÊNCIA BIBLIOGRÁFICA

Kalatalo, D. N. (2023). Biomass Torrefaction Under High Intensity Acoustic Fields. Dissertação de Mestrado, Publicação PCMEC.DM – XXX.AAAA, Departamento de Engenharia Mecânica, Universidade de Brasília, Brasília, Distrito Federal, xviii, 88p.

CESSÃO DE DIREITOS

NOME DO AUTOR: Diego Neves Kalatalo

TÍTULO DA DISSERTAÇÃO DE MESTRADO: Biomass Torrefaction Under High Intensity Acoustic Fields

GRAU / ANO: Mestre / 2023

É concedida à Universidade de Brasília, permissão para reproduzir cópias desta dissertação de mestrado e para emprestar ou vender tais cópias somente para propósitos acadêmicos e científicos. O autor reserva outros direitos de publicação e nenhuma parte desta dissertação de mestrado pode ser reproduzida sem a autorização por escrito do autor.

À minha princesa Taís (in memoriam)

ACKNOWLEDGMENTS

Agradeço à minha família, em especial meus pais, minha esposa e filhas, pela convivência, companhia e carinho.

Aos Professores Gurgel e Edgar por terem aceitado acompanhar-me neste projeto. Suas observações e conselhos foram essenciais para minha motivação à medida que as dificuldades iam surgindo.

Ao professor Armando por sua orientação no início do curso e generosidade em aceitar meu pedido de mudança.

Aos amigos de trabalho pela amizade, incentivo e reconhecimento.

Aos meus colegas de curso por partilhar esta jornada e pelo constante apoio e incentivo.

À Universidade de Brasília.

RESUMO

Título: Biomass Torrefaction Under High Intensity Acoustic Fields

Autor: Diego Neves Kalatalo

Orientador: Carlos Alberto Gurgel Veras, Dr. (ENM/FT/UnB)

Coorientador: Edgar Amaral Silveira, Dr. (ENM/FT/UnB)

Programa de Pós-Graduação em Ciências Mecânicas

Brasília, 28 de fevereiro de 2023

A torrefação de biomassa tem grande potencial energético e se apresenta como uma grande oportunidade de ampliar o uso de fontes renováveis de energia. Por meio da torrefação, a biomassa passa por um processo de degradação térmica em baixas temperaturas (200-300 °C). Esse processo consiste em um pré-tratamento para produção de biocarvão de alta qualidade, que pode ser usado para combustão e gaseificação. Partículas de biomassa foram submetidas a um escoamento uniforme, sob a influência de um campo acústico, onde foram simulados os campos de concentração de umidade e temperatura considerando o interior da partícula como volume de controle. Além disso foi simulada a variação da massa da partícula e o traçado do perfil de velocidade e trajetória. Foram observadas mudanças nos coeficientes de transferência de calor e massa, com sua elevação entre 35 a 42 %. O aumento na taxa de secagem alcançou pico de 42% com a variação de frequência e 76% com a variação na velocidade de amplitude. Parâmetros cinéticos foram combinados com modelagem de análise elemental para calcular parâmetros de desempenho, como densificação de massa, densificação de energia, incremento de poder calorífico superior (HHV) e índice de co-benefício massa-energia (EMCI). O projeto de um reator de pirólise utilizando os gases de saída de uma microturbina foi apresentado como aplicação do modelo e sugestão para estudos posteriores.

Palavras-chave: biomass energy, acoustic field, torrefaction, pyrolysis, finite difference.

ABSTRACT

Title: Biomass Torrefaction Under High Intensity Acoustic Fields

Author: Diego Neves Kalatalo

Supervisor: Carlos Alberto Gurgel Veras, Dr. (ENM/FT/UnB)

Co-Supervisor: Edgar Amaral Silveira, Dr. (ENM/FT/UnB)

Graduate Program in Mechanical Sciences

Brasília, February 28th, 2023

Biomass torrefaction has great energy potential and presents a great opportunity to expand the use of renewable energy sources. Through torrefaction, the biomass undergoes a thermal degradation process at low temperatures (200-300 °C). This process consists of a pre-treatment to produce high quality biochar, which can be used for combustion and gasification. Biomass particles were subjected to a uniform flow, under the influence of an acoustic field, where the humidity and temperature concentration fields were simulated considering the interior of the particle as a control volume. In addition, the variation of the particle mass and the tracing of the velocity and trajectory profile were simulated. Changes were observed in the heat and mass transfer coefficients, with their elevation between 35 to 42%. The increase in drying rate peaked at 42% with frequency variation and 76% with amplitude velocity variation. Kinetic parameters were combined with elemental analysis modeling to calculate performance parameters such as mass densification, energy densification, higher calorific value increment (HHV) and mass-energy co-benefit index (EMCI). The design of a pyrolysis reactor using the output gases of a microturbine was presented as a model application and a suggestion for further studies.

Keywords: biomass energy, acoustic field, torrefaction, pyrolysis, finite difference.

SUMMARY

1	INTRODUCTION	1
1.1	Objective	5
1.2	Work structure.....	5
2	THEORY.....	5
2.1	Biomass	5
2.2	Biomass energy conversion	6
2.2.1	Thermochemical conversion	6
2.2.1.1	Combustion.....	7
2.2.1.2	Gasification	7
2.2.1.3	Pyrolysis.....	7
2.2.2	Biochemical conversion	7
2.2.2.1	Fermentation.....	8
2.2.2.2	Anaerobic digestion (AD)	8
2.2.3	Mechanical Extraction	8
2.3	Delimitation of the study range.....	8
2.4	Governing Equations and Boundary Conditions	9
2.4.1	Hydrodynamics	9
2.4.2	Acoustic field.....	10
2.4.3	Balance of forces	10
2.4.4	Particle velocity	11
2.4.5	Particle displacement.....	11
2.4.6	Heat transfer	11
2.4.6.1	Boundary and initial conditions for heat transfer	12
2.4.7	Drying.....	13
2.4.7.1	Boundary and initial conditions for drying.....	14
2.4.8	Transient mass variation	15
2.4.9	Reaction Kinetics	15
2.4.10	Solid composition	17
2.4.11	Performance parameters	19
3	METHODOLOGY	20

3.1	Discretization	20
3.2	Hypotheses	21
3.3	Numerical method.....	21
3.4	Modelling.....	23
3.5	Analyzed biomass.....	23
3.6	Equation-Solving program.....	24
3.7	Simulation parameters	25
3.8	Method verification	25
3.9	Method validation	27
3.10	Simulation conditions	27
4	RESULTS AND DISCUSSION.....	29
4.1	Case 1.....	29
4.2	Case 2.....	44
4.3	Case 3.....	59
4.4	Case 4.....	68
4.5	Design specifications for a torrefaction reactor prototype	79
5	CONCLUSIONS	83
	REFERENCES.....	84

LIST OF FIGURES

Figure 2.1	Drag coefficient for a sphere as a function of Reynolds number.....	10
Figure 2.2	Two-step kinetic model	16
Figure 3.1	Biomass particle radial control volumes, likewise onion layers	21
Figure 3.2	Pyrolysis reactor under acoustic field given by a sound source and storage reservoir	23
Figure 3.3	User interface program for input data	25
Figure 3.4	Comparison of the simulated results for the temperature field as a function of time with those of analytical solution	26
Figure 3.5	System grid sizing checking.....	27
Figure 4.1	Moisture concentration field, Case 1	30
Figure 4.2	Mass transfer coefficient, Case 1, $f = 0 \text{ Hz}$	31
Figure 4.3	Mass transfer coefficient, Case 1, $f = 60 \text{ Hz}$	31
Figure 4.4	Mass transfer coefficient, Case 1, $f = 600 \text{ Hz}$	32
Figure 4.5	Mass transfer coefficient, Case 1, $f = 6000 \text{ Hz}$	32
Figure 4.6	Temperature field, Case 1.....	33
Figure 4.7	Heat transfer coefficient, Case 1, $f = 0 \text{ Hz}$	34
Figure 4.8	Heat transfer coefficient, Case 1, $f = 60 \text{ Hz}$	34
Figure 4.9	Heat transfer coefficient, Case 1, $f = 600 \text{ Hz}$	35
Figure 4.10	Heat transfer coefficient, Case 1, $f = 6000 \text{ Hz}$	35
Figure 4.11	Velocity, Case 1, $f = 0 \text{ Hz}$	36
Figure 4.12	Velocity, Case 1, $f = 60 \text{ Hz}$	37
Figure 4.13	Velocity, Case 1, $f = 600 \text{ Hz}$	37
Figure 4.14	Velocity, Case 1, $f = 6000 \text{ Hz}$	38
Figure 4.15	Vertical displacement, Case 1, $f = 0 \text{ Hz}$	39
Figure 4.16	Vertical displacement, Case 1, $f = 60 \text{ Hz}$	39
Figure 4.17	Vertical displacement, Case 1, $f = 600 \text{ Hz}$	40
Figure 4.18	Vertical displacement, Case 1, $f = 6000 \text{ Hz}$	40
Figure 4.19	Particle yield Y_p , Case 1	41
Figure 4.20	Solid yield Y_s , Case 1, $f = 0 \text{ Hz}$	42
Figure 4.21	Solid yield Y_s , Case 1, $f = 60 \text{ Hz}$	42

Figure 4.22	Solid yield Y_s , Case 1, $f = 600 \text{ Hz}$	43
Figure 4.23	Solid yield Y_s , Case 1, $f = 6000 \text{ Hz}$	43
Figure 4.24	Moisture concentration field, Case 2.....	45
Figure 4.25	Mass transfer coefficient, Case 2, $\tilde{u}_g = 0 \text{ m/s}$	46
Figure 4.26	Mass transfer coefficient, Case 2, $\tilde{u}_g = 10 \text{ m/s}$	46
Figure 4.27	Mass transfer coefficient, Case 2, $\tilde{u}_g = 20 \text{ m/s}$	47
Figure 4.28	Mass transfer coefficient, Case 2, $\tilde{u}_g = 40 \text{ m/s}$	47
Figure 4.29	Temperature field, Case 2.....	48
Figure 4.30	Heat transfer coefficient, Case 2, $\tilde{u}_g = 0 \text{ m/s}$	49
Figure 4.31	Heat transfer coefficient, Case 2, $\tilde{u}_g = 10 \text{ m/s}$	49
Figure 4.32	Heat transfer coefficient, Case 2, $\tilde{u}_g = 20 \text{ m/s}$	50
Figure 4.33	Heat transfer coefficient, Case 2, $\tilde{u}_g = 40 \text{ m/s}$	50
Figure 4.34	Velocity, Case 2, $\tilde{u}_g = 0 \text{ m/s}$	51
Figure 4.35	Velocity, Case 2, $\tilde{u}_g = 10 \text{ m/s}$	52
Figure 4.36	Velocity, Case 2, $\tilde{u}_g = 20 \text{ m/s}$	52
Figure 4.37	Velocity, Case 2, $\tilde{u}_g = 40 \text{ m/s}$	53
Figure 4.38	Vertical displacement, Case 2, $\tilde{u}_g = 0 \text{ m/s}$	54
Figure 4.39	Vertical displacement, Case 2, $\tilde{u}_g = 10 \text{ m/s}$	54
Figure 4.40	Vertical displacement, Case 2, $\tilde{u}_g = 20 \text{ m/s}$	55
Figure 4.41	Vertical displacement, Case 2, $\tilde{u}_g = 40 \text{ m/s}$	55
Figure 4.42	Particle yield Y_p , Case 2.....	56
Figure 4.43	Solid yield Y_s , Case 2, $\tilde{u}_g = 0 \text{ m/s}$	57
Figure 4.44	Solid yield Y_s , Case 2, $\tilde{u}_g = 10 \text{ m/s}$	57
Figure 4.45	Solid yield Y_s , Case 2, $\tilde{u}_g = 20 \text{ m/s}$	58
Figure 4.46	Solid yield Y_s , Case 2, $\tilde{u}_g = 40 \text{ m/s}$	58
Figure 4.47	Moisture concentration field, Case 3.....	60
Figure 4.48	Temperature field, Case 3.....	60
Figure 4.49	Mass transfer coefficient, Case 3.....	61
Figure 4.50	Heat transfer coefficient, Case 3.....	62
Figure 4.51	Velocity, Case 3, $f = 0 \text{ Hz}$	63
Figure 4.52	Vertical displacement, Case 3, $f = 0 \text{ Hz}$	63

Figure 4.53	Velocity, Case 3, $f = 60 \text{ Hz}$	64
Figure 4.54	Vertical displacement, Case 3, $f = 60 \text{ Hz}$	65
Figure 4.55	Particle yield Y_p , Case 3	66
Figure 4.56	Solid yield Y_s , Case 3, $d_p = 50 \mu\text{m}$	67
Figure 4.57	Solid yield Y_s , Case 3, $d_p = 100 \mu\text{m}$	67
Figure 4.58	Solid yield Y_s , Case 3, $d_p = 150 \mu\text{m}$	68
Figure 4.59	Mass transfer coefficient, Case 4	69
Figure 4.60	Heat transfer coefficient, Case 4	70
Figure 4.61	Particle velocity, Case 4	71
Figure 4.62	Vertical displacement, Case 4	72
Figure 4.63	Particle yield Y_p , Case 4	73
Figure 4.64	Solid yield Y_s , Case 4	74
Figure 4.65	Solid product yield Y_i ($i = A, B, C, V1, V2$), Case 4, 0 Hz	75
Figure 4.66	Solid product yield Y_i ($i = A, B, C, V1, V2$), Case 4, 60 Hz	75
Figure 4.67	Solid product composition yield Y_{CHO} , Case 4	76
Figure 4.68	HHV Enhancement Factor EF , Case 4	77
Figure 4.69	Energy Yield EY , Case 4	78
Figure 4.70	Energy-Mass Co-benefit Index $EMCI$, Case 4	79
Figure 4.71	A transport or entrained bed	80

LIST OF TABLES

Table 1.1	Primary Energy Production from firewood in Brazil.	1
Table 1.2	Brazilian Expansion by technology between 2026 and 2030 in installed capacity.	2
Table 1.3	Summary of the studies on isothermal, two-step torrefaction models.	3
Table 2.1	Values of parameters used in the model.	12
Table 2.2	Fitted V_1 and V_2 composition (% mass).	19
Table 3.1	Kinetic parameters for studied biomass.	24
Table 3.2	Ultimate analysis data for studied biomass.	24
Table 3.3	Values of the constant parameters used in the simulation.	28
Table 3.4	Variable parameters used in the torrefaction of a single biomass particle in the presence of the oscillating flow	29
Table 4.1	Observations and effects for case 1	44
Table 4.2	Observations and effects for case 2	59
Table 4.3	Observations and effects for case 3	68
Table 4.4	Comparison of Principal Gas–Solid Contacting Processes	80
Table 4.5	Prototype parameters.	82

LIST OF SYMBOLS

Greek symbols

α	Thermal diffusivity coefficient [$W/m^2 \cdot K$]
δ_r	Radius finite difference between two consecutive mesh points [m]
μ_g	Gas viscosity [$kg/m \cdot s$]
ρ_b	Biomass density [kg/m^3]
ρ_g	Gas density [kg/m^3]
ρ_p	Particle density [kg/m^3]

Latin symbols

a_p	Particle acceleration [m/s^2]
c_g	Speed of sound in the gas [m/s]
c_p	Specific heat capacity [$J/kg \cdot K$]
cp_g	Gas specific heat capacity [$J/kg \cdot K$]
cp_p	Particle specific heat capacity [$J/kg \cdot K$]
d_p	Particle diameter [m]
d_{pore}	Pore diameter [m]
d_r	Reactor diameter [m]
f	Frequency [Hz]
g	Gravitational acceleration [m/s^2]
h_m	Convection mass transfer coefficient [m/s]
h_t	Convection heat transfer coefficient [$W/m^2 \cdot K$]
k	Particle thermal conductivity [$W/m \cdot K$]
k_1	Overall reaction rate of stage 1 [min^{-1}]
k_2	Overall reaction rate of stage 2 [min^{-1}]
k_g	Gas thermal conductivity [$W/m \cdot K$]
k_i	Reaction rate for product i [min^{-1}]
k_n	Thermal conductivity on the n^{th} mesh point [$W/m \cdot K$]
m_0	Initial dry solid biomass [kg]
m_A	Mass of solid A [kg]

m_B	Mass of solid B [kg]
m_C	Mass of solid C [kg]
\dot{m}_b	Mass flow rate of biomass [kg/s]
\dot{m}_g	Mass flow rate of gas [kg/s]
m_p	Particle mass [kg]
m_s	Solid biomass [kg]
m_{V1}	Mass of volatile V1 [kg]
m_{V2}	Mass of volatile V2 [kg]
m_w	Mass of water [kg]
m_w^i	Mass of water for the i^{th} control volume [kg]
t	Time [s]
t_r	Residence time [s]
toe	Tons of oil equivalent [1 J = 2,388458966275X10 ⁻¹¹ toe]
u_0	Initial particle velocity [m/s]
\bar{u}_g	Gas average velocity [m/s]
u_g	Gas velocity [m/s]
u_p	Particle velocity [m/s]
u_r	Relative velocity [m/s]
\tilde{u}_g	Gas amplitude velocity [m/s]
v_i	Control volume for i^{th} mesh point [m ³]
z_0	Initial particle position [m]
A_i	Pre – exponential factor for product i [min ⁻¹]
C	Moisture concentration [kg/m ³]
C_0	Initial moisture concentration [kg/m ³]
C_i	Moisture concentration for the i^{th} control volume [kg/m ³]
C_∞	Bulk moisture concentration of gas flow [kg/m ³]
C_n	Moisture concentration on the n^{th} mesh point [kg/m ³]
C_s	Moisture concentration on the surface [kg/m ³]
CV	Calorific Value [kJ/kg]
D	Mass diffusion coefficient [m ² /s]
D_{AB}	Molecular diffusivity [m ² /s]
D_{eff}	Effective diffusivity [m ² /s]

D_{KA}	<i>Knudsen diffusivity [m²/s]</i>
D_n	<i>Mass diffusion coefficient on the nth mesh point [m²/s]</i>
E_a^i	<i>Activation energy for product i [J/mol]</i>
F_d	<i>Drag force [N]</i>
F_w	<i>Weight force [N]</i>
HHV	<i>Higher Heating Value [MJ/kg]</i>
L_p	<i>Sound pressure level [dB]</i>
M_A	<i>Molar mass of species A [kg/mol]</i>
P_{rms}	<i>Root mean square sound pressure [N/m²]</i>
Q_{sd}	<i>Sensible heat of drying [J/kg]</i>
Q_{ld}	<i>Latent heat of drying [J/kg]</i>
Q_{sp}	<i>Sensible heat of pyrolysis [J/kg]</i>
Q_{lp}	<i>Latent heat of pyrolysis [J/kg]</i>
\dot{Q}	<i>Heat transfer rate [J/s]</i>
R	<i>Universal gas constant [J/mol.K]</i>
T	<i>Temperature [K]</i>
T_0	<i>Initial temperature [K]</i>
T_c	<i>Temperature in celsius degress [C], Temperature in the center [K]</i>
T_∞	<i>Bulk temperature of gas flow [K]</i>
T_n	<i>Temperature on the nth mesh point [K]</i>
T_s	<i>Temperature on the surface [K]</i>

Dimensionless symbols

n	<i>Number of mesh points</i>
p_{char}	<i>Property of char composition</i>
p_{eff}	<i>Effective property</i>
p_{wood}	<i>Property of wood composition</i>
r	<i>Radial direction</i>
A	<i>Pre – exponential factor</i>
AD	<i>Anaerobic Digestion</i>
β	<i>Instantaneous fractional yields for product B</i>
C	<i>Carbon</i>

C_d	<i>Drag coefficient</i>
ε	<i>Overall voidage</i>
<i>EES</i>	<i>Engineering Equation Solver</i>
<i>EF</i>	<i>Enhancement Factor</i>
<i>EMCI</i>	<i>Energy-Mass Co-benefit Index</i>
<i>EY</i>	<i>Energy Yield</i>
γ	<i>Instantaneous fractional yields for product C</i>
<i>H</i>	<i>Hydrogen</i>
<i>Nu</i>	<i>Nusselt number</i>
ν	<i>Instantaneous fractional yields for product V1</i>
<i>O</i>	<i>Oxygen</i>
<i>Pr</i>	<i>Prandtl number</i>
π	<i>Pi number</i>
<i>Re</i>	<i>Reynolds number</i>
<i>RME</i>	<i>Rapeseed Methyl Ester</i>
<i>Sc</i>	<i>Schmidt number</i>
<i>Sh</i>	<i>Sherwood number</i>
Y_i	<i>Mass yield for product i</i>
$Y_{j,i}$	<i>Mass yield for element j of product i</i>
Y_p	<i>Particle yield</i>
Y_s	<i>Solid yield</i>
ζ	<i>Instantaneous fractional yields for product V2</i>

Subscript symbols

0	<i>Initial time</i>
1	<i>Stage 1</i>
2	<i>Stage 2</i>
<i>a</i>	<i>Activation</i>
<i>b</i>	<i>Biomass</i>
<i>bb</i>	<i>Biomass burned</i>
<i>c</i>	<i>Celsius degrees, Center</i>
<i>d</i>	<i>Drag</i>

<i>eff</i>	<i>Effective</i>
<i>g</i>	<i>Gas</i>
<i>i</i>	<i>ith index, Product i</i>
<i>ld</i>	<i>Latent heat of drying</i>
<i>lp</i>	<i>Latent heat of pyrolysis</i>
<i>m</i>	<i>Mass</i>
<i>n</i>	<i>nth index</i>
<i>p</i>	<i>Particle, Pressure</i>
<i>pore</i>	<i>Porous medium</i>
<i>r</i>	<i>Radius, Relative, Reactor</i>
<i>rms</i>	<i>Root mean square</i>
<i>s</i>	<i>Solid</i>
<i>sd</i>	<i>Sensible heat of drying</i>
<i>sp</i>	<i>Sensible heat of pyrolysis</i>
<i>t</i>	<i>Thermal</i>
<i>v</i>	<i>Vaporization</i>
<i>w</i>	<i>Water, Weight</i>
<i>A</i>	<i>Solid A, Species A</i>
<i>AB</i>	<i>Couple of gases A and B</i>
<i>B</i>	<i>Solid B</i>
<i>C</i>	<i>Solid C</i>
∞	<i>Bulk referential</i>
<i>KA</i>	<i>Knudsen diffusivity for gas A</i>
<i>V1</i>	<i>Volatile V1</i>
<i>V2</i>	<i>Volatile V2</i>

Superscript symbols

<i>i</i>	<i>ith index, product i</i>
----------	--

1 INTRODUCTION

The generation of mechanically processed wood residue corresponds to a 45% loss in log processing, while pulp and paper mills produce 48% of waste in their production process [1]. Such waste is a threat in manufacturing industries, considering its flammable nature. Furthermore, it is bulky in nature and occupies a lot of space causing a serious environmental pollution.

The use of waste wood is one such method to potentially reduce fossil-based energy dependence. However, raw biomass fuel properties are generally poor and unpredictable, thus requiring pretreatment to maximize their energy potentials.

From 2012 to 2021, the primary production of energy from firewood in Brazil corresponds to an average value of 25.067×10^3 tons of oil equivalent (toe) as we can see in Table 1.1. This production can be compensated from the processing of wood biomass residues.

Table 1.1 – Primary Energy Production from firewood in Brazil.

FONTES	2012	2013	2014	2015	2016	2017	2018	2019	2020	2021	10 ³ tep (toe) SOURCES
NÃO RENOVÁVEL	140.573	139.997	153.920	165.795	172.540	179.478	178.417	192.643	202.917	203.660	NON-RENEWABLE ENERGY
PETRÓLEO	107.258	104.762	116.705	126.127	130.373	135.907	134.067	144.303	152.635	150.386	PETROLEUM
GÁS NATURAL	25.574	27.969	31.661	34.871	37.610	39.810	40.560	44.398	46.299	48.462	NATURAL GAS
CARVÃO VAPOR	2.517	3.298	3.059	2.459	2.636	1.931	1.930	2.162	2.085	2.640	STEAM COAL
CARVÃO METALÚRGICO	0	0	0	0	0	0	0	0	0	0	METALLURGICAL COAL
URÂNIO (U ₃ O ₈)	3.881	2.375	681	512	0	0	0	0	206	343	URANIUM - U ₃ O ₈
OUTRAS NÃO RENOVÁVEIS	1.343	1.592	1.814	1.826	1.921	1.831	1.860	1.780	1.693	1.829	OTHER NON-RENEWABLE
RENOVÁVEL	116.462	118.217	118.788	120.579	122.256	123.546	129.693	133.530	138.518	132.890	RENEWABLE ENERGY
ENERGIA HIDRÁULICA	35.719	33.625	32.116	30.938	32.758	31.898	33.452	34.217	34.089	31.202	HYDRAULIC
LENHA	25.683	24.580	24.936	24.900	23.095	24.423	25.527	25.725	25.710	26.083	FIREWOOD
PRODUTOS DA CANA-DE-AÇÚCAR	45.117	49.306	49.273	50.424	50.658	49.725	50.895	52.861	55.597	49.423	SUGAR CANE PRODUCTS
EÓLICA	434	566	1.050	1.860	2.880	3.644	4.169	4.815	4.906	6.217	WIND
SOLAR	0	0	1	5	7	72	298	572	924	1.441	SOLAR
OUTRAS RENOVÁVEIS	9.508	10.139	11.412	12.453	12.857	13.784	15.353	15.339	17.291	18.525	OTHER RENEWABLE
TOTAL	257.035	258.213	272.708	286.375	294.796	303.024	308.110	326.173	341.436	336.549	TOTAL

Source: Brazilian Energy Balance 2022 [2].

This proposal is in line with the Brazilian Ten-Year Energy Expansion Plan (PDE30), which contemplates the expansion of energy sources by encouraging the use of generation technologies, with emphasis on biomass, urban solid waste and

modernization of a coal plant, indicated as a policy energetic. The result of the final expansion configuration is shown in Table 1.2.

Table 1.2 – Brazilian Expansion by technology between 2026 and 2030 in installed capacity.

Fontes:	2026	2027	2028	2029	2030	Total (MW)
Hidrelétrica ⁽¹⁾⁽²⁾	593	854	1189	1384	313	4333
PCH/CGH	300	300	300	300	300	1500
Biomassa	80	80	80	80	80	400
Resíduos Sólidos Urbanos	12	12	12	12	12	60
Eólica	2375	2375	2375	2375	2375	11875
Fotovoltaica	731	731	731	731	731	3657
UTE Flexível	3082	3117	2135	2000	2000	12334
Modernização Carvão	-	-	350	-	-	350
Resposta da Demanda	200	400	500	600	700	2400
Total:	7373	7869	7672	7483	6512	36908

Source: Brazilian-Year Energy Expansion Plan (PDE30) [3].

The utilization of biomass waste by converting to biochar is an efficient and environmentally friendly way of biomass treating. Biochar is produced from biomass by low temperature pyrolysis.

Pyrolysis can benefit from the association of acoustic fields during the devolatilization process. The acoustic oscillations enhance the heat and mass transfer processes in a fuel bed as noticed by Ref. [4].

One way of enhancing the combustion rate of coal particles is to increase the relative (slip) velocity between the particles and the gas. This effect can be achieved by applying a high frequency, high intensity acoustic field. The increased slip velocity leads to an increased diffusion to the surface and an increased rate of convective heat transfer [5].

Ha et al. [6] investigated analytically the effects of high intensity acoustic fields on the heat and mass transfer around a spherical particle using a two-dimensional, unsteady computer code. They obtained oscillating velocity profile, temperature field, space and time-averaged Nusselt and Sherwood numbers as a function of steady Reynolds number, acoustic Reynolds number and Strouhal number.

The hydrodynamic and thermal characteristics of an oscillating flow created by an acoustic field over a single particle are studied by solving the unsteady and one-dimensional axisymmetric conservation equations.

To investigate the qualitative effects of high intensity acoustic fields on the biomass particles degradation, simulations were performed with the sound frequencies

of 0-6000 Hz. The temperature, moisture concentration, velocity, displacement and kinetic performance parameters in the presence of acoustic fields are compared to those obtained with no acoustic fields.

For simulation of heat and mass transfer without chemical reactions (i.e., drying phase), the species and energy conservation equations are decoupled, and therefore the solution of the thermal diffusion equation and Fick's 2nd order law equation with its boundary conditions.

Devolatilization process has received substantial interest from both researchers and industries because of its potential to improve the biomass properties to a level comparable with coal [7, 8].

During the process of thermal degradation, several chemical reactions occur that contribute to the polymerization of the constituent molecules of the biomass. These events result in profound changes in physical and chemical properties. Several experimental [9-12] and numerical [13-21] studies were carried out in an effort to contribute to the production of information and knowledge that would help to accurately describe the effects derived from biomass pyrolysis.

Lin et al., 2019 [18] compiled reaction kinetics studies for different types of biomasses, considering the assumptions of isothermal and non-isothermal pyrolysis for single-step or multiple-step reaction models. Among the pioneering studies, it is worth mentioning the one proposed by Di Blasi and Lanzetta. [22]. This study was renowned for accurately determining the kinetics of isothermal degradation of biomass. The evolution of solids and volatile fractions are described according to the concept of pseudo-components that coexist and are in continuous change in relation to the composition of the residual biomass. Table 1.3 summarizes the existing works applying the two-step kinetic model for different feedstocks, experimental conditions, and pseudo-component description.

Table 1.3 – Summary of the studies on isothermal, two-step torrefaction models.

Feedstock	Equipment	Experimental condition	Pseudo-components description	Reference
Fir	Mettler Toledo 188 TGA/SDTA 851	Sample weight: 10 mg Temperature: 250-300 °C Heating: 40 °C.min ⁻¹ N ₂ flow: 20 ml.min ⁻¹	Kinetic data	[23]
Beech, Willow Larch Straw	Perkin-Elmer Pyris 6 TG./Varian Micro GC with a Poraplot Q	Particle size: 0.7-2.0 mm Sample weight: 2-10 mg Temperature: 230-300 °C Heating: 10-100 °C.min ⁻¹ N ₂ flow: 20 ml.(STP).min ⁻¹	Solid yield prediction	[24, 25]

Palm shell Fruit bunches	TG Q50, Instruments	TA	Particle size: 0.25 mm Sample weight: 10 mg Temperature: 200-300 °C Heating: 25-50 °C.min ⁻¹ N ₂ flow: 100 ml.min ⁻¹	Solid yield prediction	[26]
Spruce Birch	SDT Q600 Instruments	TGA, TA	Particle size: 0.125 mm Sample weight: 10 mg Temperature: 220-300 °C N ₂ flow: 100 ml/min	Solid yield prediction	[27]
Spruce Pine Aspen Miscanthus	SDT Q600 Instruments	TGA, TA	Sample weight: 8-12 mg Temperature: 240-280 °C Heating rate: 20 °C.min ⁻¹ N ₂ flow: 100 N ml.min ⁻¹	Solid yield prediction	[28, 29]
Pine	TG 209 NETZSCH	F3,	Particle size: 0.09 mm Sample weight: 5 mg Temperature: 250-300 °C Heating: 10-50 °C.min ⁻¹ N ₂ flow: 40 cm ³ min ⁻¹	Solid yield and its elemental composition prediction	[30]
Wheat straw	TGA/DSC – STA 409, NETZSCH		Particle size: 0.09 mm Sample weight: 10 mg Temperature: 250-300 °C Heating: 10 °C.min ⁻¹ Argon flow: 50 cm ³ .min ⁻¹	Solid yield prediction and its pseudo-component distribution	[31]
Beech Wheat Willow	Experimental from [24, 30, 31]	data	Experimental conditions from [24, 30, 31]	Solid yield prediction and its pseudo-component distribution	[32]
Sewage sludge	TGA 2050, Instruments	TA	Sample weight: 10 mg Temperature: 220-300 °C Heating: 10 °C.min ⁻¹ N ₂ flow: 100 ml.min ⁻¹	Solid yield prediction and its pseudo-component Distribution	[33]
Willow	Experimental from [24, 25]	data	Experimental conditions from [24, 25]	Solid yield and its elemental composition prediction. Volatile yield and its composition prediction.	[21]
Eucalyptus Grandis	SDT Q600 TGA, TA Instruments Thermo scientific TGA/FTIR		Particle size: 0.25 mm Sample weight: 15 mg Temperature: 210-300 °C Heating: 5 °C.min ⁻¹ N ₂ flow: 50 ml.min ⁻¹	Solid yield and its elemental composition prediction. Volatile yield and its elemental composition prediction. Solid and Volatile products distribution	[34]

The ultimate analysis data and the kinetic rates enabled the determination of the carbon, hydrogen, and oxygen dynamics [18]. The predicted elemental composition enabled the calculation of the devolatilization (solid yield), higher heating values (HHV's), and the HHV enhancement factor (EF) evolution during the treatment [14].

From an industrial point of view, the ideal energy aspect is to obtain a high energy yield at a low solid volume (higher mass losses), dispending less energy during the pre-treatment process [35]. Lu et al. [35] determined an energy-mass co-benefit index (EMCI) that means the difference between the energy yield and the solid yield.

This INDEX was defined to seek the optimum condition operation between torrefaction treatments where a higher EMCI represents a better treatment to be applied to the raw material [35].

1.1 Objective

The objective of this work is to numerically simulate the biomass torrefaction under high intensity acoustic fields, considering heat transfer, mass transfer, elemental analysis and a kinetic model of pyrolysis reactions. Finally, a device design will be proposed to perform the model simulations. The model is going to be validated by comparing numerical to experimental data obtained from a thermogravimetric analysis.

1.2 Work Structure

Chapter 2 presents the background theory that describe biomass, kinds of biomass energy conversion, the hydrodynamic aspects of an acoustic flow, heat and mass transport in a spherical particle as well the description of the biomass solid yields, energy yields, performance parameters and its reaction kinetics. Chapter 3 presents the methodology to solve the model. A brief description of the finite difference method is covered to provide relevant details of the numerical model. Chapter 4 provides the comparison of the model with analytical data, results of the numerical simulation for variable parameters, and a device proposed for practical application. Chapter 5 presents the conclusions and provides suggestions for further work.

2 THEORY

2.1 Biomass

Biomass is available in a wide range of resources such as waste streams, woody and grassy materials and energy crops. Woody materials are preferred above food crops, because of several reasons. Woody materials contains much more energy than food crops, the number of fertilizers and pesticides necessary for wood is much lower and the production of woody materials is much higher than for food crops which means that the land use becomes smaller.

Another characteristic of biomass is its climate neutral behavior. If biomass is grown in a sustainable way, its production and application produce no net amount of CO₂ in the atmosphere. The CO₂ released by the application of biomass is stored in

the biomass resource during photosynthesis and is extracted from the atmosphere which means a climate neutral carbon cycle of CO₂.

2.2 Biomass energy conversion

The conversion of biomass into energy comprises different types and sources of raw material, conversion options, end-use applications and infrastructure requirements.

The use of biomass to produce energy is an important renewable source of resources, which can be used to reduce the impact of energy production and use on the environment. As with any energy resource, there are limitations in its use and applicability. Its use should compete not only with fossil fuels, but also with other renewable energy sources such as wind, solar and wave power.

Biomass can be converted into useful forms of energy using different processes. The factors that influence the choice of the conversion process are: the type and quantity of biomass raw material; the desired form of energy, i.e., end-use requirements; environmental standards; economic conditions; and project specific factors. In many situations it is the way energy is required that determines the process route, followed by the available types and quantities of biomass.

Biomass can be converted into three main products: two energy-related products — power/heat generation and transport fuels — and one as a chemical raw material. The conversion of biomass into energy is performed using two main process technologies: thermochemistry and biochemistry/biological. Mechanical extraction (with esterification) is the third technology for energy production from biomass, for example, biodiesel of rapeseed methyl ester (RME).

2.2.1 Thermochemical conversion

Within thermochemical conversion, four process options are available: combustion, pyrolysis, gasification and liquefaction. Biochemical conversion includes two process options: digestion (biogas production, a mixture mainly of methane and carbon dioxide) and fermentation (production of ethanol).

Three main processes are used for thermochemical conversion of biomass, along with two less used options.

2.2.1.1. Combustion

Combustion is used in a wide range of outputs to convert the chemical energy stored in biomass into heat, mechanical energy or electricity using various items of process equipment, e.g., stoves, ovens, boilers, steam turbines, turbogenerators, etc. Biomass combustion produces hot gases at temperatures around 800–1000 °C. It is possible to burn any type of biomass, but in practice combustion is feasible only for biomass with moisture content less than 50%, unless the biomass is pre-dry. Biomass with high moisture content is best suited for biological conversion processes.

2.2.1.2. Gasification

Gasification is the conversion of biomass into a mixture of combustible gas by partial oxidation of biomass at high temperatures, typically in the range of 800 to 900 °C. The low calorific value gas (CV) produced (about 4–6) can be burned directly or used as fuel for gas engines and gas turbines ([36], [37]). The gas produced can be used as raw material (synthesis gas) in the production of chemicals (e.g., methanol).

2.2.1.3. Pyrolysis

The pyrolysis (or devolatilization) process is the thermal decomposition of materials at elevated temperatures, often in an inert atmosphere [38]. As one of the promising thermochemical conversion routes, plays a vital role in biomass conversion. However, pyrolysis is an extremely complex process; it generally goes through a series of reactions and can be influenced by many factors [39], [40], [41], [42].

Previous studies showed that biomass pyrolysis can be divided into four individual stages: moisture evolution, hemicellulose decomposition, cellulose decomposition and lignin decomposition [43], [44].

Pyrolysis is an imperative process for the combustion of most solid fuels. Pyrolysis of a given material can produce many different thermal degradation products, called pyrolysis products.

It is important to emphasize that pyrolysis is not a phase change but a chemical process. More correctly, it is a thermal degradation process, as it occurs under heat and degrades larger molecules into smaller ones.

2.2.2 Biochemical conversion

Two main processes are used, fermentation and anaerobic digestion (AD), together with a less used process based on mechanical extraction/chemical conversion.

2.2.2.1. Fermentation

Biomass is ground and starch is converted by enzymes into sugars, with yeast converting sugars into ethanol. The purification of ethanol by distillation is a step that consumes a lot of energy.

The solid residue of the fermentation process can be used as feed for livestock and, in the case of sugarcane, bagasse can be used as fuel for boilers or for further gasification [45].

2.2.2.2. Anaerobic digestion (AD)

AD is the conversion of organic material directly into a gas, called biogas, a mixture mainly of methane and carbon dioxide with small amounts of other gases, such as hydrogen sulfide [46]. Biomass is converted by bacteria into an anaerobic environment, producing a gas with an energy content of about 20 to 40% of the lower calorific value of the raw material. AD is a commercially proven technology and is widely used for the treatment of organic waste with high moisture content, i.e., +80–90% moisture.

2.2.3 Mechanical Extraction

Extraction is a mechanical conversion process used to produce oil from the seeds of various biomass crops, such as rapeseed, cotton and peanuts. The process produces not only oil, but also a residual solid or 'cake', which is suitable for animal fodder.

2.3 Delimitation of the study range

The present analysis intends to evaluate the degradation of solid biomass in a specific temperature range that characterizes the occurrence of mild pyrolysis, also known by the term torrefaction.

Torrefaction of biomass occurs at temperatures typically between 200 and 300 °C. Is a process that changes biomass properties to provide a better fuel quality for combustion and gasification applications.

This is an attractive conversion pathway for several reasons. First of all, it allows for the conversion of biomass into a hydrophobic product which is not prone to biological decomposition. This conversion allows for long-term preservation of the processed biomass that would otherwise suffer from degradation in a storage environment that is exposed to the environment. The resulting torrefied product can be utilized as a biobased fuel that can be stored long-term without degradation.

Torrefaction is based on the removal of oxygen from biomass which aims to produce a fuel with increased energy density by decomposing the reactive hemicellulose fraction and upgrade lignocellulosic composition [47]. Furthermore, increased degradation of the hemicellulose component of biomass was found to correspond with an increasingly hydrophobic solid product [21].

A certain amount of time is needed to allow the desired degree of depolymerization of the biomass to occur. The degree of torrefaction depends on the torrefaction temperature as well as on the time the biomass is subjected to torrefaction. This time is also called reactor residence time or torrefaction time.

2.4 Governing Equations and Boundary Conditions

The hydrodynamic and thermal characteristics of an oscillating flow created by an acoustic field over a single spherical particle are studied by solving the unsteady and one-dimensional conservation equations for laminar flow. Degradation temperature dependence was modelled by the Arrhenius equation. A two-step reaction in series was adopted to describe biomass decomposition during an isothermal pyrolysis process.

2.4.1 Hydrodynamics

A biomass particle of diameter d_p , mass m_p and weight F_w flowing under acoustic field, inside a reactor with constant temperature, subjected to a drag force F_d . Weight force is given by $F_w = m_p \cdot g$, g is the local gravity. Particle mass varies continuously with time, primarily as a function of drying and then thermal degradation due to chemical kinetics during torrefaction. Drag force is given by

$$F_d = \frac{\pi \left(\frac{d_p}{2}\right)^2 c_d \rho_g |u_r| u_r}{2} \quad (1)$$

where C_d is the drag coefficient, taken as a function of the Reynolds number Re , calculated by Equation 2 for a given gas viscosity μ_g . For a sphere, the value of the drag coefficient varies widely with Reynolds number as shown on the Figure 2.1. The dark line is for a sphere with a smooth surface, while the lighter line is for the case of a rough surface.

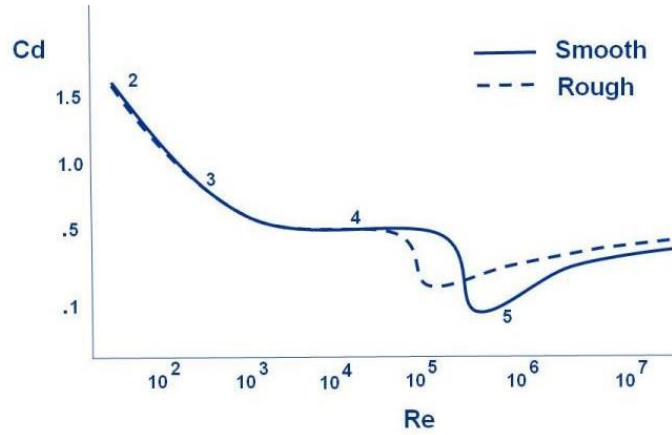


Figure 2.1 – Drag coefficient for a sphere as a function of Reynolds number.

Gas density is given by ρ_g and the relative velocity u_r between gas and particle velocities u_g and u_p is given by $u_r = u_g - u_p$. Once the particle is launched into the reactor, it is free to follow a trajectory derived from its interactions with the flow. In this sense, in order for the velocity sign to be faithfully represented, the velocity u_r was modified from the original formula of the drag force from u_r^2 to $|u_r| \cdot u_r$.

$$Re = \frac{\rho_g |u_r| d_p}{\mu_g} \quad (2)$$

Gas flow through reactor at an average constant velocity \bar{u}_g , determined by Equation 3.

$$\bar{u}_g = \frac{\dot{m}_g}{\pi \left(\frac{d_r}{2}\right)^2 \rho_g} \quad (3)$$

Gas mass flow rate is given by \dot{m}_g , considering a cylindrical reactor of diameter d_r .

2.4.2 Acoustic field

In a traveling wave acoustic field with a sound pressure of P_{rms} and acoustic impedance $\rho_g c_g$, where c_g is the speed of sound in the gas, the amplitude gas velocity

\tilde{u}_g is given by:

$$\tilde{u}_g = \frac{\sqrt{2}P_{rms}}{\rho_g c_g} \quad (4)$$

where a pre-exponential factor A is obtained from the sound pressure level L_p according to

$$P_{rms} = 10^A \quad (5)$$

$$A = \frac{L_p - 94}{20} \quad (6)$$

Equation 7 [4] insert acoustic field oscillation and calculate gas velocity u_g . The gas velocity u_g varies through time t and oscillation frequency f .

$$u_g = \bar{u}_g + \tilde{u}_g \sin(2\pi ft) \quad (7)$$

2.4.3 Balance of forces

Forces balance between weight and drag results particle's acceleration a_p , as presented at Equation 8.

$$F_w + F_d = m_p a_p \quad (8)$$

2.4.4 Particle velocity

Considering an initial particle's velocity u_0 and particle's acceleration a_p in Equation 9, yields local particle's velocity u_p .

$$u_p = u_0 + \int_0^t a_p dt \quad (9)$$

2.4.5 Particle displacement

Assuming an initial particle's position z_0 , the particle position z_p relative to vertical axis z is given by Equation 10.

$$z_p = z_0 + \int_0^t u_p dt \quad (10)$$

2.4.6 Heat transfer

Thermal diffusion equation with no heat generation in spherical coordinates

and one dimension is given by Equation 11.

$$\frac{\partial T}{\partial t} = \frac{1}{r^2} \frac{\partial}{\partial r} \left(r^2 \alpha \frac{\partial T}{\partial r} \right) \quad (11)$$

Thermal diffusivity coefficient α is given by Equation 12.

$$\alpha = \frac{k}{\rho_p c p_p} \quad (12)$$

k , ρ_p and $c p_p$ are the particle thermal conductivity, density and specific heat capacity respectively. It was assumed that k and $c p_p$ are functions of T . In particular, the effective value of these properties p_{eff} , of the residual solid were estimated as the sum of the values corresponding to the virgin material p_{wood} and of the charcoal p_{char} , at the instantaneous temperature. Each of the two values contributes to the sum in a way proportional to the conversion from dry solid raw biomass m_0 to solid torrefied biomass product m_s as following by

$$p_{eff} = \left(\frac{m_s}{m_0} \right) p_{wood} + \left(1 - \frac{m_s}{m_0} \right) p_{char} \quad (13)$$

Empirical correlations from [48] were used to set these properties as reported in Table 2.1.

Table 2.1 – Values of parameters used in the model.

Property	Correlation	Unit
Specific heat	$C_p = -1.5021 + 0.013T - 1.0 \cdot (10)^{-5} T^2$	$kJ/kg \cdot K$
Thermal conductivity	$k = \begin{cases} 0.285 & T \leq 473K \\ -0.617 + 0.0038T - 4.0 \cdot (10)^{-6} T^2 & 473K \leq T \leq 663K \end{cases}$	$W/m \cdot K$

2.4.6.1. Boundary and initial conditions for heat transfer

Boundary and initial value conditions for heat transfer are given in Equations 14, 15 and 16.

$$\left(\frac{\partial T}{\partial r} \right)_{r=0} = 0 \quad (14)$$

In Equation 14 set it is assumed symmetry conditions, then

$$-k_n \left(\frac{\partial T}{\partial r} \right)_{r=R} = h_t (T_n - T_\infty) \quad (15)$$

Equation 15 set the Robin boundary condition, where convective and conductive heat fluxes sum to zero on the particle external surface ($r = R$). T_∞ is the bulk temperature of gas flow and h_t is the convective heat transfer coefficient. The index n denotes the surface position of the grid along the particle's radius divided into n mesh points and $n - 1$ control volumes.

$$T(r, 0) = T_0 \quad (16)$$

Equation 16 set the initial condition, where all the domain is at the initial temperature T_0 .

Prandtl, Reynolds and Nusselt number in equations 17-19, derive from Ranz-Marshall [49] and are applied to calculate the convective heat transfer coefficient h_t .

$$Pr = \frac{\mu_g cp_g}{k_g} \quad (17)$$

$$Nu = \frac{h_t d_p}{k_g} \quad (18)$$

$$Nu = 2 + 0.6Re^{1/2} Pr^{1/3} \quad (19)$$

Where gas specific heat capacity is given by cp_g and gas thermal conductivity is given by k_g .

Temperature field is calculated from Equation 20.

$$T(r) = T_0(r) + \int_0^t \frac{\partial T}{\partial t} dt \quad (20)$$

2.4.7 Drying

Drying is calculated by the moisture concentration C variation in particle. Second order Fick's law equation in axisymmetric spherical coordinates is given by Equation 21.

$$\frac{\partial C}{\partial t} = \frac{1}{r^2} \frac{\partial}{\partial r} \left(r^2 D \frac{\partial C}{\partial r} \right) \quad (21)$$

Mass diffusivity coefficient D is assumed as function of T . Therefore, were adopted empirical correlation to calculate the binary diffusion coefficient for gases using the Chapman-Enskog presented in Poling et al. [50]. This correlation is applied from the internal functions of the Engineering Equation Solver (EES), which returns the

diffusivity value for a given temperature. The effective diffusivity of gas species inside the particle can be calculated by the parallel pore [51] model, as shown in Equation (22).

$$\frac{1}{D_{eff}} = \frac{1}{D_{AB}} + \frac{1}{D_{KA}} \quad (22)$$

where, D_{AB} and D_{KA} are molecular diffusivity and Knudsen diffusivity ($A = H_2O, B = N_2$). Knudsen diffusivity is given by

$$D_{KA} = \frac{d_{pore}}{3} \sqrt{\frac{8RT}{\pi M_A}} \quad (23)$$

d_{pore} is the pore diameter, R is the universal gas constant, T is the absolute temperature and M_A is the molar mass of species A .

2.4.7.1. Boundary and initial conditions for drying

Boundary and initial value conditions are given by Equations 24, 25 and 26.

$$\left(\frac{\partial C}{\partial r}\right)_{r=0} = 0 \quad (24)$$

In Equation 24 set it is assumed symmetry conditions, then

$$-D_n \left(\frac{\partial C}{\partial r}\right)_{r=R} = h_m (C_n - C_\infty) \quad (25)$$

Equation 25 set the Robin boundary condition, where convective and diffusive mass fluxes sum to zero. C_∞ is the bulk moisture concentration of the gas flow.

$$C(r, 0) = C_0 \quad (26)$$

Equation 26 set the initial condition, where all the solid domain is at the initial moisture concentration C_0 .

Schmidt, Reynolds and Sherwood number correlation from Ranz-Marshall [49] are applied to calculate the convective mass transfer coefficient h_m .

$$Sc = \frac{\mu_g}{\rho_g D_n} \quad (27)$$

$$Sh = \frac{h_m}{D_n} \frac{d_p}{a_p} \quad (28)$$

$$Sh = 2 + 0.6Re^{1/2}Sc^{1/3} \quad (29)$$

Moisture concentration field is calculated from Equation 30.

$$C(r) = C_0(r) + \int_0^t \frac{\partial C}{\partial t} dt \quad (30)$$

2.4.8 Transient mass variation

Particle mass m_p is expressed by the amount of water m_w plus the solid mass of biomass m_s , being then described by

$$m_p = m_w + m_s \quad (31)$$

The mass of water per unit volume corresponds to the product of concentration and each control volume i

$$m_w^i = C_i v_i \quad (32)$$

The total value of the water mass corresponds to the sum of the respective masses in each control volume. The sum is calculated according to equation 33

$$m_w = \sum_{i=1}^n m_w^i \quad (33)$$

In this way, to obtain the mass of the particle, it remains to define how the solid mass is expressed.

2.4.9 Reaction Kinetics

After drying, the pyrolysis process starts and essentially depends on temperature and time. The model that expresses this process of biomass degradation is the Arrhenius equation in the following form

$$k_i = A_i e^{\left(\frac{-E_a^i}{RT}\right)} \quad (34)$$

Where k_i is the reaction rate function, A_i is the pre-exponential factor, E_a^i is the activation energy, R is the universal gas constant and T is the absolute temperature. The values of the different parameters of the Arrhenius equation are determined by adjusting experimental data to reaction models for each product i .

Di Blasi and Lanzeta [22] proposed a reaction model that describes the weight

loss of biomass. This model consists of a competitive two stages, first order mechanism. In the first stage, raw biomass A reacts forming the solid intermediate reaction B and volatile V_1 . In the second stage, B reacts to form residual solid product C and volatile V_2 .

The assumptions using this model are based on two things: conversion occurs purely under kinetic control and a semi-global reaction mechanism is applicable. These steps are shown in Figure 2.2.

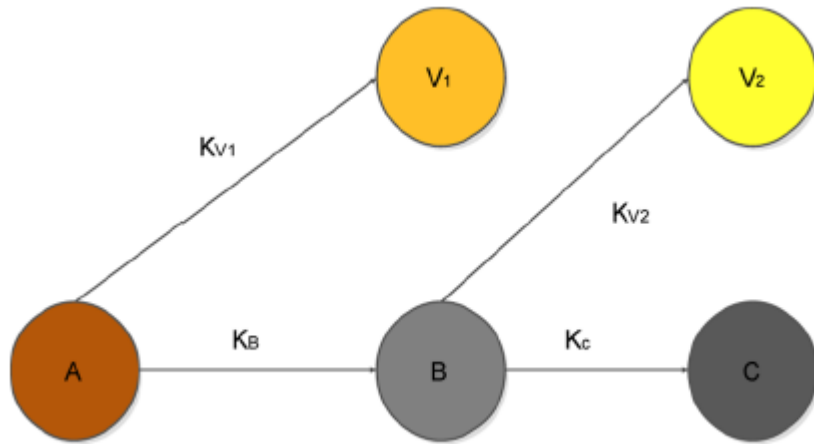


Figure 2.2 – Two-step kinetic model.

Based on this hypothesis and from Figure 2.2, differential equations 35–39 are developed from the rate equations of the individual steps.

$$r_A = \frac{dm_A}{dt} = -(k_{V_1} + k_B)m_A \quad (35)$$

$$r_B = \frac{dm_B}{dt} = k_B m_A - (k_{V_2} + k_C)m_B \quad (36)$$

$$r_C = \frac{dm_C}{dt} = k_C m_B \quad (37)$$

$$r_{V_1} = \frac{dm_{V_1}}{dt} = k_{V_1} m_A \quad (38)$$

$$r_{V_2} = \frac{dm_{V_2}}{dt} = k_{V_2} m_B \quad (39)$$

m_i is the mass of the pseudo-components ($i = A, B, C, V_1$, and V_2), and k_i is the rate constant for each of the equations as illustrated in Figure 2.2. The mathematical expressions for the overall rate constant for the first and second stages of the torrefaction reaction are expressed in equations 40 and 41.

$$k_1 = k_{V_1} + k_B \quad (40)$$

$$k_2 = k_{V_2} + k_C \quad (41)$$

Integrating equations 35–39 yields equations 42–46, with initial conditions when time $t = 0$, $m_A(0) = m_0$, $m_B(0) = m_{V_1}(0) = m_{V_2}(0) = m_C(0) = 0$. Where m_0 is the initial dry mass of the biomass.

$$m_A = m_0 e^{-k_1 t} \quad (42)$$

$$m_B = \frac{k_B m_0}{(k_2 - k_1)} e^{-k_1 t} - \frac{k_B m_0}{(k_2 - k_1)} e^{-k_2 t} \quad (43)$$

$$m_C = \frac{k_C k_B m_0}{(k_2 - k_1) k_1} [1 - e^{-k_1 t}] + \frac{k_C k_B m_0}{(k_2 - k_1) k_2} [e^{-k_2 t} - 1] \quad (44)$$

$$m_{V_1} = \frac{k_{V_1} m_0}{k_1} [1 - e^{-k_1 t}] \quad (45)$$

$$m_{V_2} = \frac{k_{V_2} k_B m_0}{(k_2 - k_1) k_1} [1 - e^{-k_1 t}] + \frac{k_{V_2} k_B m_0}{(k_2 - k_1) k_2} [e^{-k_2 t} - 1] \quad (46)$$

Where m_s corresponds to solid product remaining after the torrefaction process, and equation 47 is obtained

$$m_s = m_A + m_B + m_C \quad (47)$$

To better demonstrate the evolution of the i^{th} biomass product (solids and volatiles) during torrefaction, it is useful to adopt the mass yield, since it is possible to work with dimensionless data. The mass yield is calculated with equation 48

$$Y_i = \frac{m_i}{m_0} \quad (48)$$

Bates et al., [21] obtained the elemental composition using raw material composition and data of the released volatiles from Ref. [25], assuming that the composition of the volatiles pseudo-components was constant and not temperature-dependent.

2.4.10 Solid composition

Combining mass conservation with the kinetics rate expressions, the rate of change of the carbon, hydrogen, oxygen, nitrogen, and ash content of the solid product

is written in terms of the composition and formation rates of V_1 and V_2 .

$$\frac{d(m_s Y_{j,d})}{dt} = -\frac{dm_{V_1}}{dt} Y_{j,V_1} - \frac{dm_{V_2}}{dt} Y_{j,V_2} \quad (49)$$

Where, m_s is the mass of the solid product composed of element ($j = C, H, O, N, ash$) on a dry basis.

Based product distribution analysis from Figure 2.2, where decomposition occurs first-order with respect to the reactant (A and B for stage 1 and 2, respectively), the composition of B and C can then be defined from mass balance.

The instantaneous fractional yields are defined by the formation rate of product divided by the decomposition rate of the reactant:

$$\beta = \frac{r_{B,1}}{-r_{A,1}} = \frac{k_B m_A}{(k_{V_1} + k_B) m_A} = \frac{k_B}{(k_{V_1} + k_B)} \quad (50)$$

$$\nu = \frac{r_{V_1,1}}{-r_{A,1}} = \frac{k_{V_1} m_A}{(k_{V_1} + k_B) m_A} = \frac{k_{V_1}}{(k_{V_1} + k_B)} \quad (51)$$

$$\gamma = \frac{r_{C,2}}{-r_{B,2}} = \frac{k_C m_B}{(k_{V_2} + k_C) m_B} = \frac{k_C}{(k_{V_2} + k_C)} \quad (52)$$

$$\zeta = \frac{r_{V_2,2}}{-r_{B,2}} = \frac{k_{V_2} m_B}{(k_{V_2} + k_C) m_B} = \frac{k_{V_2}}{(k_{V_2} + k_C)} \quad (53)$$

The two-step kinetic mechanism can be expressed as



According to Bates [21], the chemical compositions of the pseudo components V_1 and V_2 were assumed constant within 200-300 °C. Moreover, stage one volatiles (V_1) are expected to represent primarily (but not solely) hemicellulose decomposition products and stage two volatiles (V_2) should be representative of cellulose decomposition products.

His results showed agreement with several experimentally observed trends in the volatiles produced during wood pyrolysis. To summarize, the composition of V_1 and V_2 are modeled with unique chemical mixtures of nine species which do not vary with temperature (between 230 and 300 °C) and are fitted to experimental data. These

results are described in Table 2.2. Values were calculated for carbon, hydrogen, and oxygen content. Nitrogen and ash content assumed to be negligible in volatiles.

Table 2.2 – Fitted V_1 and V_2 composition (% mass) from [21].

Chemical Component	Percentage	
	V_1	V_2
Acetic acid	$Y_{a,v1} = 14.8\%$	$Y_{a,v2} = 16.1\%$
Water	$Y_{b,v1} = 48.1\%$	$Y_{b,v2} = 7.6\%$
Formic acid	$Y_{c,v1} = 5.3\%$	$Y_{c,v2} = 5.1\%$
Methanol	$Y_{d,v1} = 4.2\%$	$Y_{d,v2} = 30.1\%$
Lactic acid	$Y_{e,v1} = 1.3\%$	$Y_{e,v2} = 31.3\%$
Furfural	$Y_{f,v1} = 1.1\%$	$Y_{f,v2} = 0.0\%$
Hydroxy acetone	$Y_{g,v1} = 0.6\%$	$Y_{g,v2} = 9.7\%$
Carbon dioxide	$Y_{h,v1} = 20.4\%$	$Y_{h,v2} = 0.0\%$
Carbon monoxide	$Y_{i,v1} = 4.2\%$	$Y_{i,v2} = 0.1\%$
Sum	100%	100%
Carbon	$Y_{C,v1} = 18\%$	$Y_{C,v2} = 36\%$
Hydrogen	$Y_{H,v1} = 7\%$	$Y_{H,v2} = 9\%$
Oxygen	$Y_{O,v1} = 75\%$	$Y_{O,v2} = 55\%$
Nitrogen	$Y_{N,v1} = 0\%$	$Y_{N,v1} = 0\%$
Ash	$Y_{Ash,v1} = 0\%$	$Y_{Ash,v1} = 0\%$
Sum	100%	100%

Based on the modeling proposed by Bates (2012), the composition of A is fixed and known from the ultimate analysis of the raw biomass. The compositions of V_1 and V_2 are fixed and defined by the previously described volatile composition model.

From the instantaneous fractional yields defined [equations 50-53], it is possible to define the composition (ultimate analysis) of B and C . The composition of B and C depends on the instantaneous fractional yields and the compositions of A , V_1 and V_2 :

$$Y_{j,B} = \frac{Y_{j,A} - \nu Y_{j,V_1}}{\beta} \quad (56)$$

$$Y_{j,C} = \frac{Y_{j,B} - \zeta Y_{j,V_2}}{\gamma} \quad (57)$$

2.4.11 Performance parameters

The predicted elemental composition allowed for the calculation of the Higher heating value (HHV) prediction dynamics. To calculate the HHV of untreated and

torrefied wood, the correlation presented in Equation 58 [52] was employed. C , H , and O are the mass fraction of carbon, hydrogen, and oxygen on a dry ash-free basis [14].

$$HHV[MJ/kg] = -1.3675 + 0.3137 \times C + 0.7009 \times H + 0.0318 \times O \quad (58)$$

The HHV enhancement factor (EF) is calculated as Equation 59

$$EF = \frac{HHV_{torrefied}}{HHV_{raw}} \quad (59)$$

Total solid yield Y_s is given by the sum of each solid product composed of product ($i = A, B, C$) on a dry basis:

$$Y_s = \sum Y_i \quad (60)$$

Energy yield EY is defined as the ratio of an increase of calorific value (heating value) to a decrease in weight of biomass, i.e., for a higher energy yield. The biomass weight loss should be overcome by an increase in the calorific value [53]. Energy yield is calculated as follows:

$$EY = Y_s \times EF \quad (61)$$

The energy-mass co-benefit index ($EMCI$) is calculated as Equation 62

$$EMCI = EY - Y_s \quad (62)$$

3 METHODOLOGY

3.1 Discretization

Temperature and Concentration distribution inside the particle is obtained after discretization applying a finite difference method. The particle was divided in a series of control volumes whose radial length is given by Equation 63.

$$\Delta_r = \frac{R}{n-1} \quad (63)$$

Where n is the number of mesh points along the radius R .

Since the domain is divided in $n - 1$ elements, with Δ_r length and $i \in \{1, \dots, n\}$, for convenience, the notations can be adopted in terms of ($r = 0$ or $i = 1$) and ($r = R$ or $i = n$) with no loss of generality.

Space Domain diagram can be geometrically described by Figure 3.1.

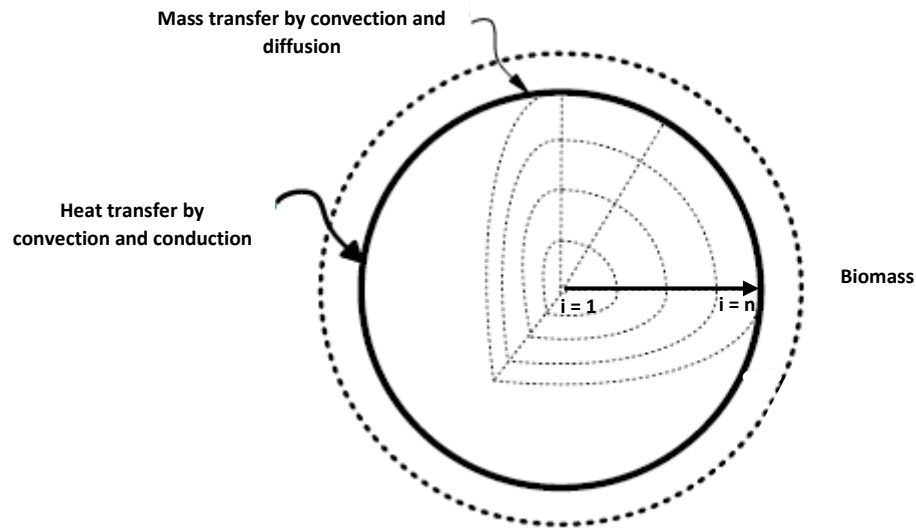


Figure 3.1 – Biomass particle radial control volumes, likewise onion layers.

3.2 Hypotheses

The conservation equations of mass and energy are used to create a numerical model that describes the torrefaction of the biomass. Some assumptions are made to simplify the numerical solution of the model.

- The model is essentially one-dimensional, which means that gradients in concentration and temperature only exist in one direction;
- The biomass properties are assumed to be isotropic;
- The shrinkage of the particle can be considered insignificant;
- Internal heat generation and radiation in the particle were not considered;
- The model was developed for a transient process;
- The gas flow takes place in a uniform regime and constant temperature;
- The acoustic field considered in the reactor is of standing waves and one-dimensional.

3.3 Numerical method

Figure 3.1 gives the notations used to discretize the portion of the sphere for which the temperature field is sought. The r axis is divided into $n - 1$ spherical layers of thickness Δ_r . With this notation, n mesh points are defined and correspond to (i) , which varies from 1 to n .

Thibault et al. [54] presented a finite-difference solution of the Heat Equation in spherical coordinates. Two different numerical methods were compared: the method based on the superposition principle and the method of Brian. For this study, the superposition method was chosen. As the present model is one-dimensional, the method proposed by Thibault will be simplified to apply only the radial direction.

The formulation of the algorithm based on the superposition principle is given by

$$\frac{T_{i,t} - T_{i,t+\Delta t}}{\Delta t} = \alpha \left[\frac{T_{i+1,t} - 2T_{i,t} + T_{i-1,t}}{\Delta r^2} + \frac{T_{i+1,t} - T_{i-1,t}}{(i-1)\Delta r^2} \right] + \frac{d\alpha}{dT} \left(\frac{T_{i+1,t} - T_{i-1,t}}{2\Delta r} \right)^2 \quad (64)$$

Equation 64 apply only for interior mesh points ($1 < i < n$).

For mesh points located on a boundary, special consideration is necessary. For the radial direction at $r = 0$ ($i = 1$), finite-difference equation becomes

$$\frac{T_{1,t} - T_{1,t+\Delta t}}{\Delta t} = 6\alpha \left[\frac{T_2 - T_1}{\Delta r^2} \right] \quad (65)$$

On the surface of the sphere $r = R$ ($i = n$), there is a heat flux into the surface given by Equation 15.

In finite-difference form, Equation 15 is best represented by the central difference form

$$-k_n \frac{T_{n+1} - T_{n-1}}{2\Delta r} = h_t (T_n - T_\infty) \quad (66)$$

where $(n + 1)$ is an imaginary grid point located at a distance Δ_r beyond the boundary. The imaginary point is eliminated by combining Eqs. (64) and (66) to yield

$$\frac{T_{n,t} - T_{n,t+\Delta t}}{\Delta t} = 2\alpha \left[\frac{T_{n-1} - T_n}{\Delta r^2} + \frac{h_t (T_n - T_\infty)}{-k_n \Delta r} \left(1 + \frac{1}{n-1} \right) \right] + \frac{d\alpha}{dT} \left(\frac{h_t (T_n - T_\infty)}{-k_n} \right)^2 \quad (67)$$

The same numerical solution can be applied to Fick's second law. The boundary and initial conditions are also reproduced and the equations for the numerical solution of the mass diffusivity are given by

$$\frac{C_{1,t} - C_{1,t+\Delta t}}{\Delta t} = 6D \left[\frac{C_2 - C_1}{\Delta r^2} \right], (i = 1) \quad (68)$$

$$\frac{C_{i,t} - C_{i,t+\Delta t}}{\Delta t} = D \left[\frac{C_{i+1} - 2C_i + C_{i-1}}{\Delta r^2} + \frac{C_{i+1} - C_{i-1}}{(i-1)\Delta r^2} \right] + \frac{dD}{dT} \left(\frac{T_{i+1} - T_{i-1}}{2\Delta r} \right) \left(\frac{C_{i+1} - C_{i-1}}{2\Delta r} \right), (1 < i < n) \quad (69)$$

$$\frac{C_{n,t} - C_{n,t+\Delta t}}{\Delta t} = 2D \left[\frac{C_{n-1} - C_n}{\Delta r^2} + \frac{h_m(C_n - C_\infty)}{-D\Delta r} \left(1 + \frac{1}{n-1} \right) \right] + \frac{dD}{dT} \left(\frac{h_t(T_n - T_\infty)}{-k} \right) \left(\frac{h_m(C_n - C_\infty)}{-D} \right), (i = n) \quad (70)$$

An important observation about the chosen method is that because it is implicit is unconditionally stable, so it allows longer time intervals for simulation. This feature allows a wide range of simulations, as will be seen in the results later.

3.4 Modelling

A system design is presented in Figure 3.2, consisting of a biomass feeder source and a pyrolysis reactor, with biomass' round particles under the influence of a sound source induced oscillation. The proposed scheme presents an outlet for the input and volatile gases after the path in the pyrolysis reactor.

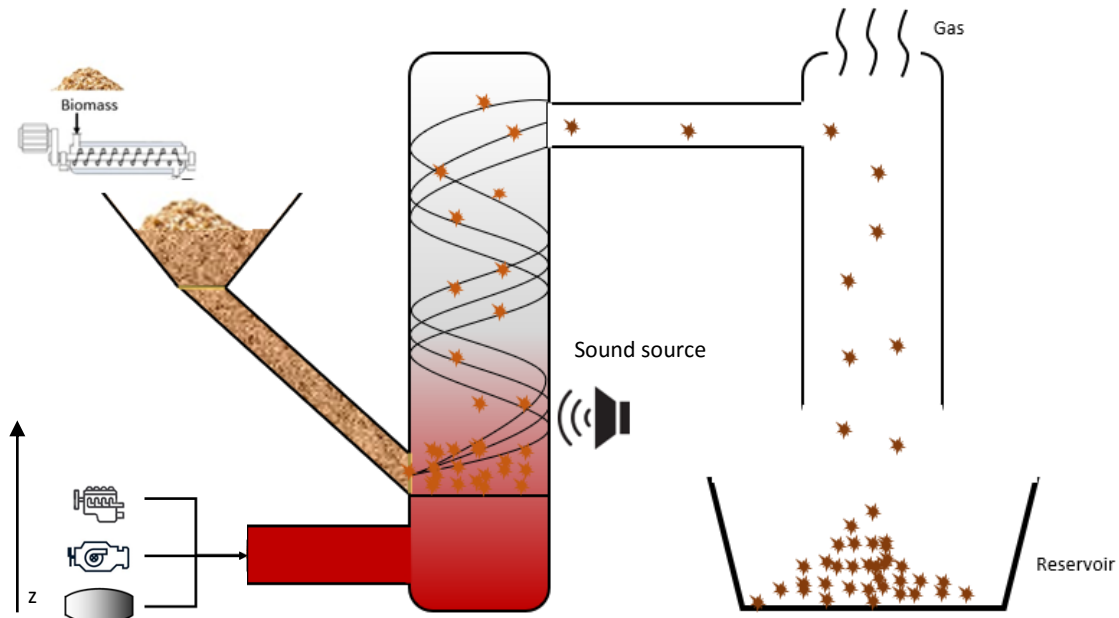


Figure 3.2 – Pyrolysis reactor under acoustic field given by a sound source and storage reservoir.

The proposed reactor can be built from a heat source derived from the output gases of a diesel engine, otto engine or gas microturbine.

The design of this equipment derives mainly from its dimensioning. The main dimension is its length, which is directly related to the residence time required for the biomass to be submitted to torrefaction and reach the maximum EMCI.

3.5 Analyzed biomass

The biomass employed in this work was Eucalyptus Grandis sawdust with a density of 640 kg/m³ and moisture content of 12% [55]. Information available for the identification of wood species is usually expressed in terms of solid wood specific gravity (S_g) and moisture content. Considering that the present work is focused on the study of particles in the form of sawdust, it will be assumed that the specific gravity of sawdust corresponds to a third of S_g . This consideration is compatible with the observations made by Thompson and Darwin in 1968 [56].

The kinetic parameters used in the simulation were the same as those obtained by Silveira et al. (2021) [34]. In this study, an online method – TG coupled with FTIR – and elemental analysis were applied to acquire data in order to perform an experimental and numerical thermal upgrading assessment of Eucalyptus Grandis.

Ultimate analysis data are also needed to calculate the performance parameters, especially the EMCI. This information was extracted from [34] too.

The kinetic parameters and ultimate data for each biomass are listed in tables 3.1 and 3.2.

Table 3.1 – Kinetic parameters for studied biomass.

Biomass	Pre-exponential factor [min ⁻¹]				Activation Energy [J/mol]			
	A_B	A_C	A_{V1}	A_{V2}	Ea_B	Ea_C	Ea_{V1}	Ea_{V2}
Eucalyptus Grandis	2,76E+07	2,31E+00	7,00E+11	1,06E+09	85349	24333	137038	119485

Table 3.2 – Ultimate analysis data for studied biomass.

Biomass	Specific gravity	Moisture content	Ultimate analysis		
			Y_C	Y_H	Y_O
Eucalyptus Grandis	0,64	0,12	0,44	0,06	0,49

3.6 Equation Solving Program

The derived differential equations are solved numerically using the equation-based integral function of the Engineering Equation Solver software (EES) [57].

EES was chosen for its practicality in the solutions and speed in executing system of equations. Mathematical modeling introduced in the code editor has similarities with the theoretical language that benefit the elaboration of algorithms in a reduced time.

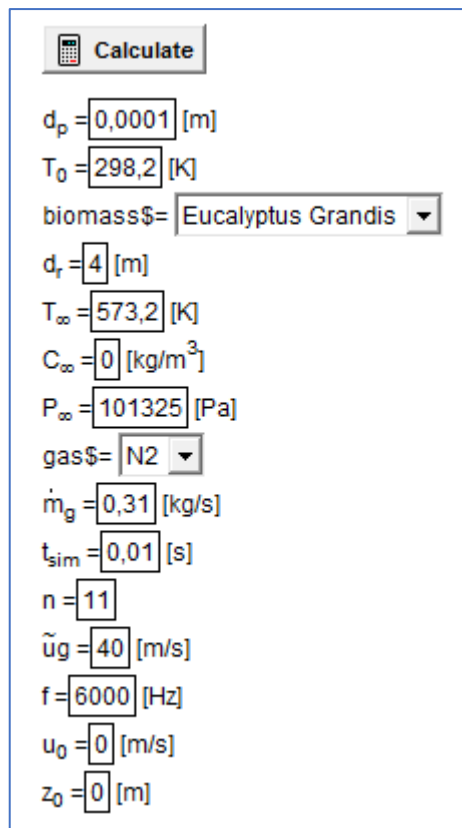
There are two major differences between EES and existing numerical equation-solving programs. First, EES automatically identifies and groups equations

that must be solved. This simplifies the process and ensures that the solver will always operate at optimum efficiency. Second, EES provides many built-in mathematical and thermophysical property functions useful for engineering calculations [57].

EES uses numerical integration to solve differential equations. The Integral function can use a fixed supplied step or an automatic step adjusted to meet some accuracy criteria.

3.7 Simulation parameters

Simulations were performed varying parameters such as particle diameter, residence time, amplitude velocity and acoustic oscillation frequency. Input interface is shown in Figure 3.3.



The screenshot shows a user interface for inputting simulation parameters. At the top left is a 'Calculate' button with a calculator icon. Below it are several input fields, each with a label, a value, and a unit. The parameters and their values are: $d_p = 0,0001$ [m], $T_0 = 298,2$ [K], biomass\$ = Eucalyptus Grandis (selected from a dropdown), $d_r = 4$ [m], $T_\infty = 573,2$ [K], $C_\infty = 0$ [kg/m³], $P_\infty = 101325$ [Pa], gas\$ = N2 (selected from a dropdown), $\dot{m}_g = 0,31$ [kg/s], $t_{sim} = 0,01$ [s], $n = 11$, $\tilde{u}_g = 40$ [m/s], $f = 6000$ [Hz], $u_0 = 0$ [m/s], and $z_0 = 0$ [m].

Figure 3.3 – User interface program for input data.

EES software has data integration features that allow reading from external files. A list of kinetic parameters such as k_i , A_i and E_a^i of equation 34 was elaborated and the simulation of different types of biomasses can be carried out in a practical and fast way by choosing the simulation biomass in a selection box.

3.8 Method verification

The discretized method was compared with EES library function from an analytical solution to Heat Equation [58], resulting differences between numerical and analytical solution lower than $1,5E-02$ K for temperature field. Solid lines in Fig. 3.4 represent the results for the numerical simulation. Circle symbols represent the results obtained by EES [58].

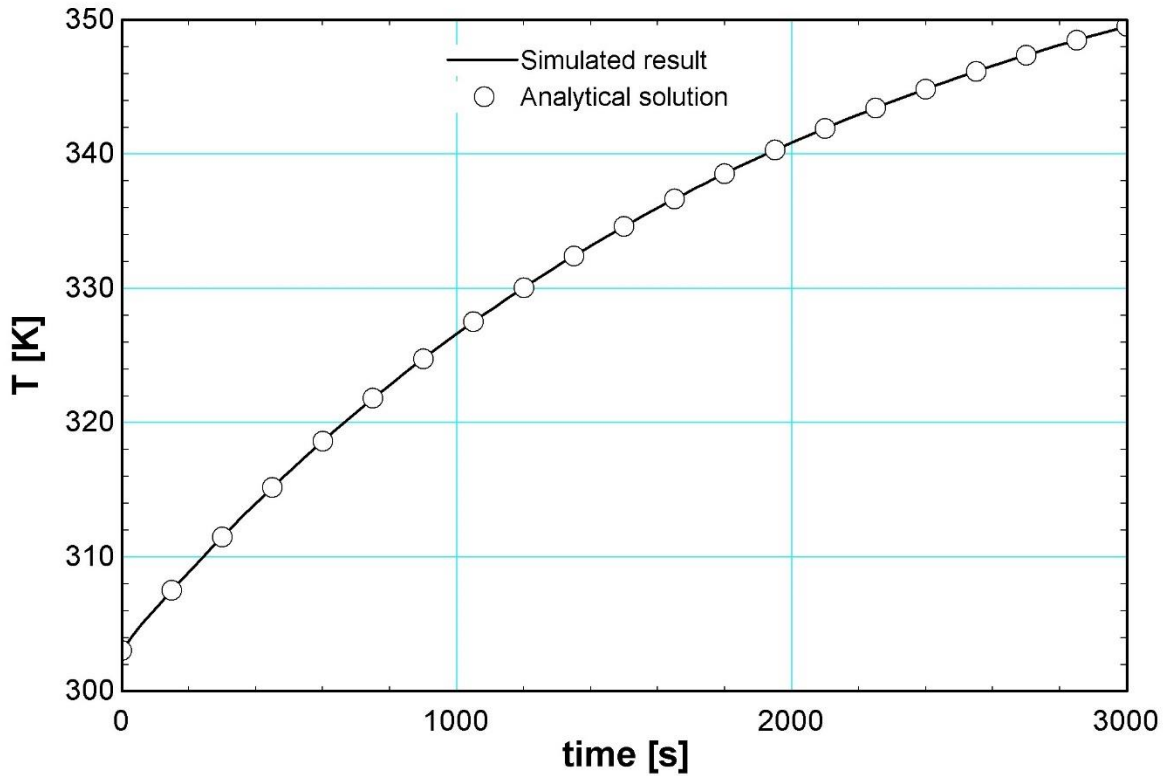


Figure 3.4 – Comparison of the simulated results for the temperature field as a function of time with those of analytical solution [58].

For the same solution from [58], two grid points with 10 and 100 mesh points were employed to check system sensitivity for grid sizing. The numerical results are shown in figure 3.5.

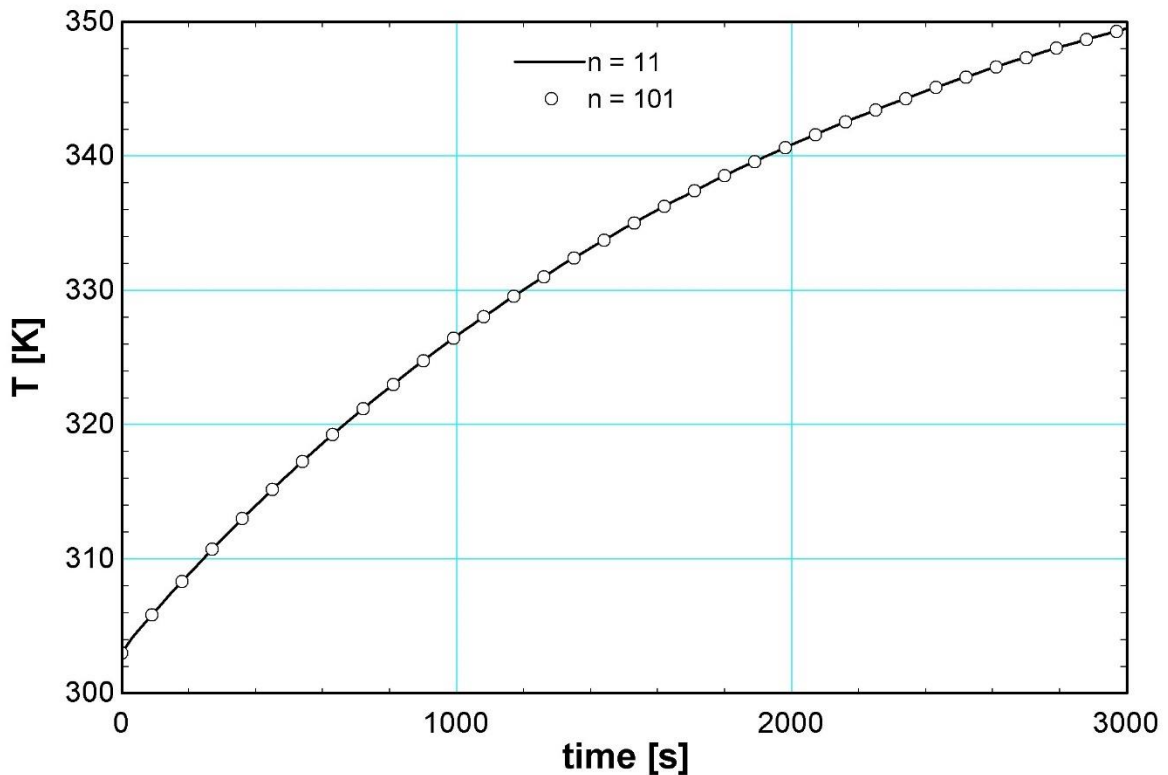


Figure 3.5 - System grid sizing checking.

3.9 Method validation

The model can represent the torrefaction treatment, and the reported results [22,28,32] corroborate the fitting quality for predicted weight loss described in the thermal degradation dynamics. The two-step model has been applied to mild pyrolysis for different biomass and separate wood components [22,28,32]. The kinetic model developed and validated in Refs. [18,19] was employed in this study.

The acoustic flow was simulated under the same conditions used by Ha [5] namely, $d_p = 100 \mu m$, $P = 1 atm$, $\tilde{u}_g = 10 m/s$. The present results compare very well with those of Ha [5] given the assumptions of spherical symmetry and one-dimensional geometry. This result shows that the conservation equations based on the spherical symmetry and one-dimension assumptions are good enough for predicting the case of the torrefaction of a spherical biomass particle surrounded by an acoustic flow.

3.10 Simulation conditions

Torrefaction for a particle, surrounded by an acoustic flow, was simulated under conditions described in table 3.3.

Table 3.3 - Values of the constant parameters used in the simulation.

Property	Value	Unit
T_0	298,2	<i>K</i>
T_∞	573,2	<i>K</i>
C_∞	0	<i>kg/m³</i>
P_∞	101325	<i>Pa</i>
\dot{m}_g	0,31	<i>kg/s</i>
d_r	4	<i>m</i>
n	11	–
u_0	0	<i>m/s</i>
z_0	0	<i>m</i>
d_{pore} [59]	$3,2 \times 10^{-6}$	<i>m</i>

After the successful test runs, the cases shown in Table 3.4 were run to investigate the degradation of a single biomass particle in the presence of a high intensity acoustic field. The parameters are shown in Table 3.4.

These parameters were calculated using the thermophysical properties given at ambient conditions: $P_\infty = 101325 \text{ Pa}$, $T_\infty = 573,2 \text{ K}$ and $C_\infty = 0 \text{ kg/m}^3$. The initial particle temperature was fixed at $298,2 \text{ K}$. The domain of the numerical solution is taken as the shells along radius of the particle as shown in figure 3.1. 11 points in the radial direction were used in the present simulation.

A mass flow rate of $0,31 \text{ kg/s}$ was adopted considering a microturbine extracted from a manufacturer's catalog [60].

The reactor diameter was chosen considering a low velocity for the gas and, consequently, a shorter length of the reactor for design purposes.

The thermal conductivity and specific heat of the particle are taken to be calculated from [48].

Table 3.4 – Variable parameters used in the torrefaction of a single biomass particle in the presence of the oscillating flow.

<i>Case</i>	$d_p[\mu m]$	$f[Hz]$	$\tilde{u}_g[m/s]$	$t_r[s]$
1	100	0	0	0,0001-0,01
	100	60	10	0,0001-0,01
	100	600	10	0,0001-0,01
	100	6000	10	0,0001-0,01
2	100	0	0	0,0001-0,01
	100	6000	10	0,0001-0,01
	100	6000	20	0,0001-0,01
	100	6000	40	0,0001-0,01
3	50	0	0	0,0001-0,01
	50	60	10	0,0001-0,01
	100	0	0	0,0001-0,01
	100	60	10	0,0001-0,01
	150	0	0	0,0001-0,01
	150	60	10	0,0001-0,01
4	100	0	0	1000
	100	60	10	1000

4 RESULTS AND DISCUSSION

4.1 Case 1

Case 1 in Table 3.4 simulated the torrefaction of a particle of 100 μm and amplitude velocity of 10 m/s in the presence of an acoustic field in different frequency ranges up to a maximum value of 6000 Hz. The results were compared with the simulation of the same flow without the presence of oscillation. The reduction in moisture concentration increased directly with frequency, resulting in faster drying at higher frequency levels, as shown in figure 4.1.

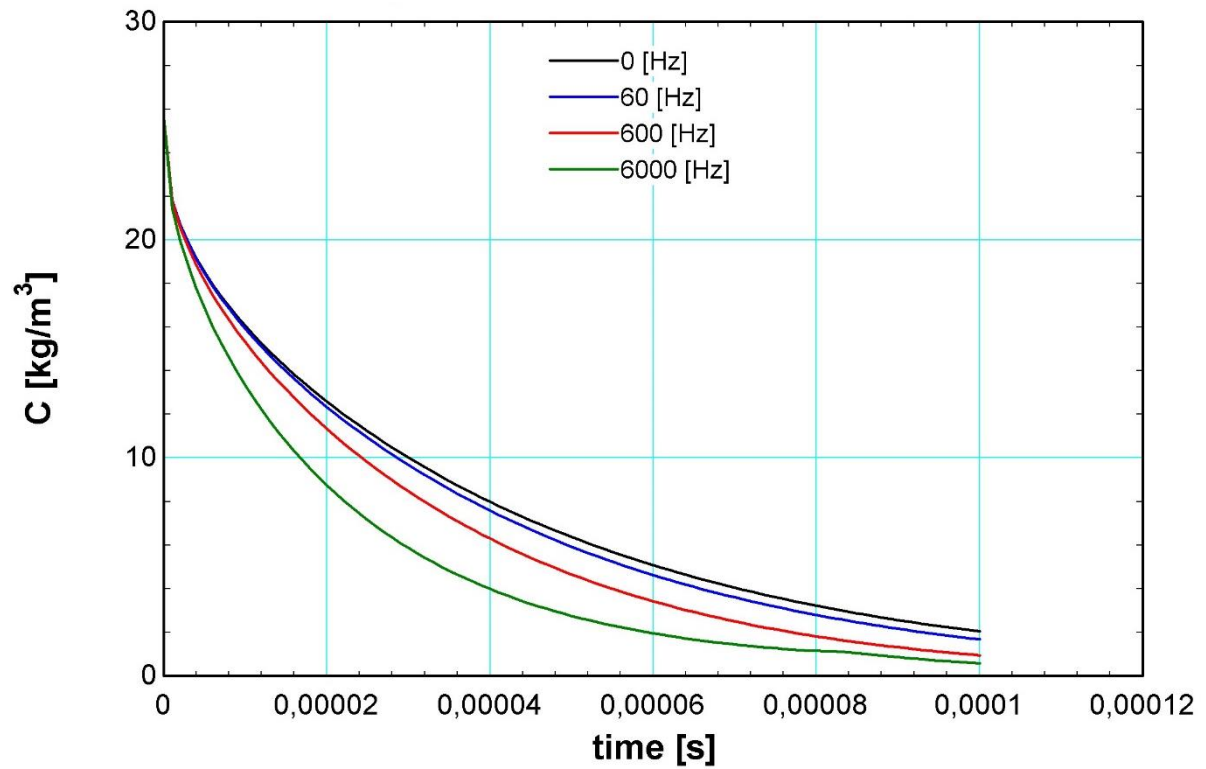


Figure 4.1 – Moisture concentration field, Case 1.

The faster drying is a consequence of the changes indicated in the convective mass transfer coefficient h_m shown in figures 4.2, 4.3, 4.4 and 4.5. As the frequency increases, h_m values increase and more strongly. These effects result in faster mass transfer, corroborating the earlier observation on abbreviation of drying. The increase in drying rate peaked at 42%.

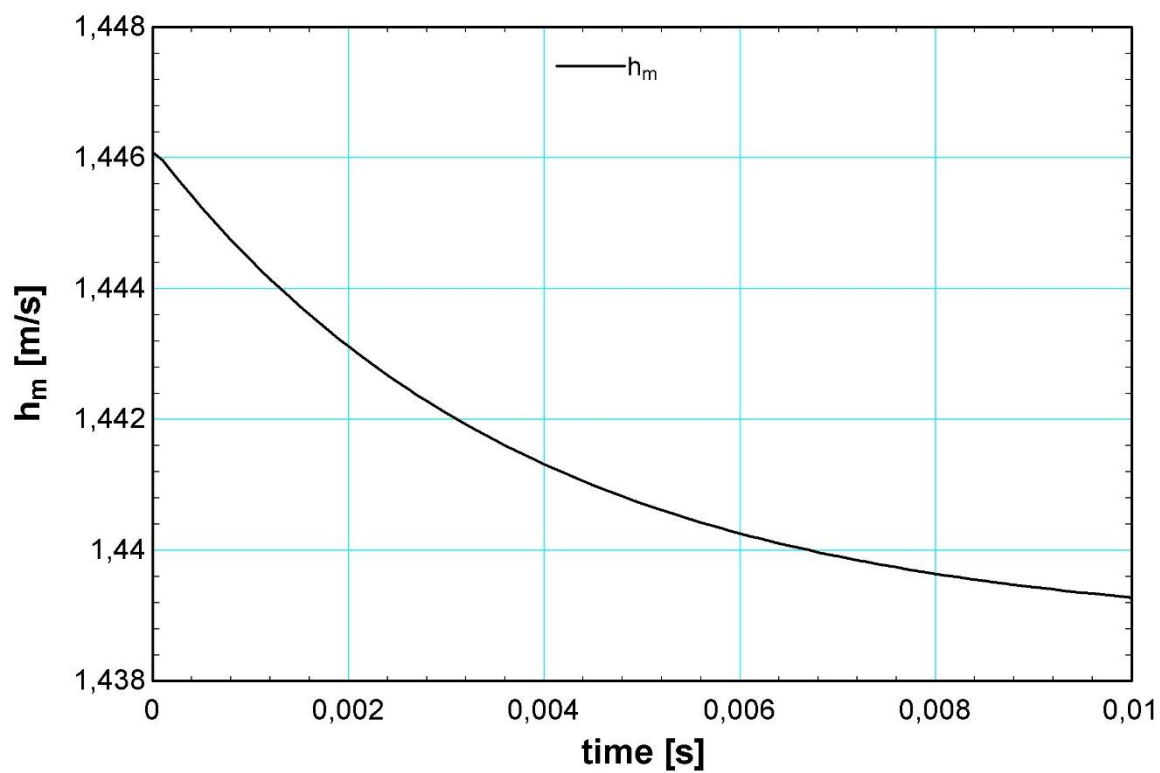


Figure 4.2 – Mass transfer coefficient, Case 1, $f = 0$ Hz.

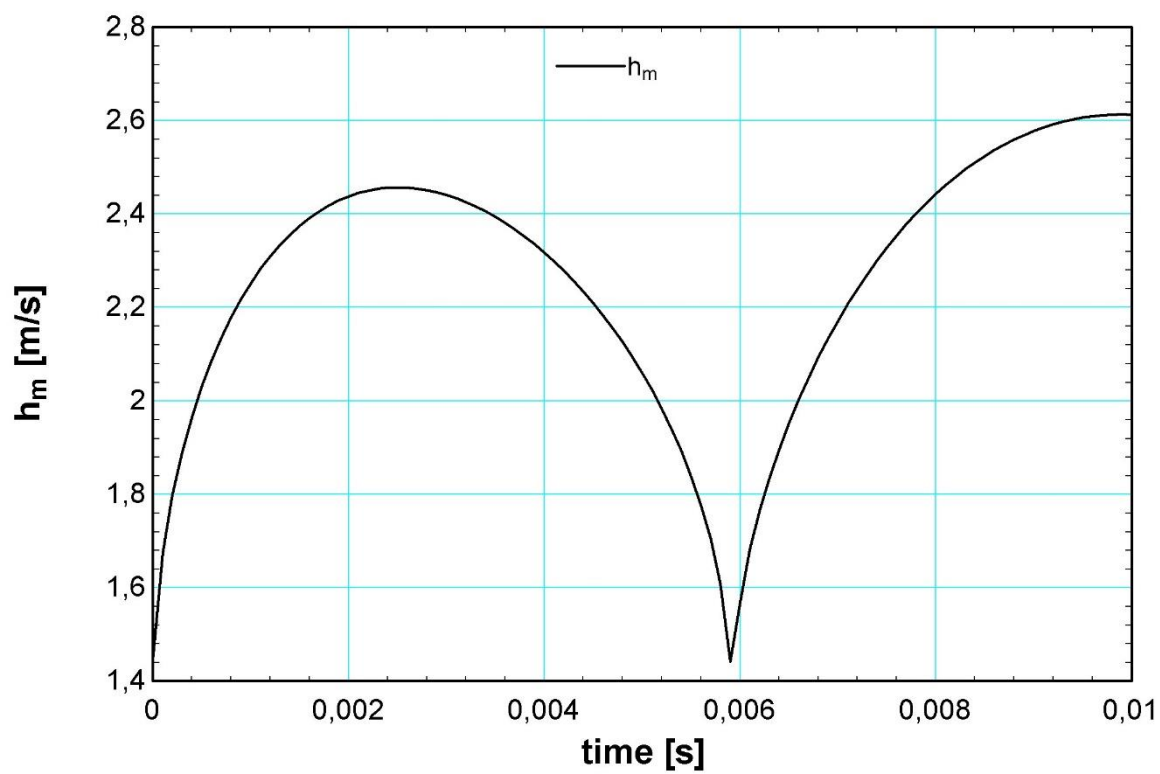


Figure 4.3 – Mass transfer coefficient, Case 1, $f = 60$ Hz.

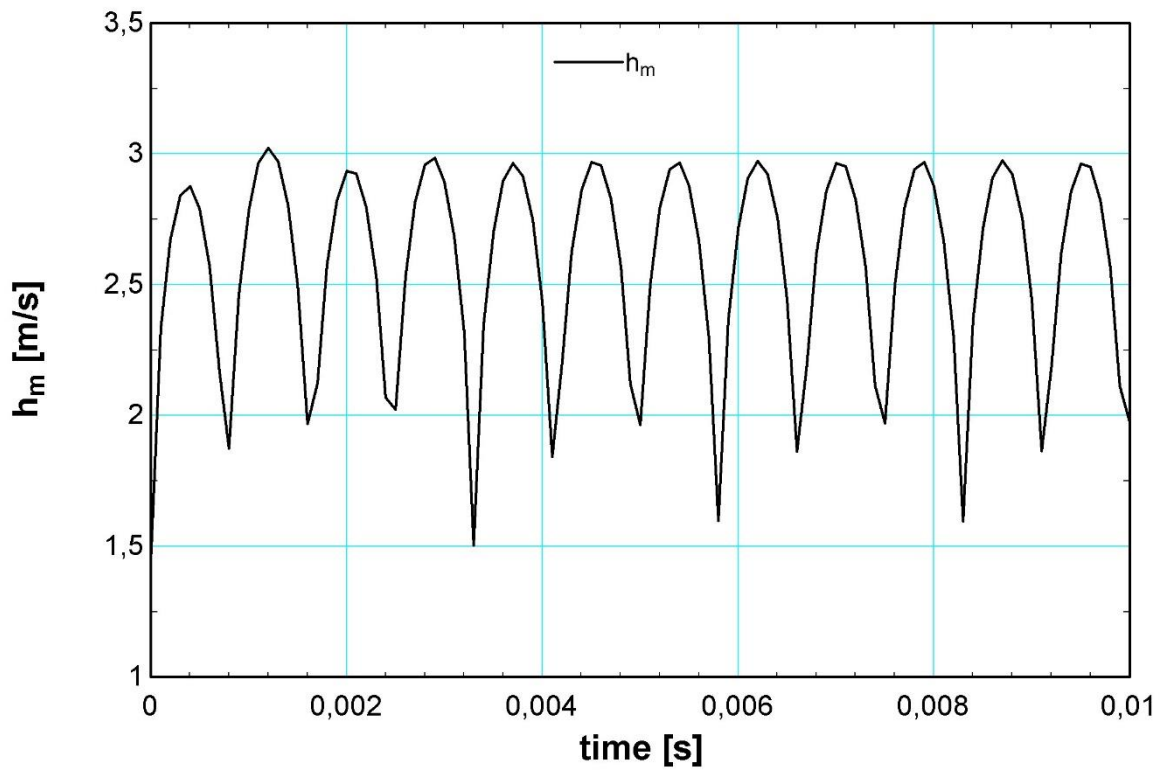


Figure 4.4 – Mass transfer coefficient, Case 1, $f = 600$ Hz.

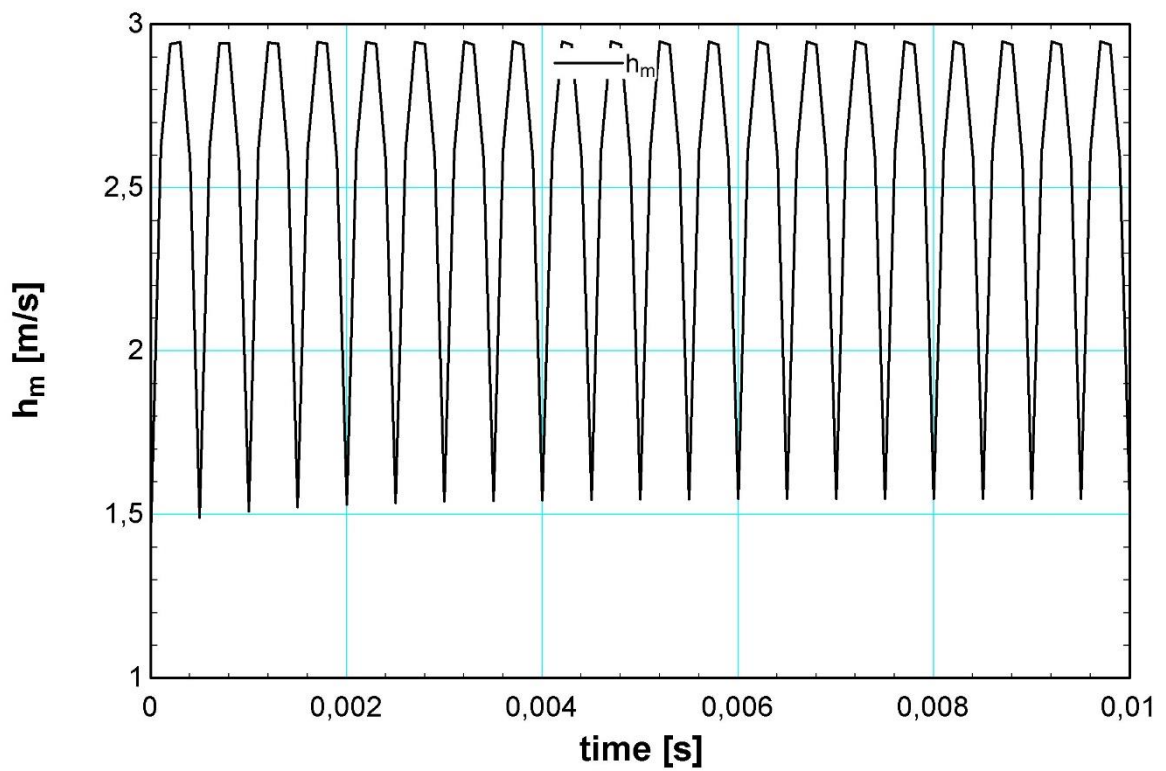


Figure 4.5 – Mass transfer coefficient, Case 1, $f = 6000$ Hz.

The temperature also increased with increasing frequency, leading the particle to the isothermal state in shorter times according to figure 4.6. Due to thermal diffusivity, the understanding of the increase in heat transport rates is similar to what happened for mass diffusivity and ratified with the changes observed in the convective heat transfer coefficient h_t in figures 4.7, 4.8, 4.9 and 4.10.

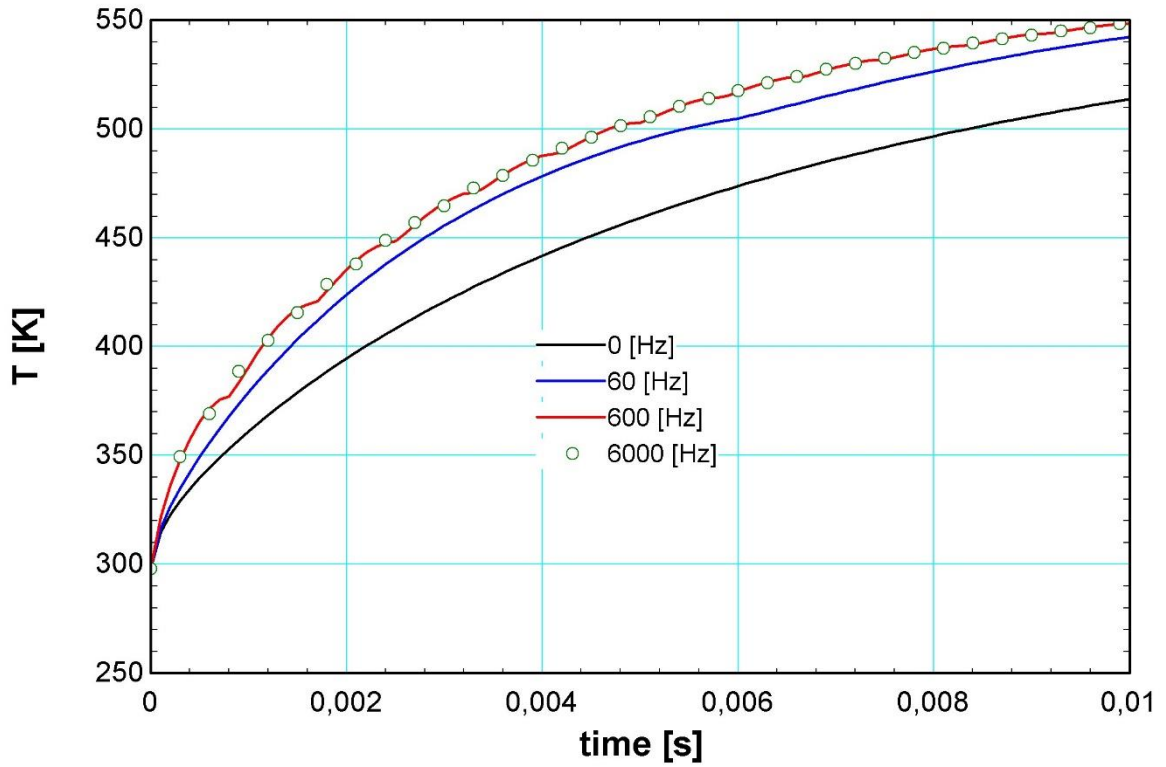


Figure 4.6 – Temperature field, Case 1.

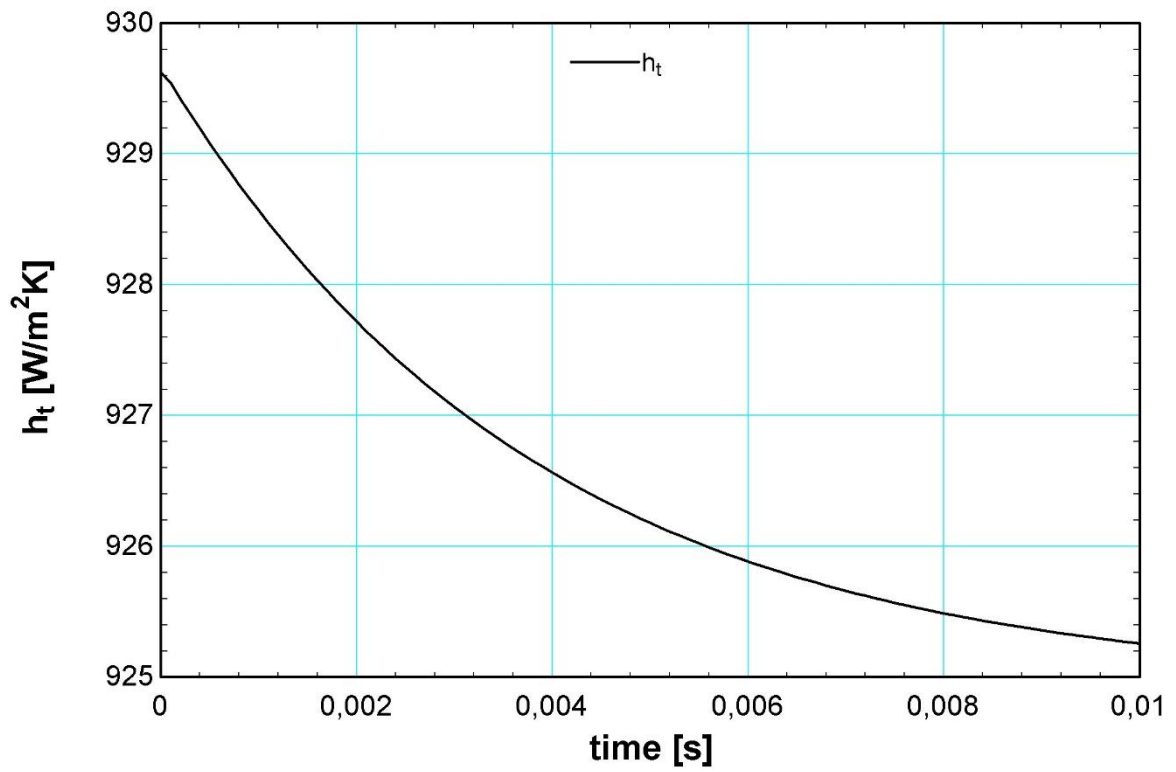


Figure 4.7 – Heat transfer coefficient, Case 1, $f = 0 \text{ Hz}$.

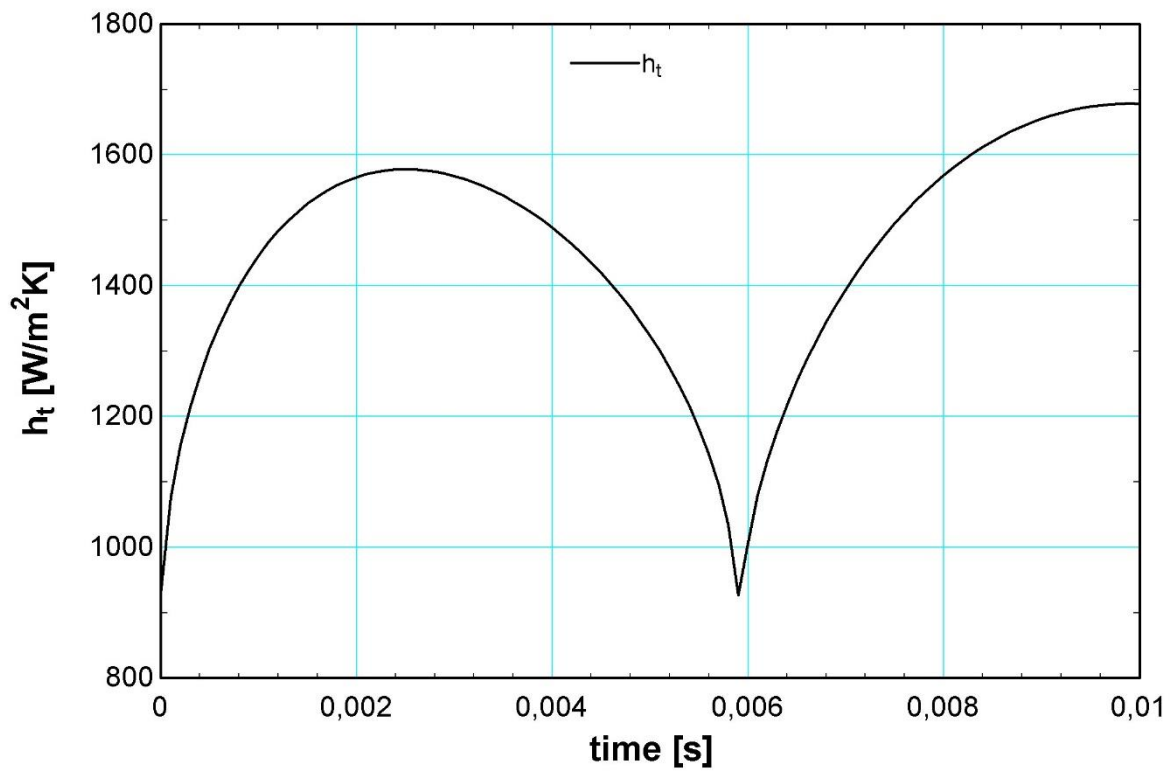


Figure 4.8 – Heat transfer coefficient, Case 1, $f = 60 \text{ Hz}$.

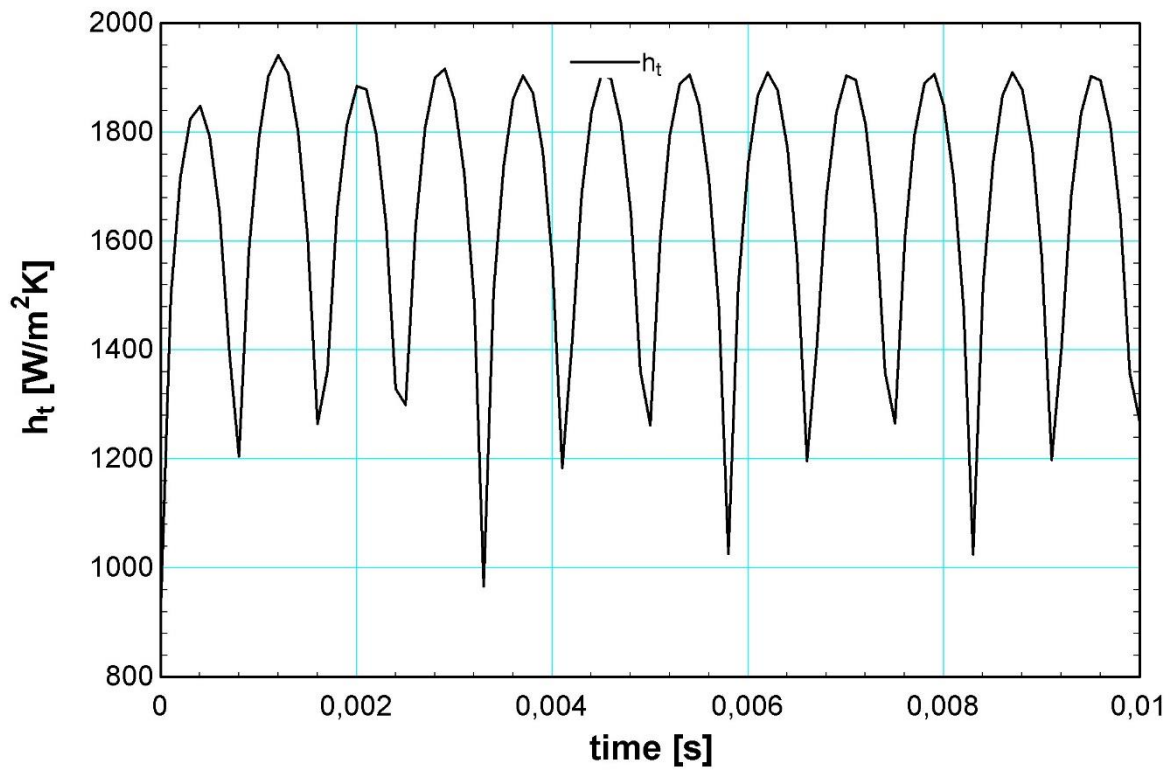


Figure 4.9 – Heat transfer coefficient, Case 1, $f = 600 \text{ Hz}$.

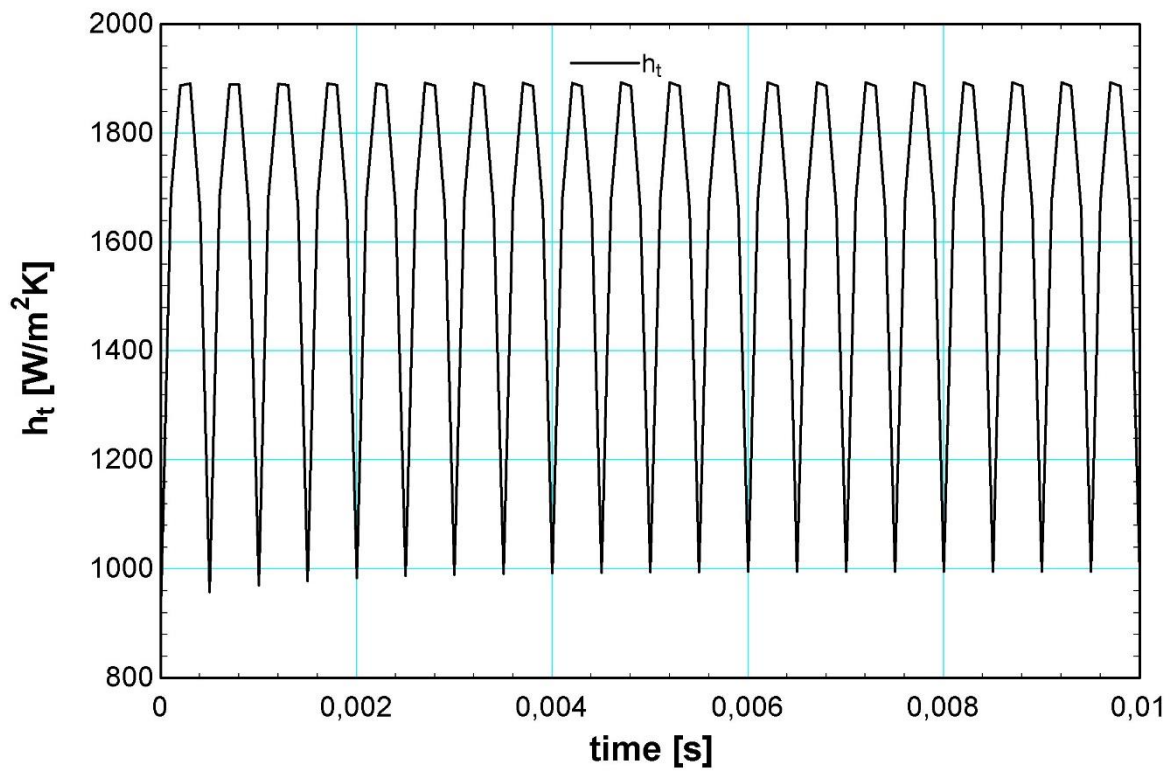


Figure 4.10 – Heat transfer coefficient, Case 1, $f = 6000 \text{ Hz}$.

Velocity profiles were appreciably altered with changes in frequency. The absence of oscillation describes a particle that reaches a terminal velocity derived from the balance between the gravitational field strength and the drag force as observed in figure 4.11.

With the inclusion of the acoustic field, the lower frequency values (60 Hz) describe a particle velocity profile very similar to the gas velocity profile, differentiated by a small phase lag as shown in figure 4.12. The increase in frequency to 600 Hz described in figure 4.13 implies well-defined velocity profiles and with different amplitudes for the gas and particle, indicating a reduction in the particle oscillation amplitude as a result of the greater intensity in the change of flow direction, without the corresponding change by the particle. This condition points to higher values of the relative velocity between the flow and the particle, justifying the increase in the range of h_m and h_t values.

The increase in frequency to 6000 Hz described in figure 4.14, although it implies a greater intensity in the occurrence of h_m and h_t at higher levels, does not promote an increase in their value ranges, suggesting that their effects no longer contribute to increasing mass and heat transfer rates.

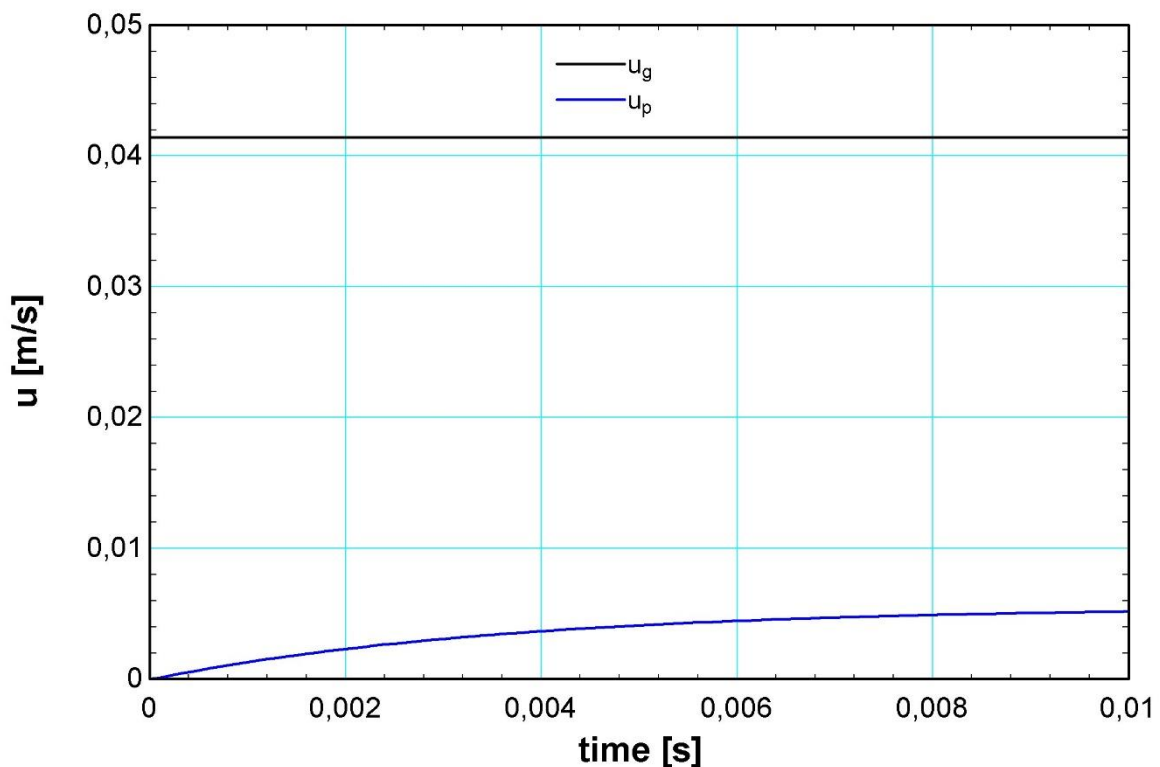


Figure 4.11 – Velocity, Case 1, $f = 0$ Hz.

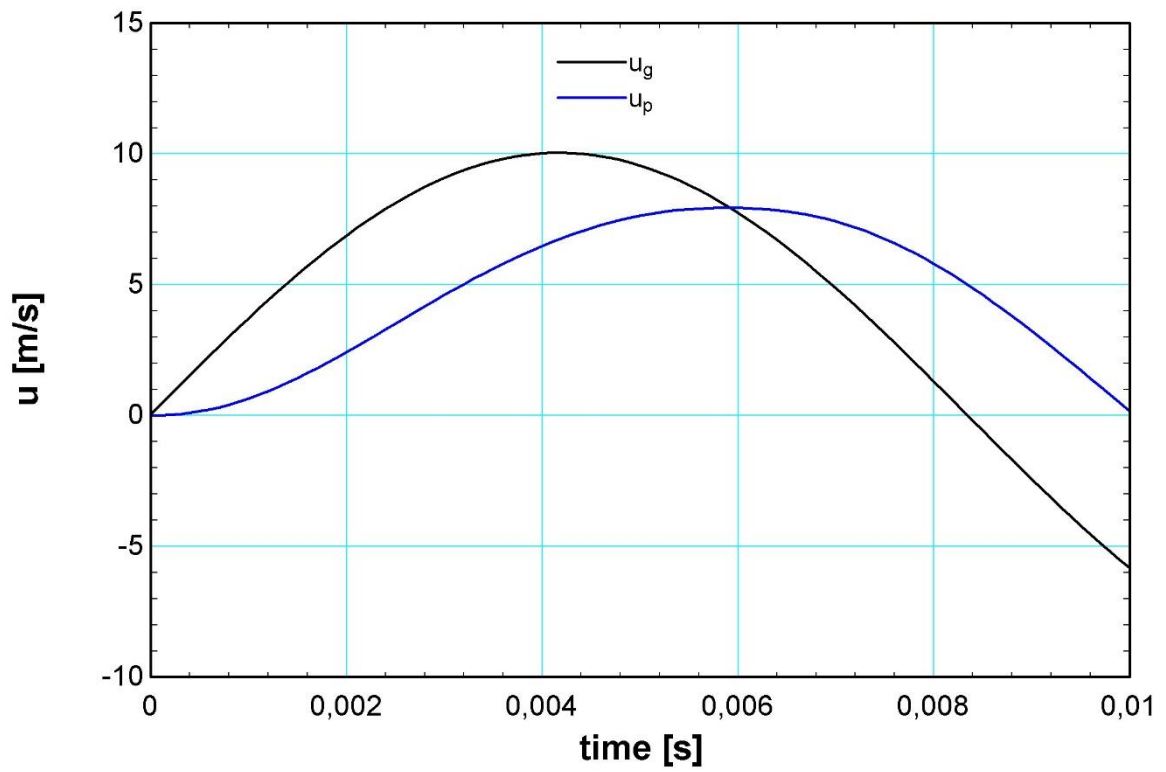


Figure 4.12 – Velocity, Case 1, $f = 60$ Hz.

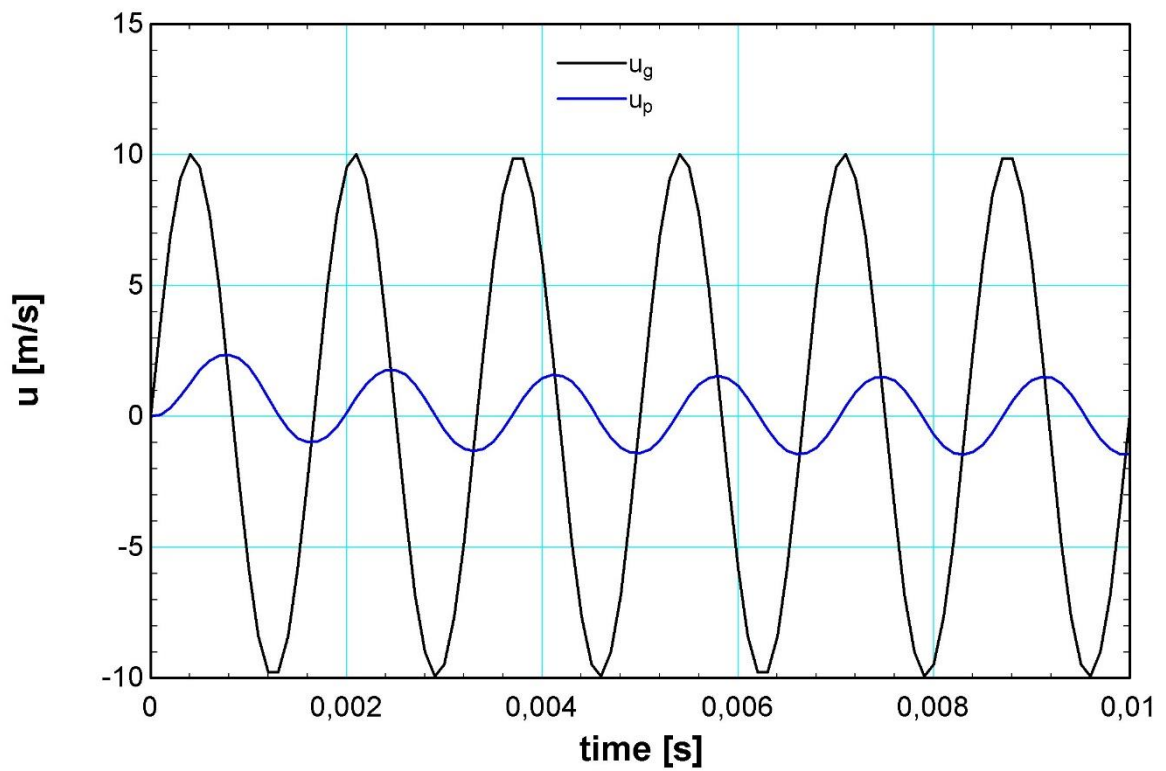


Figure 4.13 – Velocity, Case 1, $f = 600$ Hz.

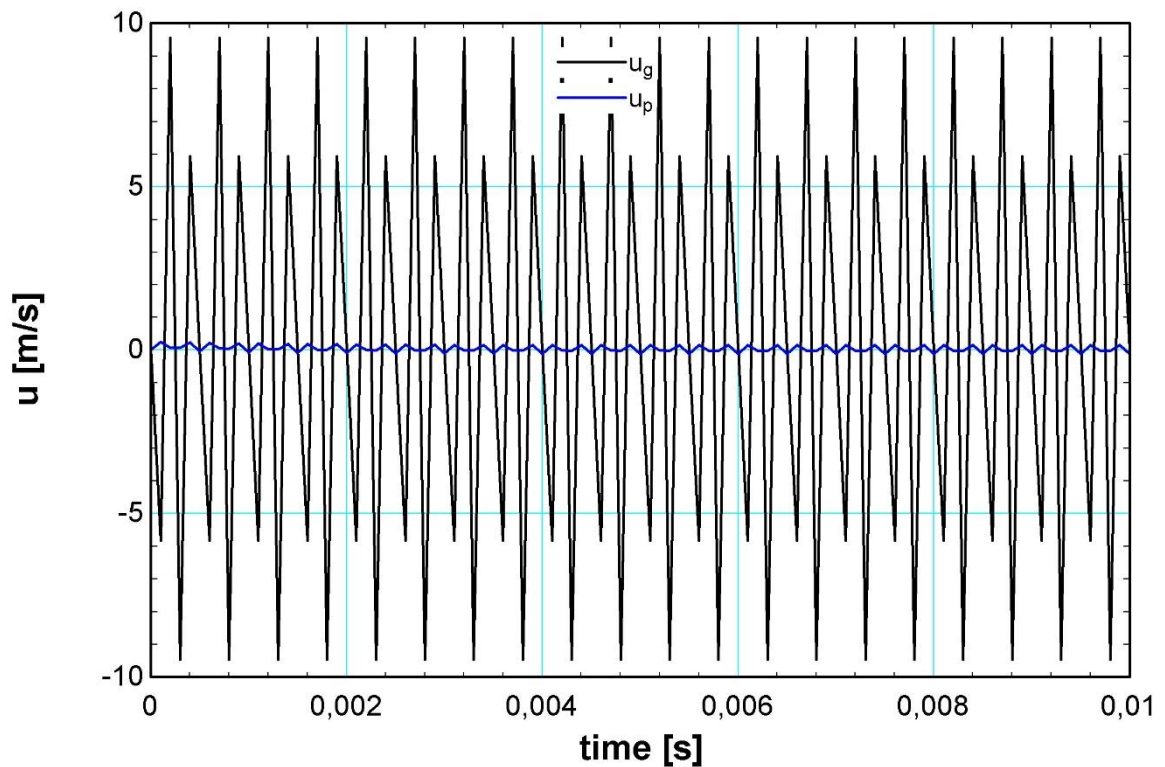


Figure 4.14 – Velocity, Case 1, $f = 6000 \text{ Hz}$.

The vertical displacement of the particle describes a trajectory significantly influenced by the oscillation frequency, the consequences are analogous to what is observed in the velocity profiles, as shown in figures 4.15, 4.16, 4.17 and 4.18. For frequencies where the particle has amplitude velocity close to the amplitude velocity of the gas, the position of the particle can vary considerably in relation to the flow without oscillation. This condition decreases as frequencies increase, leading the particle to follow the same original trajectory for very high frequencies.

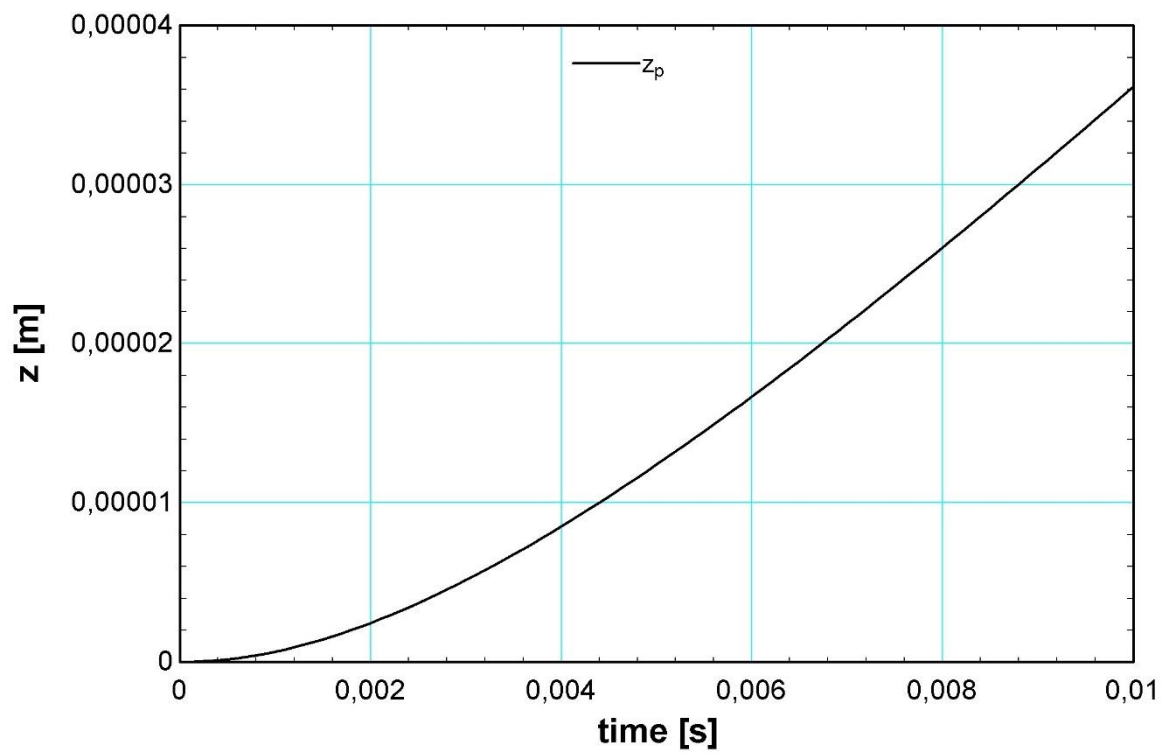


Figure 4.15 – Vertical displacement, Case 1, $f = 0$ Hz.

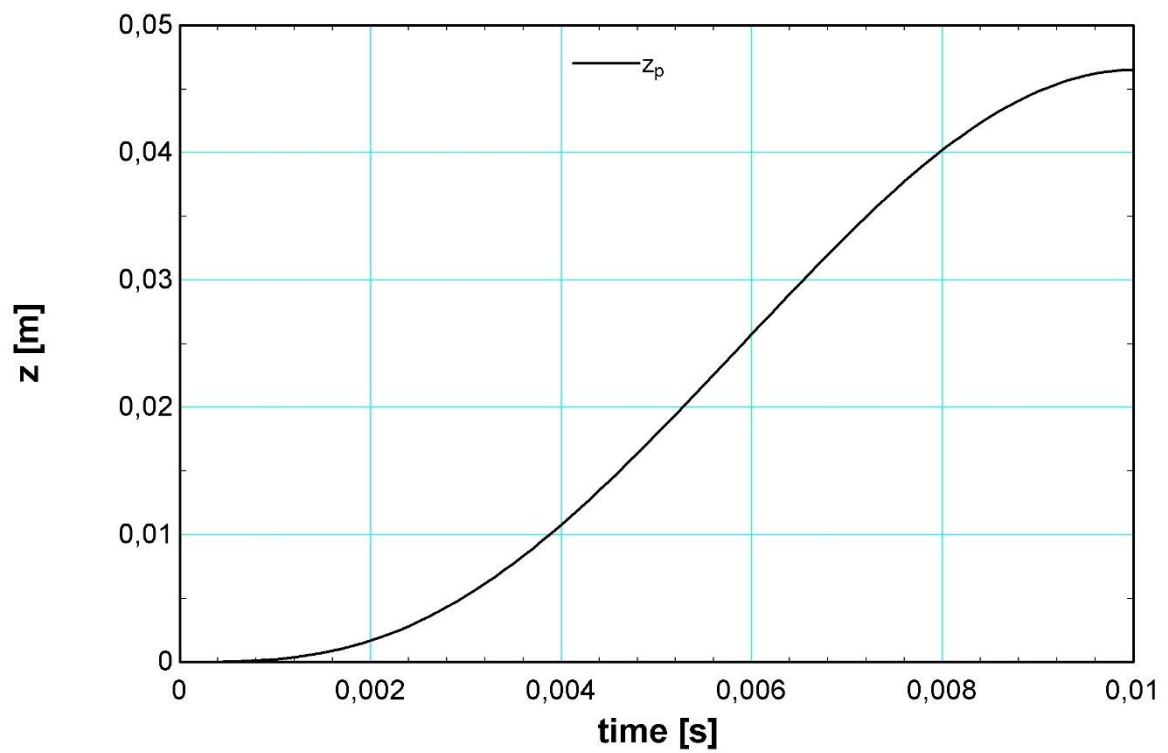


Figure 4.16 – Vertical displacement, Case 1, $f = 60$ Hz.

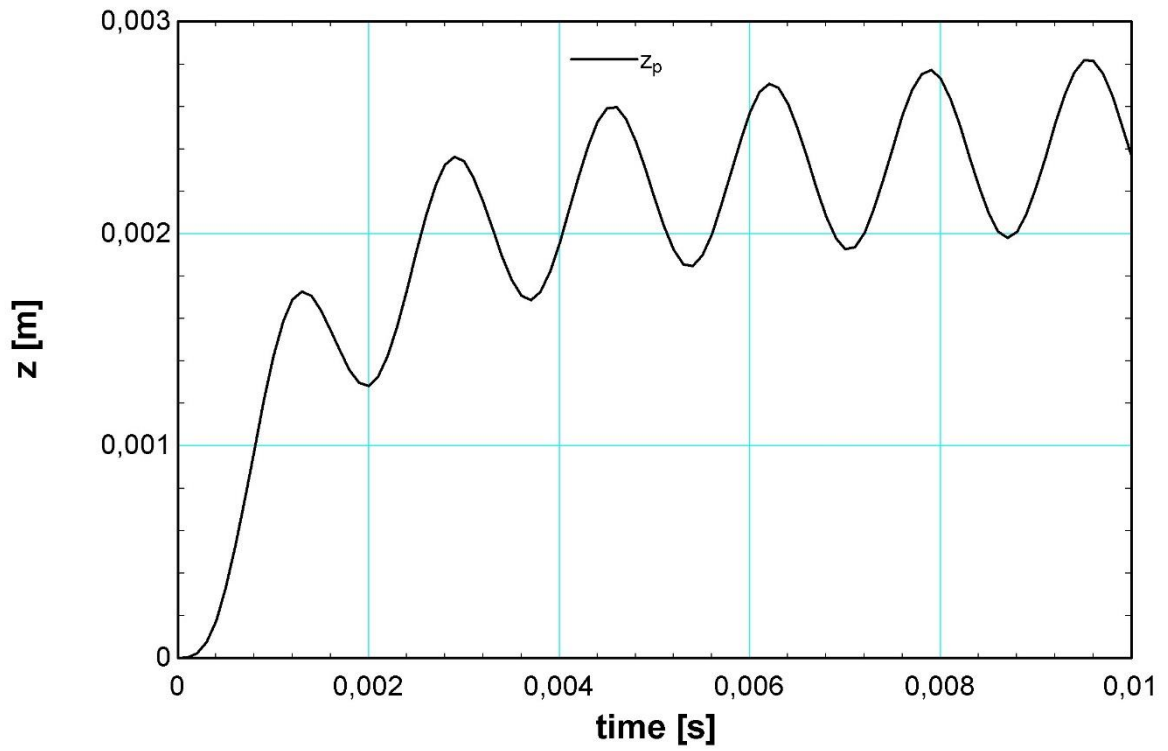


Figure 4.17 – Vertical displacement, Case 1, $f = 600 \text{ Hz}$.

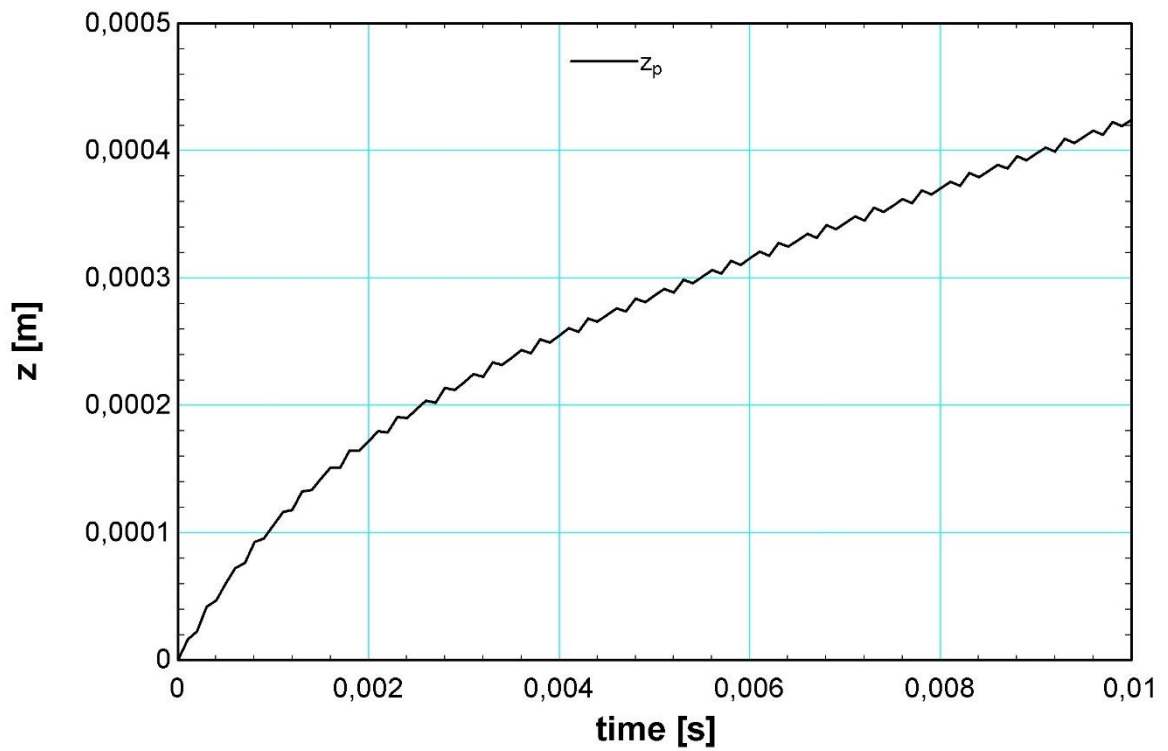


Figure 4.18 – Vertical displacement, Case 1, $f = 6000 \text{ Hz}$.

A direct consequence of the faster drying observed in figure 4.1 is the faster reduction of particle mass, on a time scale ($\sim 0,0001$) much lower than the scale observed for the occurrence of thermal degradation ($\sim 0,01$). Figure 4.19 depicts the particle yield Y_p derived solely from drying, since the start of pyrolysis has not yet been reached on this time scale, either because it is not yet in an isothermal condition and also because there is not enough time for the reaction rates to accuse the degradation of the biomass.

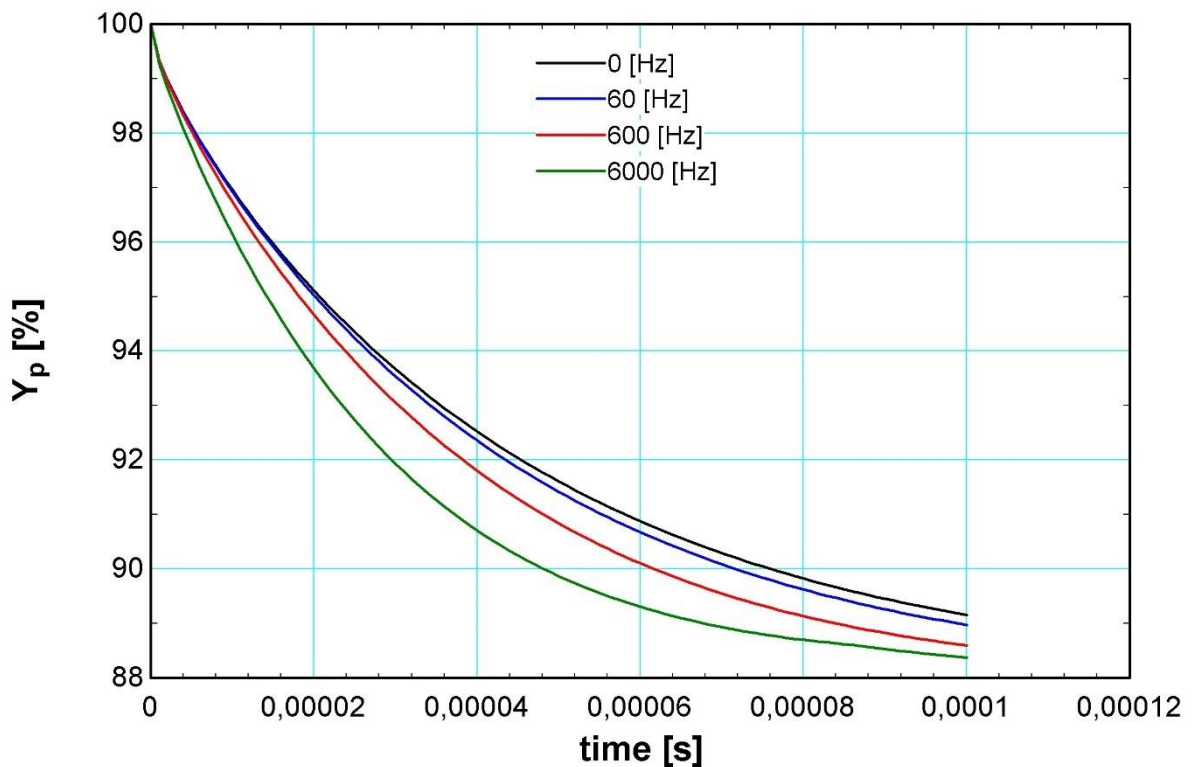


Figure 4.19 – Particle yield Y_p , Case 1.

The presence of an acoustic field makes degradation faster, as shown in the solid yield Y_s comparison between figure 4.20 and figures 4.21, 4.22 and 4.23. The values that indicate this process are very small ($\sim 10^{-6}$) and are presented on the appropriate significant figures to show its occurrence. This time measurement is suitable for verifying the effects of the acoustic field on degradation, since the characteristic time of pyrolysis in a conventional thermogravimetric analysis is infinitely greater than the time considered for the oscillations of the acoustic field.

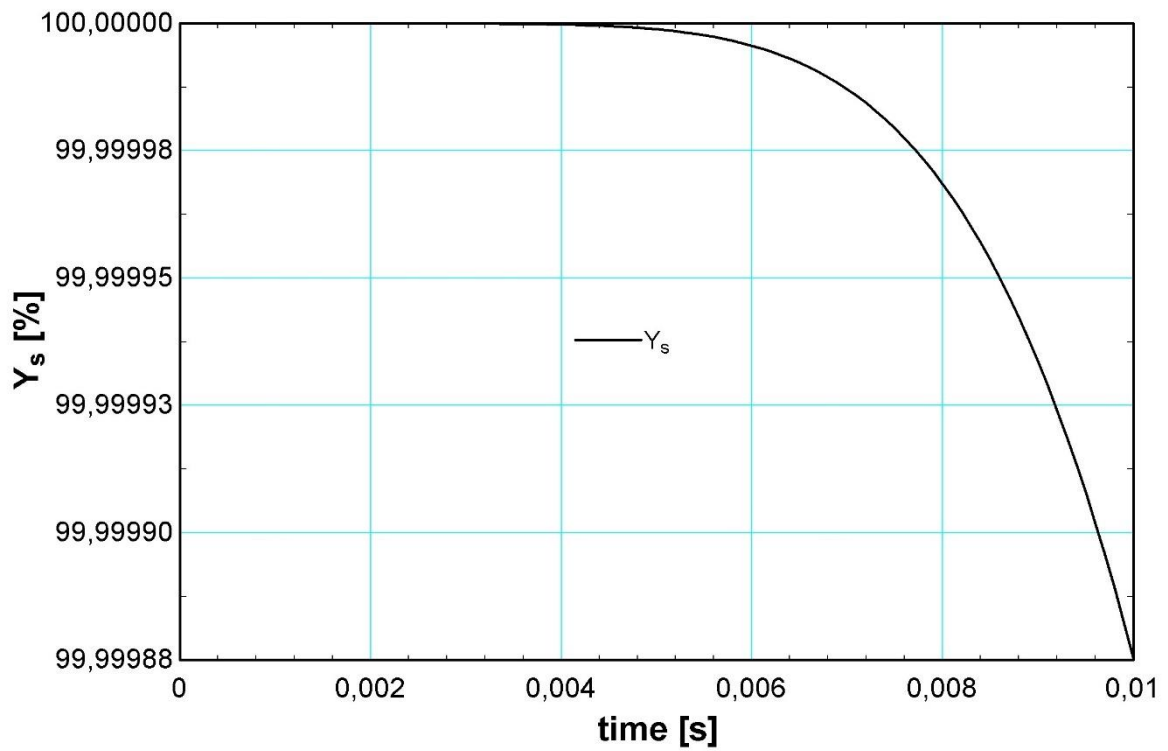


Figure 4.20 – Solid yield Y_s , Case 1, $f = 0$ Hz.

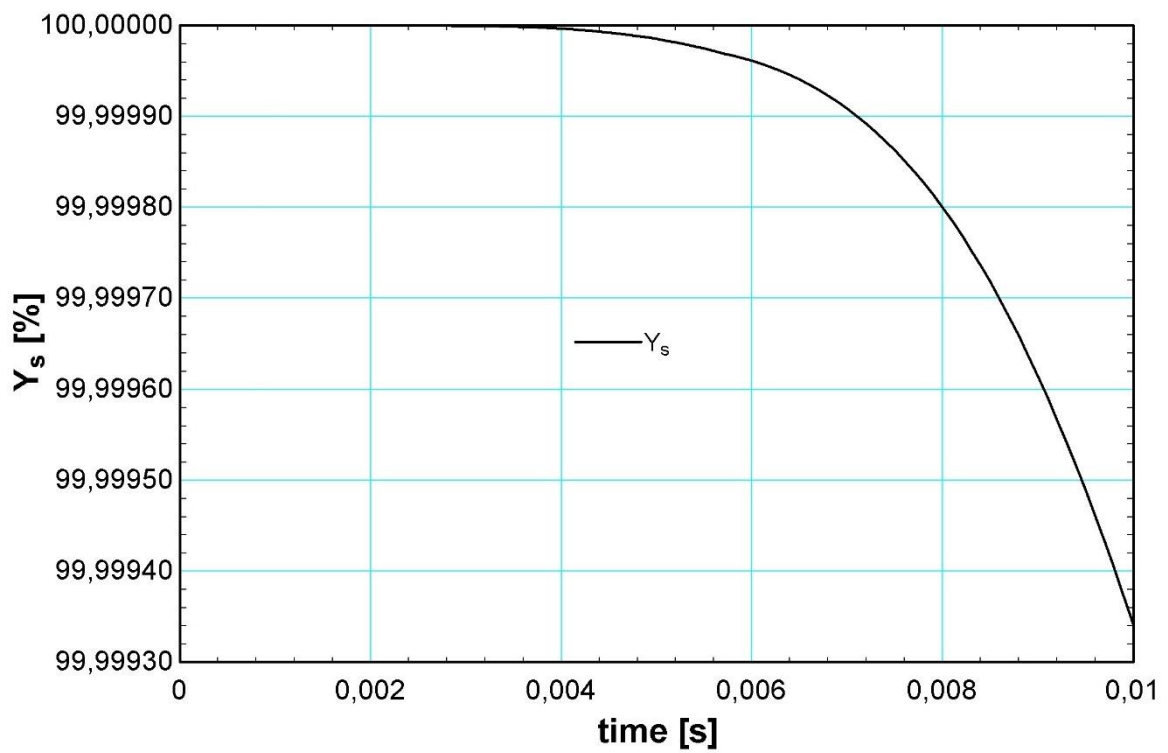


Figure 4.21 – Solid yield Y_s , Case 1, $f = 60$ Hz.

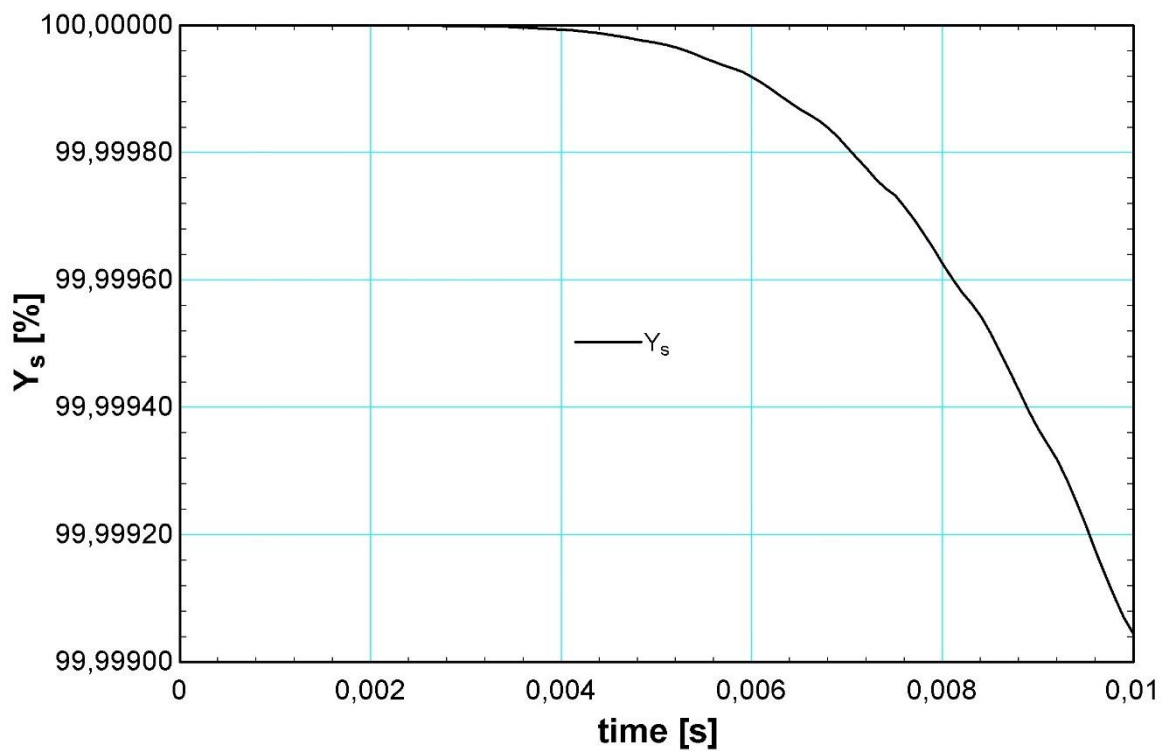


Figure 4.22 – Solid yield Y_s , Case 1, $f = 600$ Hz.

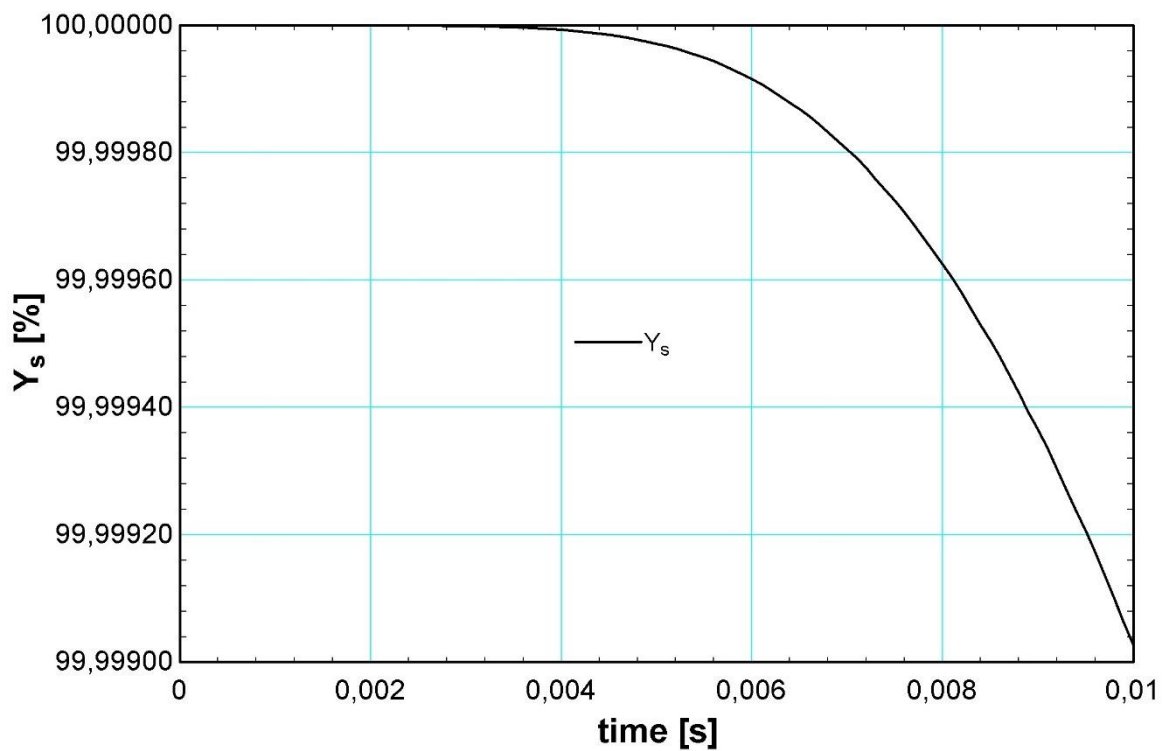


Figure 4.23 – Solid yield Y_s , Case 1, $f = 6000$ Hz.

The summary of all parameters analyzed in case 1, considering the observations and effects are in table 4.1.

Table 4.1 – Observations and effects for case 1.

Variable parameter: f [Hz]			
Parameter	Unit	Observation	Effect
C	kg/m^3	Drying rate	↑
h_m	m/s	Mass transfer	↑
T	K	Temperature change rate	↑
h_t	W/m^2K	Heat transfer	↑
u_p	m/s	Particle velocity	↑
z_p	m	Particle vertical displacement	↑
Y_p	%	Particle yield	↓
Y_s	%	Solid yield	↓

4.2 Case 2

Case 2 simulated the torrefaction of a particle of 100 μm and frequency of 6000 Hz in the presence of an acoustic field in different amplitude velocities ranges up to a maximum value of 40 m/s. The results were compared with the simulation of the same flow without the presence of oscillation. The rate of change in moisture concentration increased directly with amplitude velocity \tilde{u}_g , resulting in faster drying at higher \tilde{u}_g levels, as shown in figure 4.24.

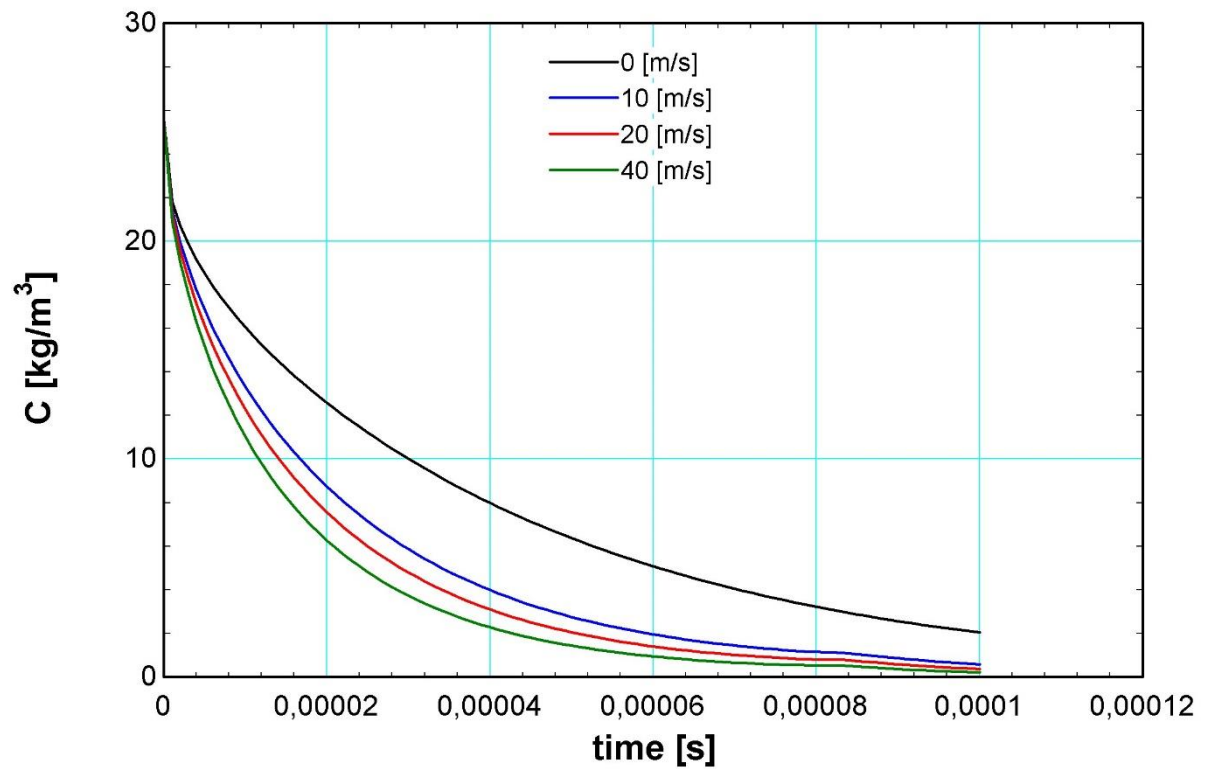


Figure 4.24 – Moisture concentration field, Case 2.

The convective mass transfer coefficient h_m increased because of variations on \tilde{u}_g , as shown in figures 4.25, 4.26, 4.27 and 4.28. Similarly, to what was observed for the frequency, the mass transfer became faster, reducing the drying time. The increase in drying rate peaked at 76%.

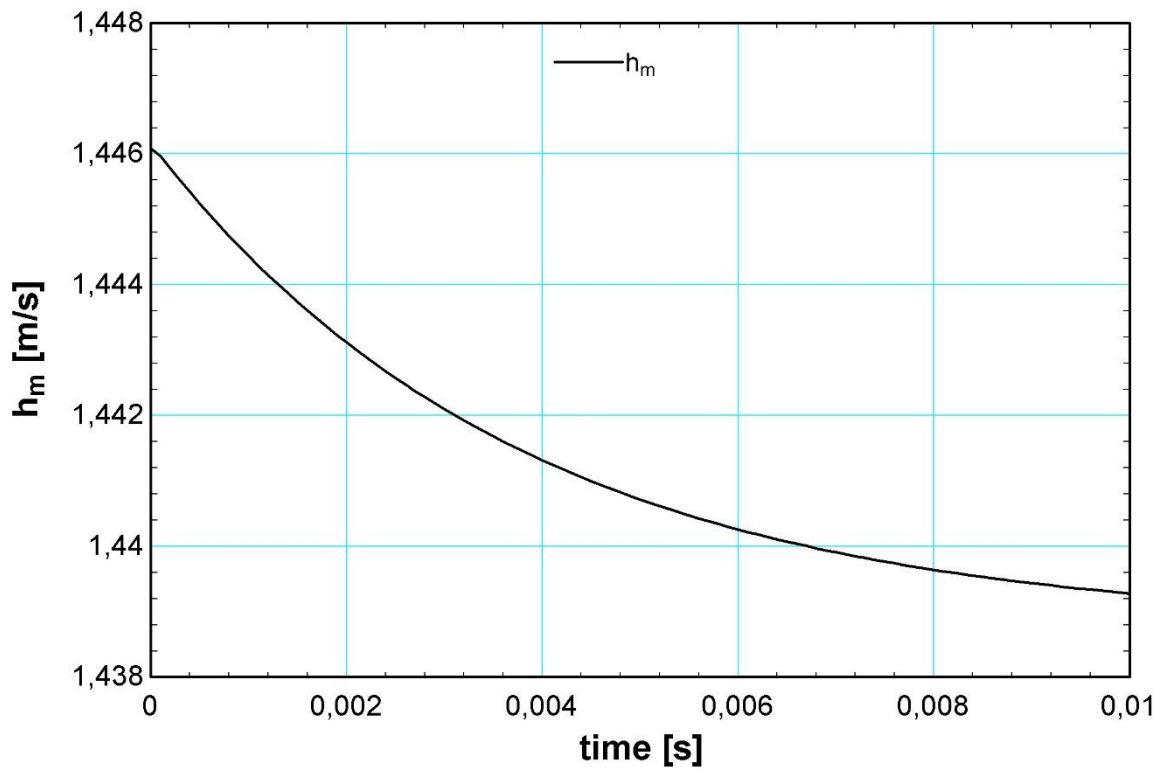


Figure 4.25 – Mass transfer coefficient, Case 2, $\tilde{u}_g = 0 \text{ m/s}$.

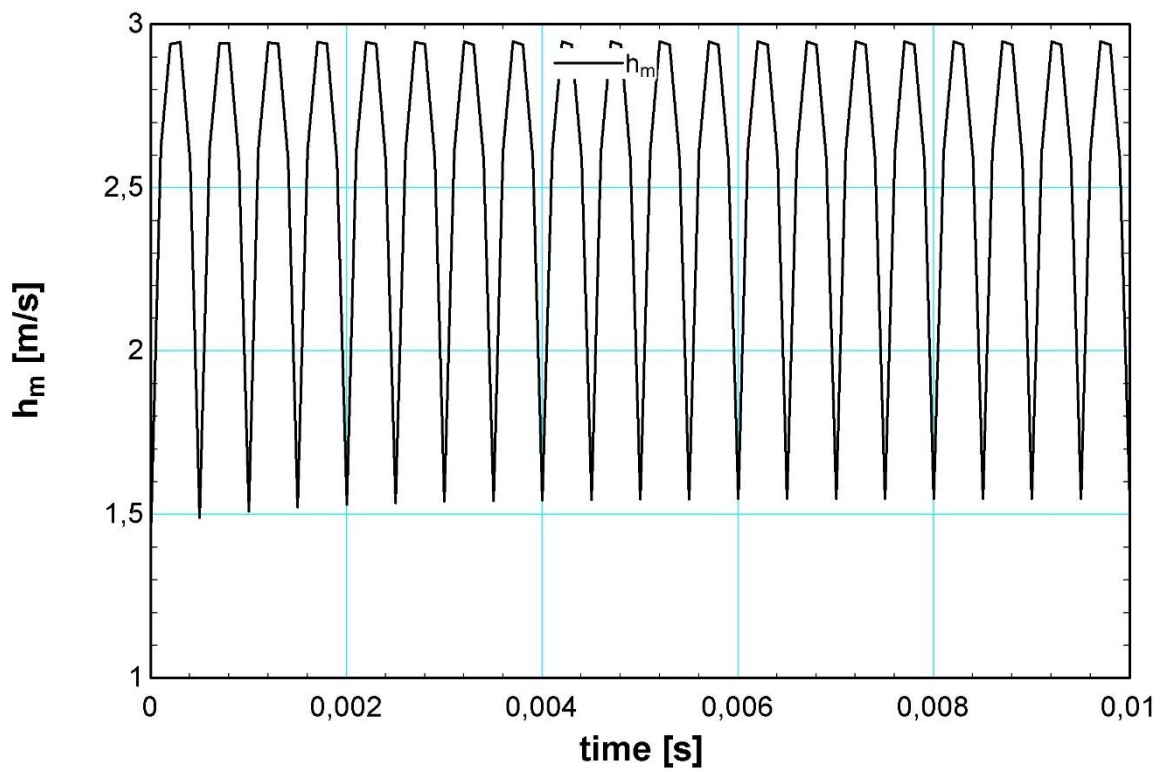


Figure 4.26 – Mass transfer coefficient, Case 2, $\tilde{u}_g = 10 \text{ m/s}$.

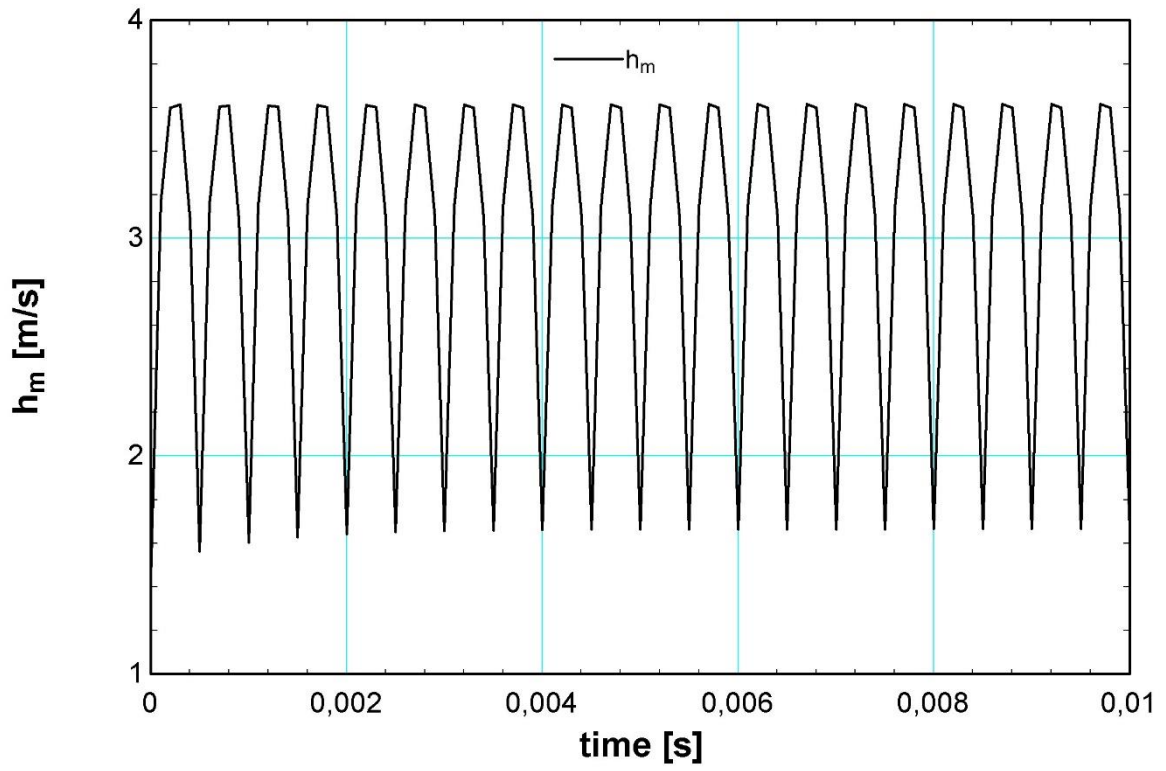


Figure 4.27 – Mass transfer coefficient, Case 2, $\tilde{u}_g = 20$ m/s.

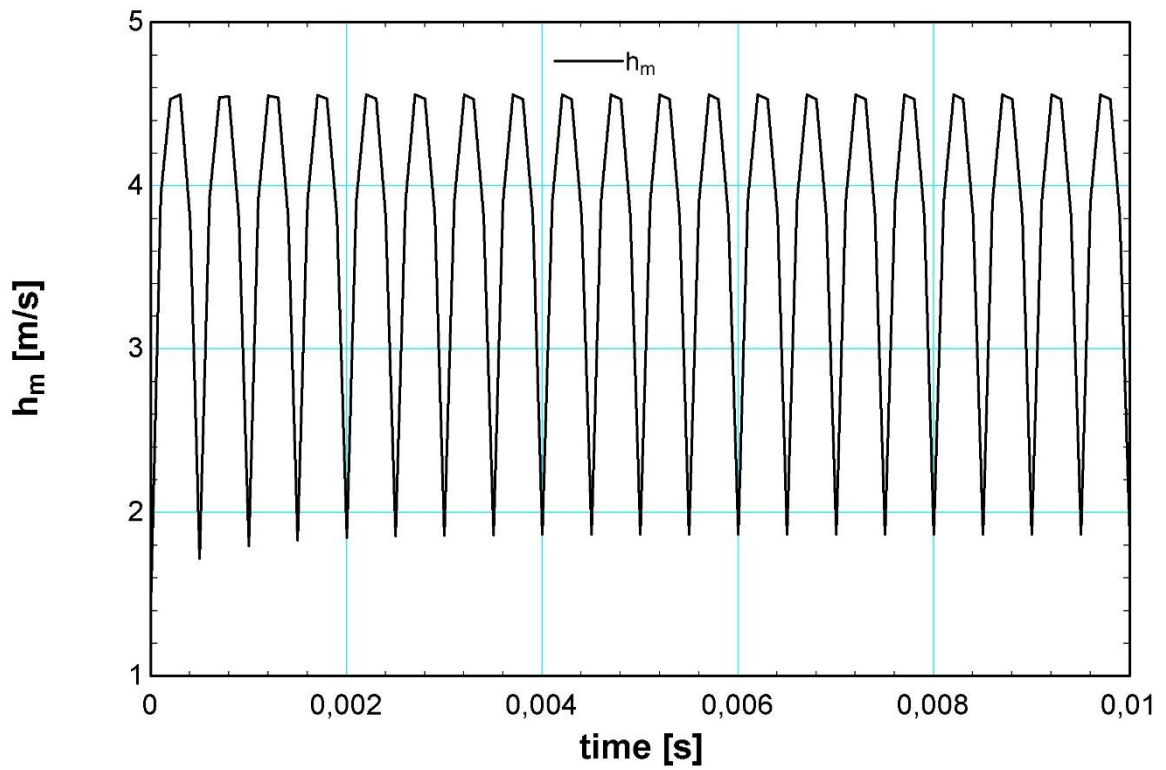


Figure 4.28 – Mass transfer coefficient, Case 2, $\tilde{u}_g = 40$ m/s.

The temperature variation rate also increased with increasing \tilde{u}_g , faster than observed for changes in frequency as shown in figure 4.29. Higher temperature levels were reached in a shorter time, due to the higher values for the convective heat transfer coefficient h_t in figures 4.30, 4.31, 4.32 and 4.33.

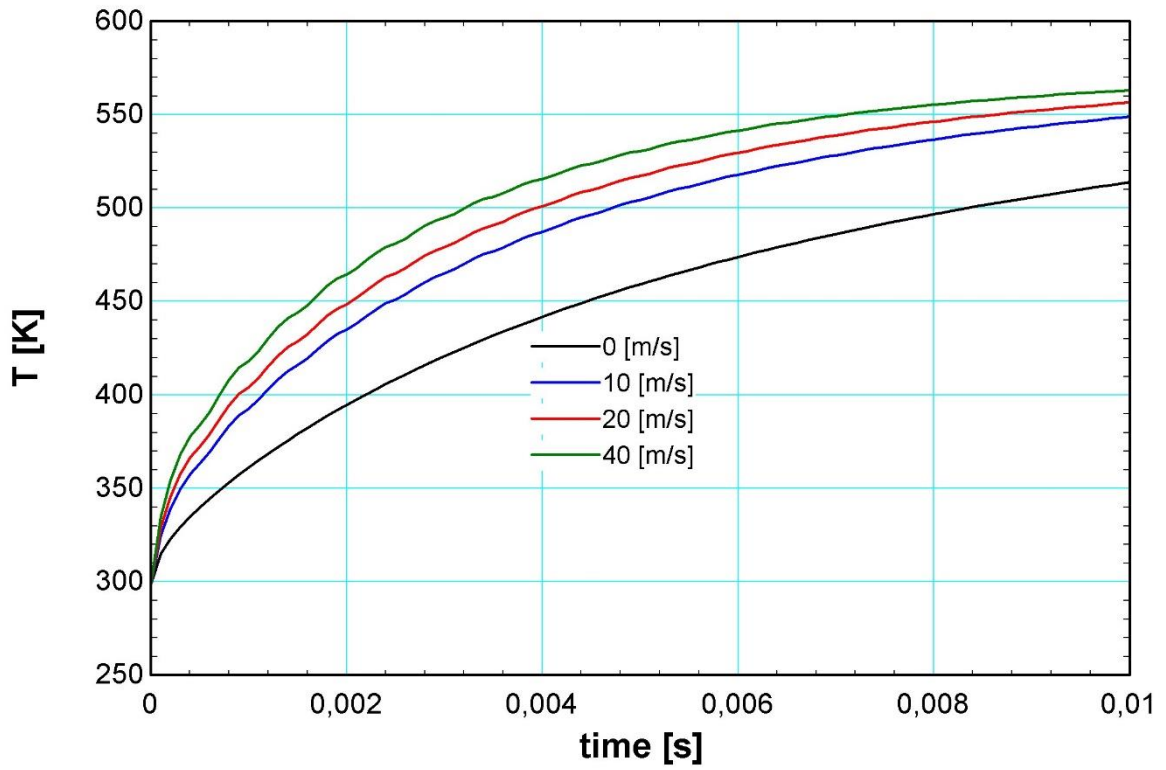


Figure 4.29 – Temperature field, Case 2.

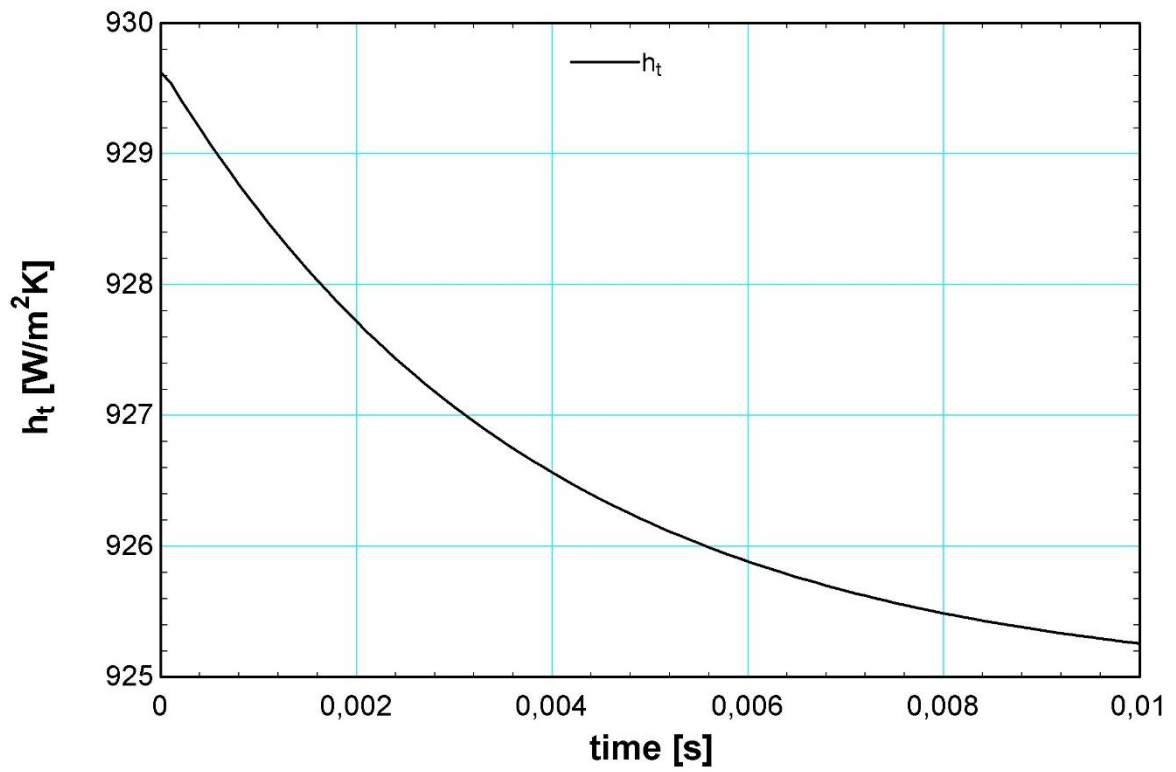


Figure 4.30 – Heat transfer coefficient, Case 2, $\tilde{u}_g = 0 \text{ m/s}$.

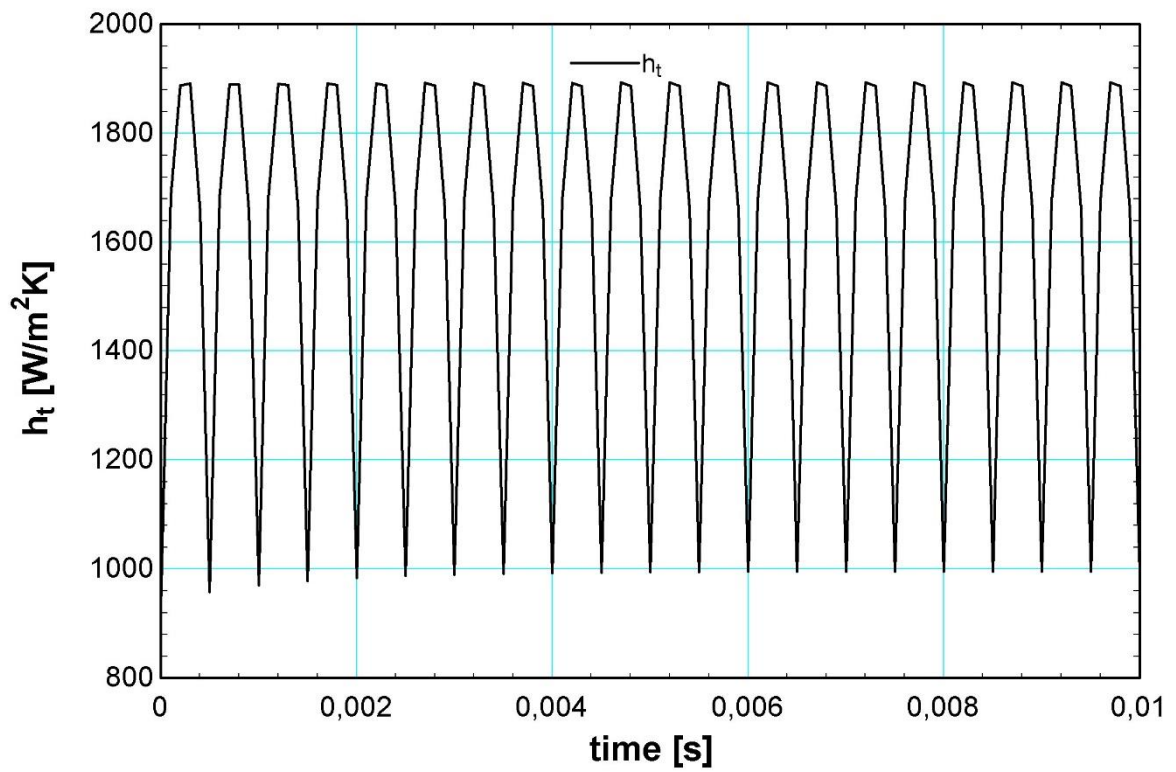


Figure 4.31 – Heat transfer coefficient, Case 2, $\tilde{u}_g = 10 \text{ m/s}$.

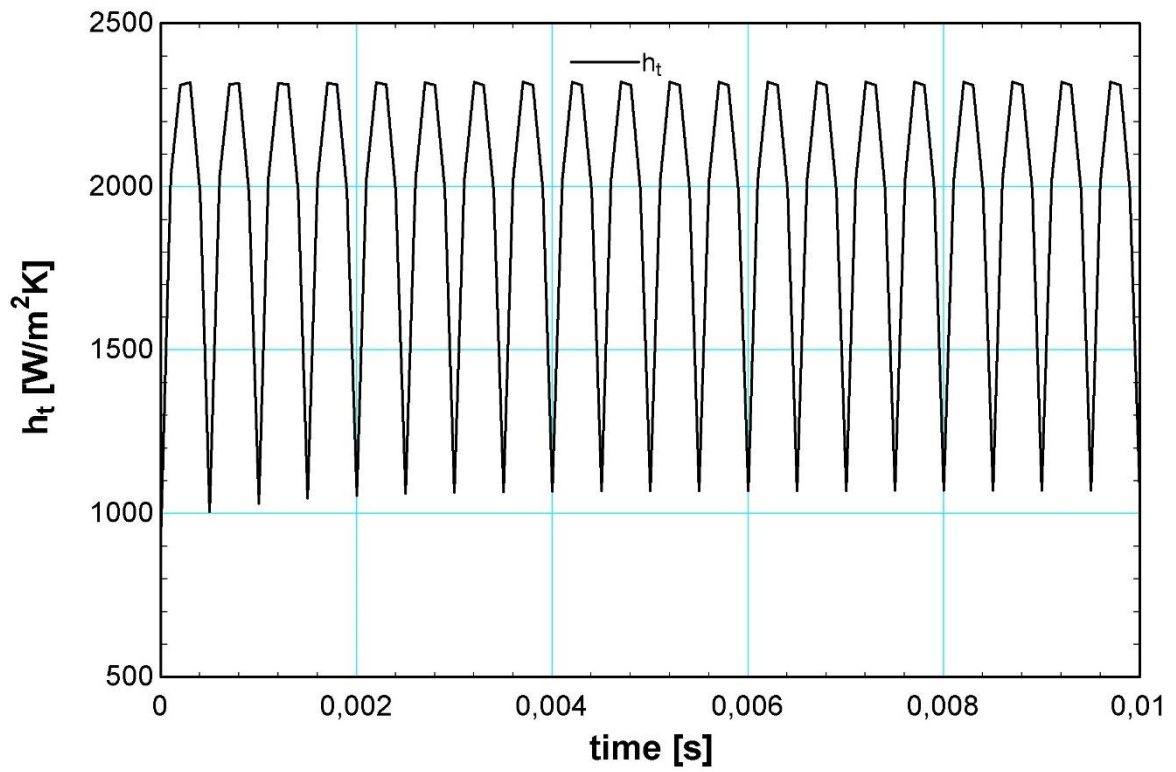


Figure 4.32 – Heat transfer coefficient, Case 2, $\tilde{u}_g = 20 \text{ m/s}$.

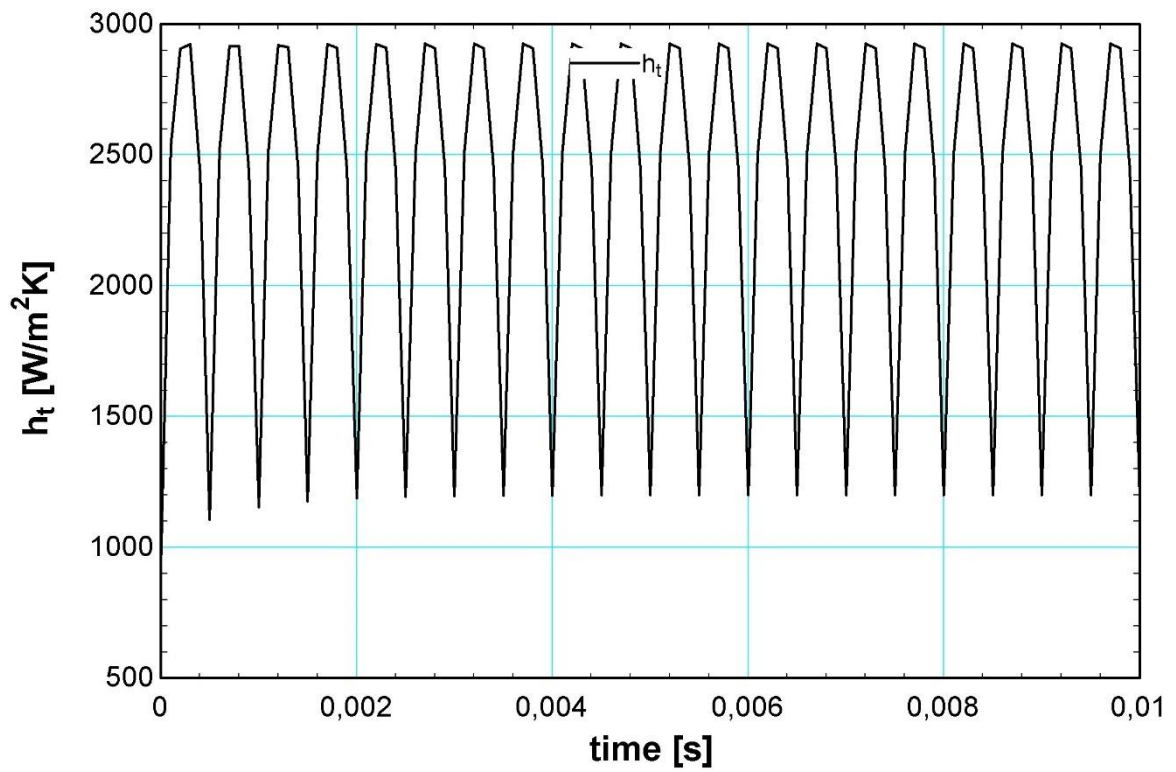


Figure 4.33 – Heat transfer coefficient, Case 2, $\tilde{u}_g = 40 \text{ m/s}$.

The velocity profiles did not change except in the absolute values. The particle amplitude velocity increased proportionally with the increase in \tilde{u}_g . This demonstrates that the changes in the profile are essentially derived from the considered frequency, since we assume \tilde{u}_g as constant. We can observe these findings in figures 4.34, 4.35, 4.36 and 4.37.

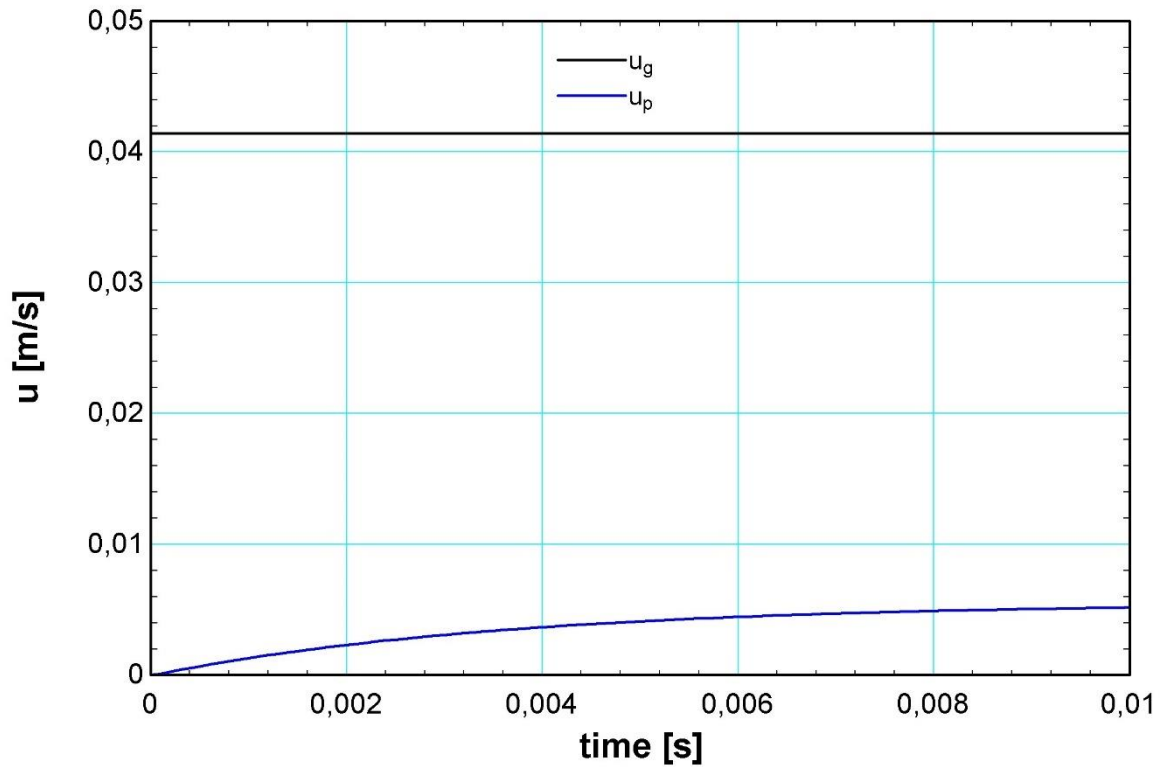


Figure 4.34 – Velocity, Case 2, $\tilde{u}_g = 0$ m/s.

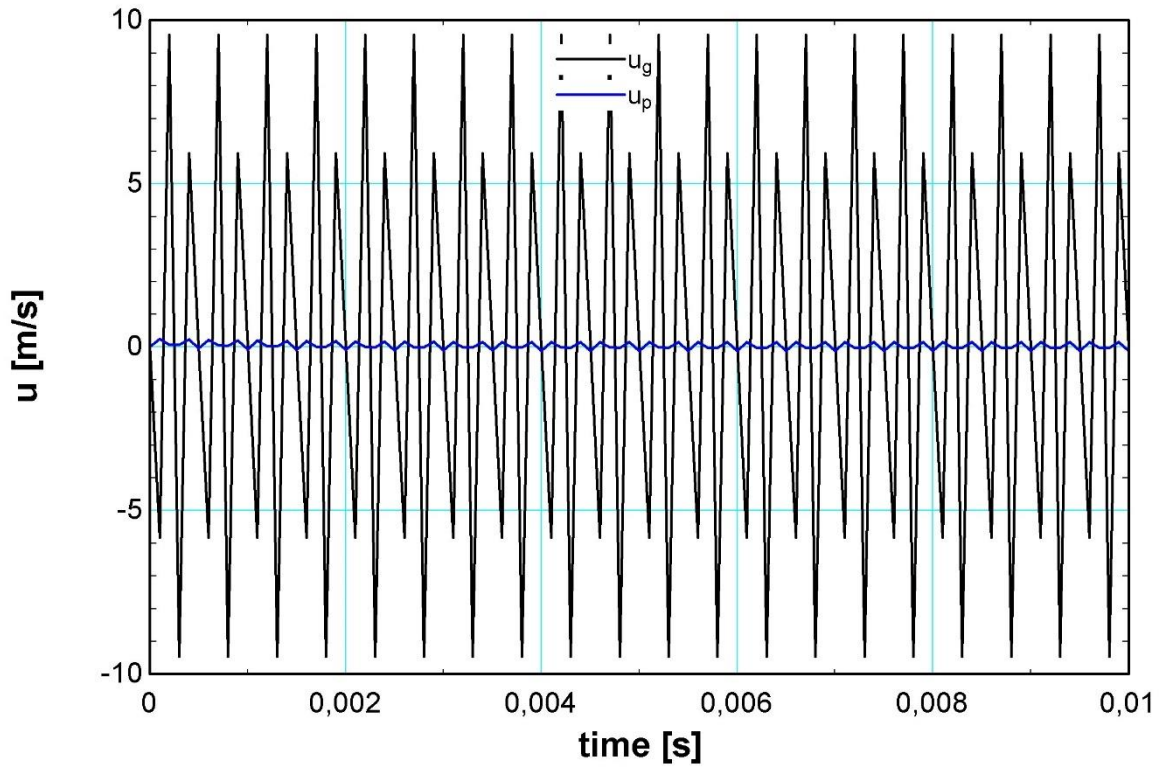


Figure 4.35 – Velocity, Case 2, $\tilde{u}_g = 10$ m/s.

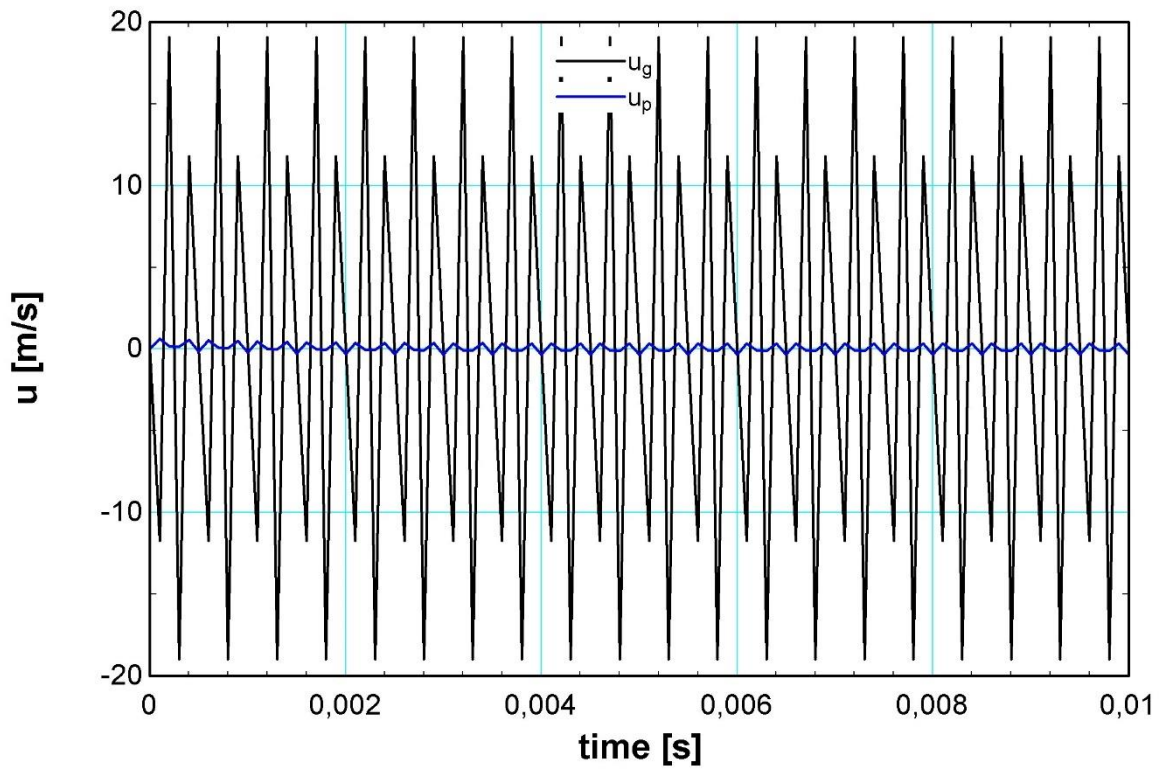


Figure 4.36 – Velocity, Case 2, $\tilde{u}_g = 20$ m/s.

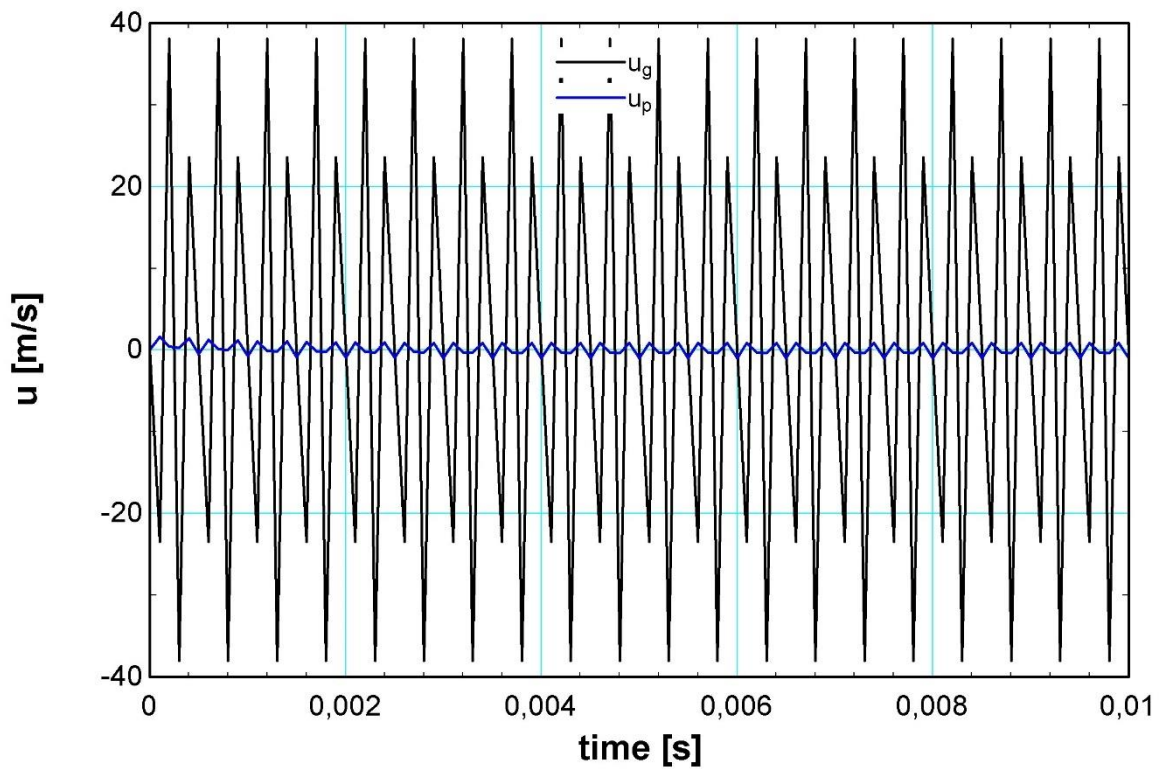


Figure 4.37 – Velocity, Case 2, $\tilde{u}_g = 40 \text{ m/s}$.

Since displacement is a primary function for velocity, the understanding of the absence of effects, except for absolute values, also applies. The \tilde{u}_g variation implies higher levels of z_p for the same time interval, as can be seen in 4.38, 4.39, 4.40 and 4.41.

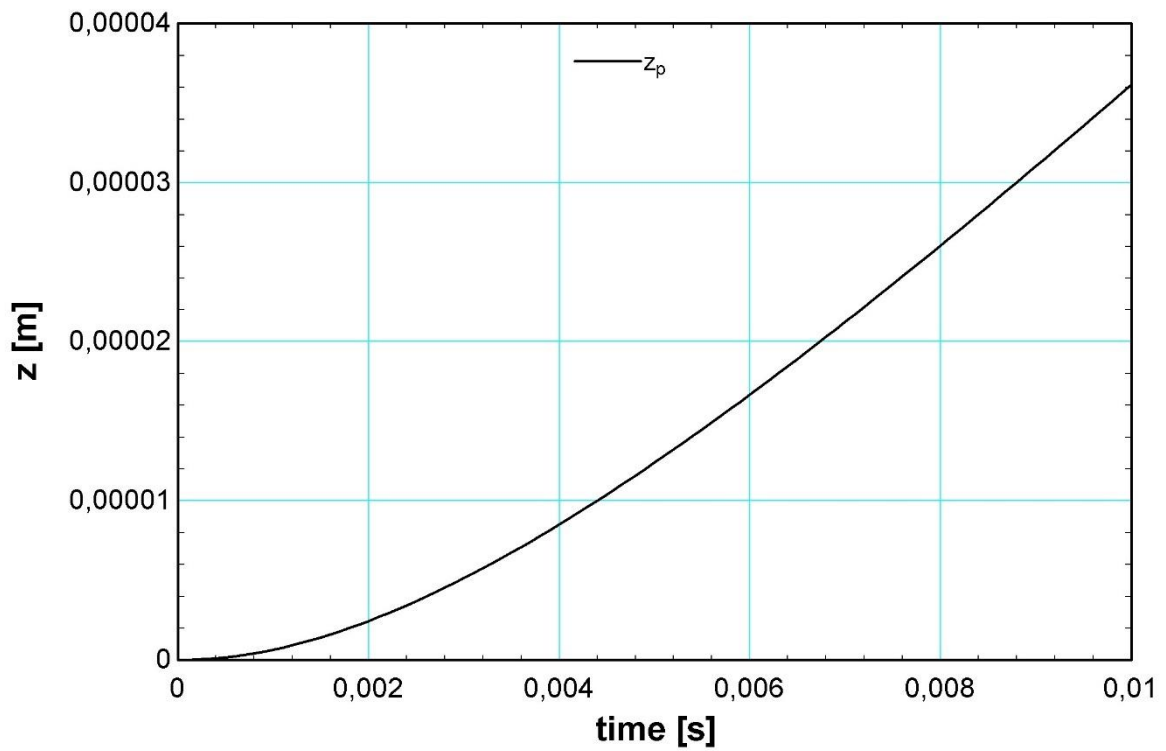


Figure 4.38 – Vertical displacement, Case 2, $\tilde{u}_g = 0$ m/s.

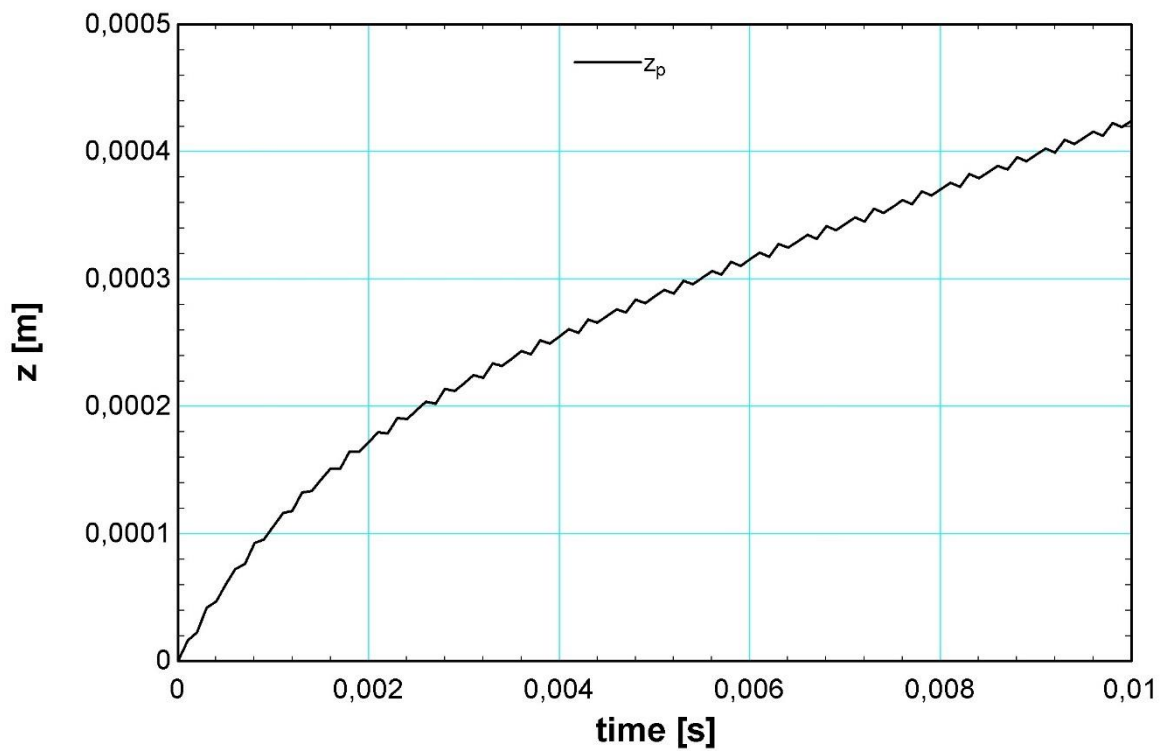


Figure 4.39 – Vertical displacement, Case 2, $\tilde{u}_g = 10$ m/s.

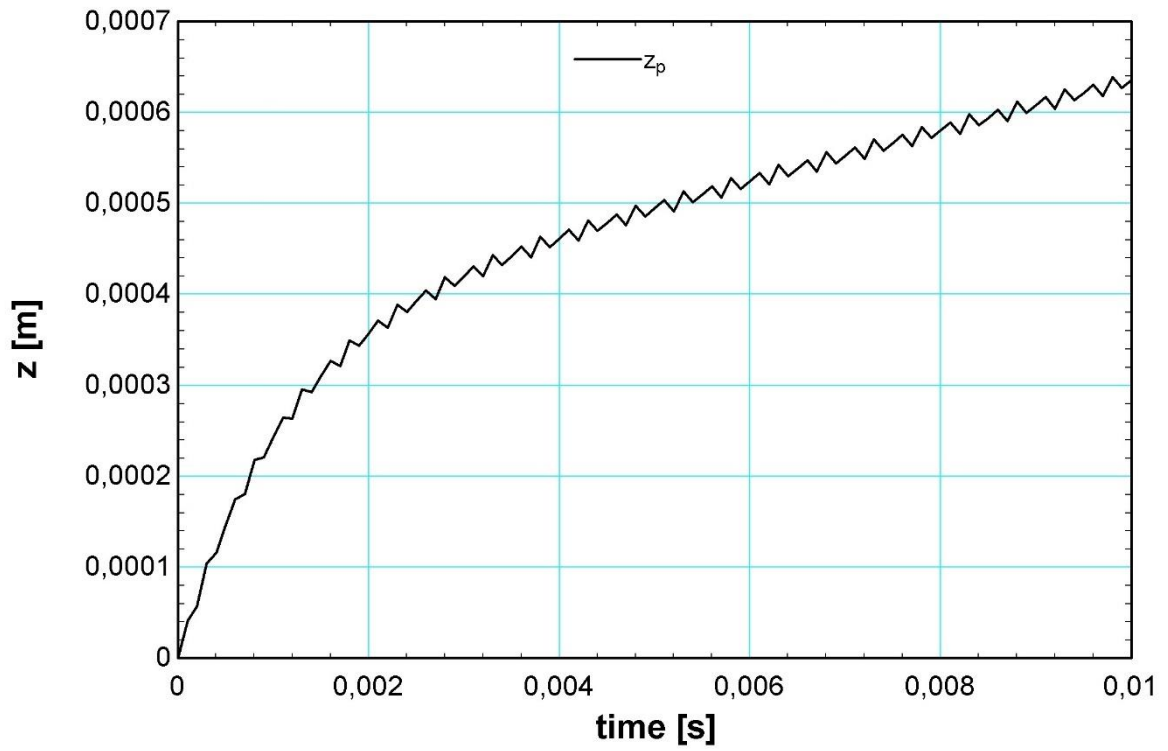


Figure 4.40 – Vertical displacement, Case 2, $\tilde{u}_g = 20$ m/s.

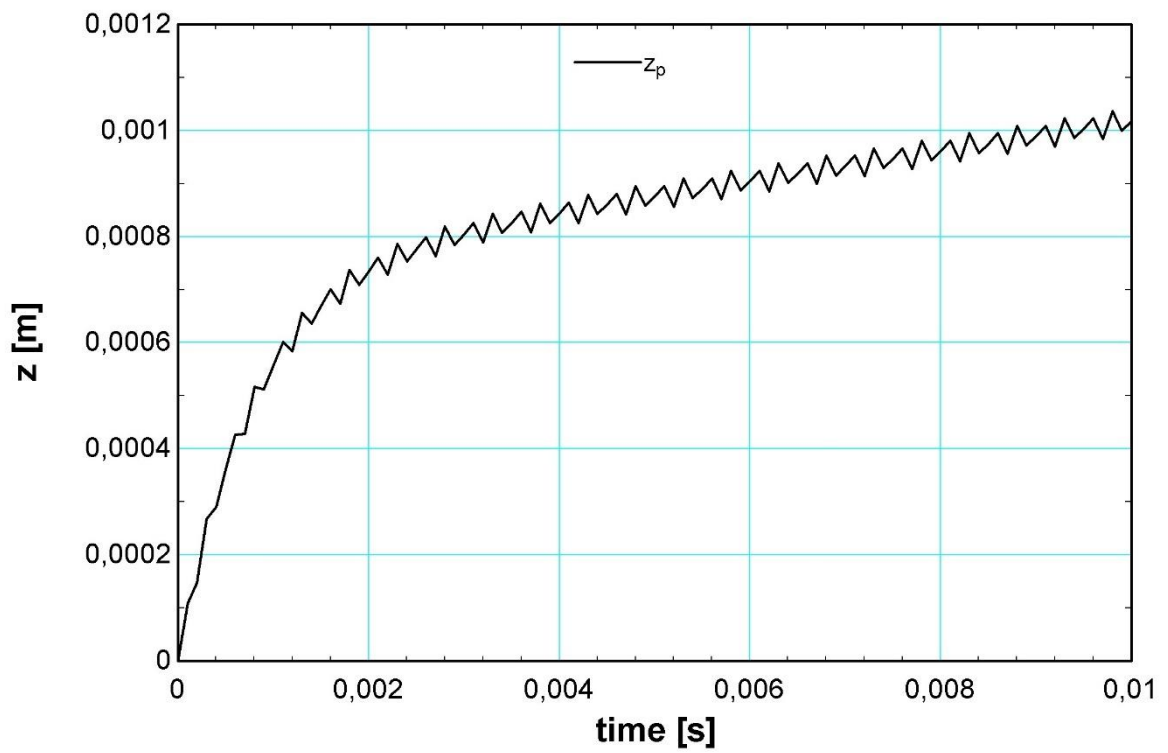


Figure 4.41 – Vertical displacement, Case 2, $\tilde{u}_g = 40$ m/s.

Faster variations in the drying process resulted in more intense Y_p reductions. These observations are described in figure 4.42.

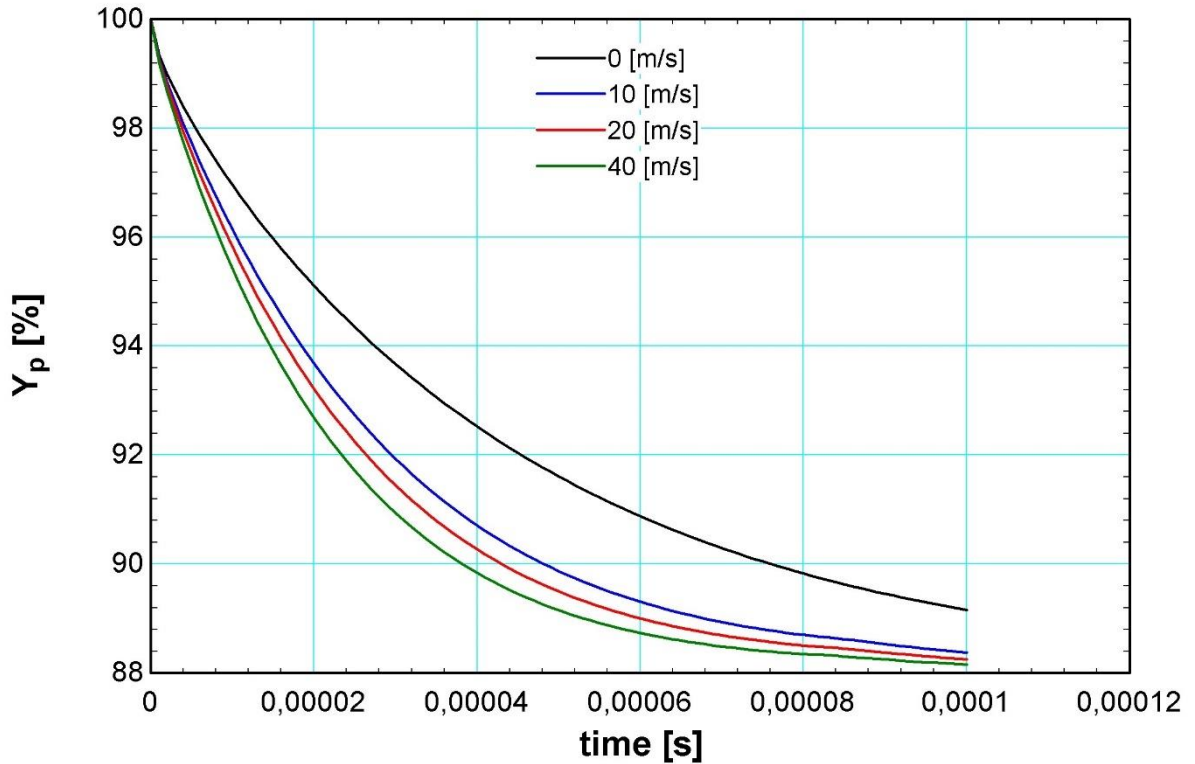


Figure 4.42 – Particle yield Y_p , Case 2.

The variation in amplitude velocity also implied a faster biomass degradation. The values, however, were not substantial to raise the changes in a higher scale than the same ones observed in the frequency change. Preserving the same significant figures adopted in Case 1, we have the values of Y_s varying as a function of \tilde{u}_g according to figures 4.43, 4.44, 4.45 and 4.46.

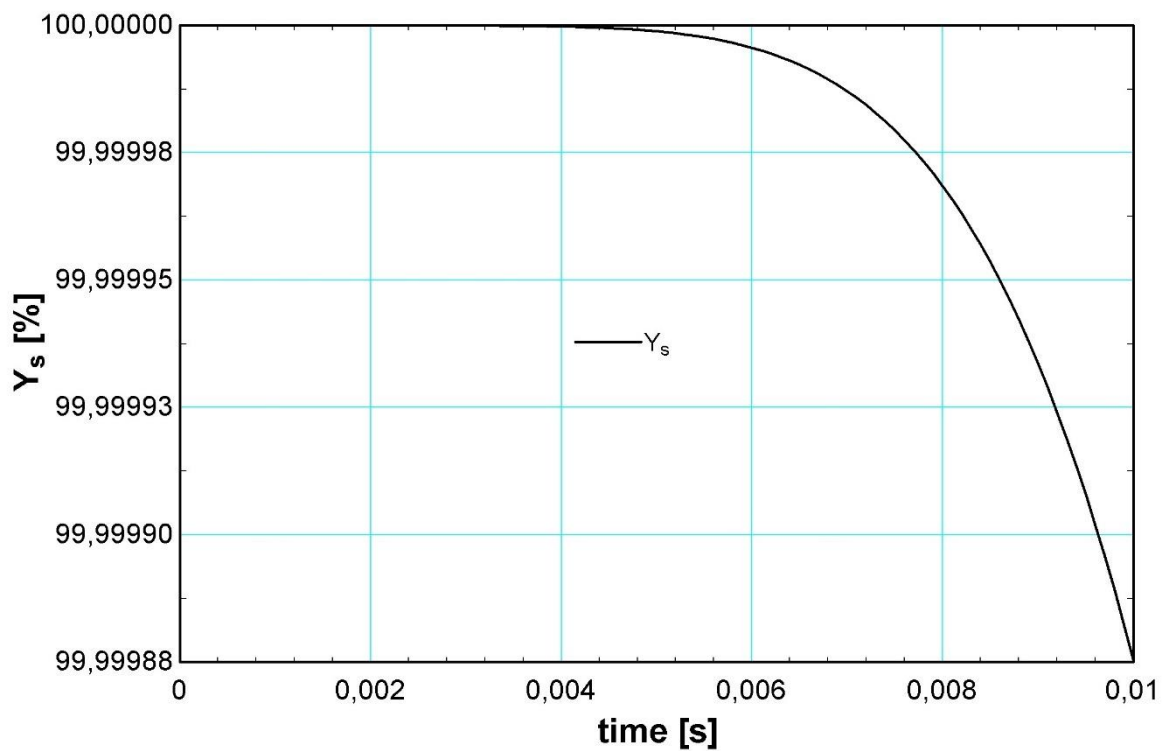


Figure 4.43 – Solid yield Y_s , Case 2, $\tilde{u}_g = 0$ m/s.

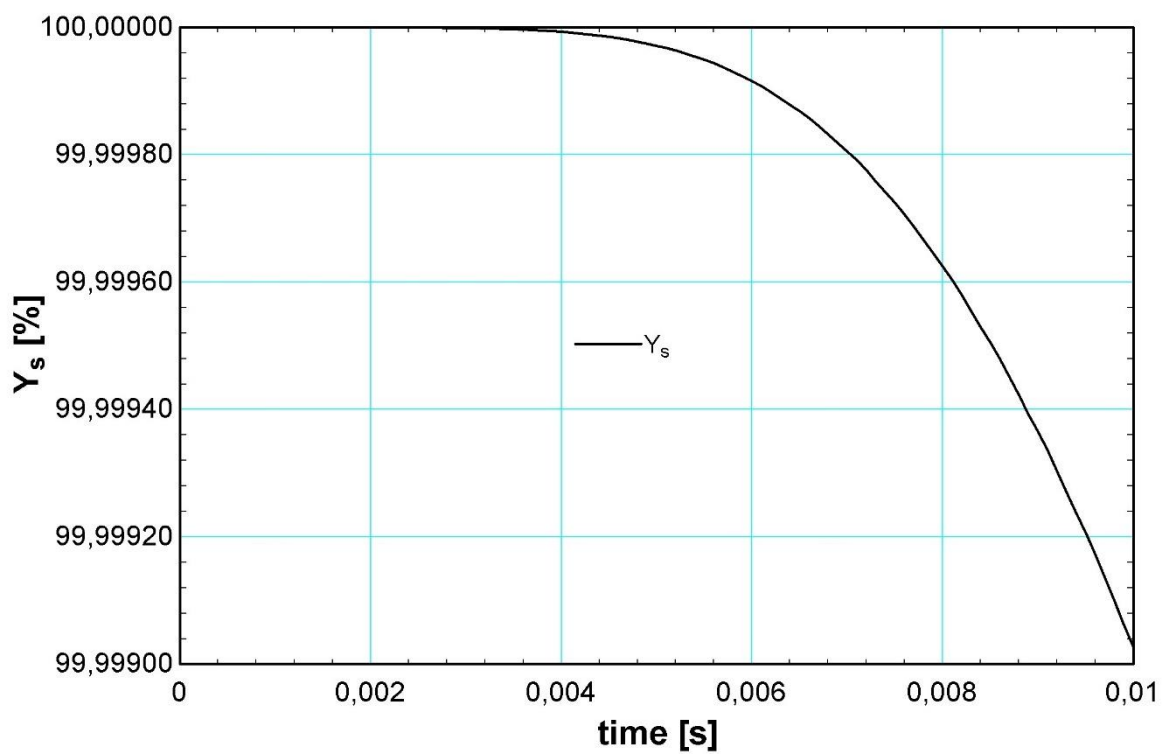


Figure 4.44 – Solid yield Y_s , Case 2, $\tilde{u}_g = 10$ m/s.

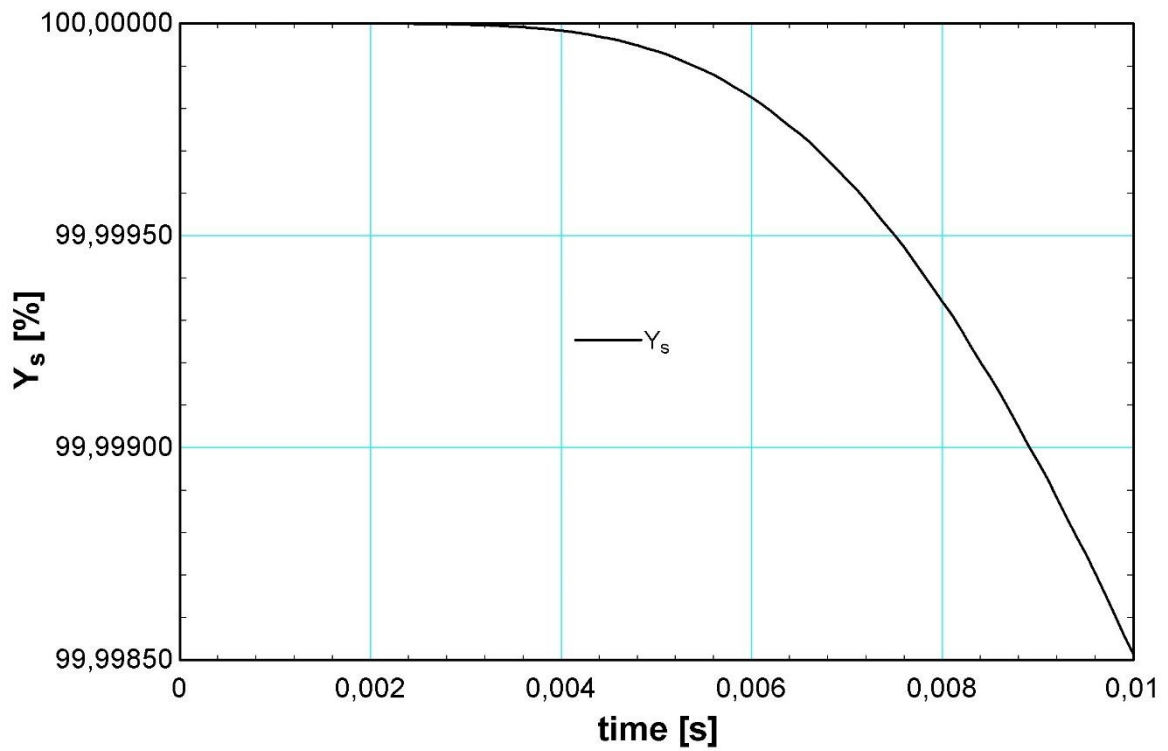


Figure 4.45 – Solid yield Y_s , Case 2, $\tilde{u}_g = 20$ m/s.

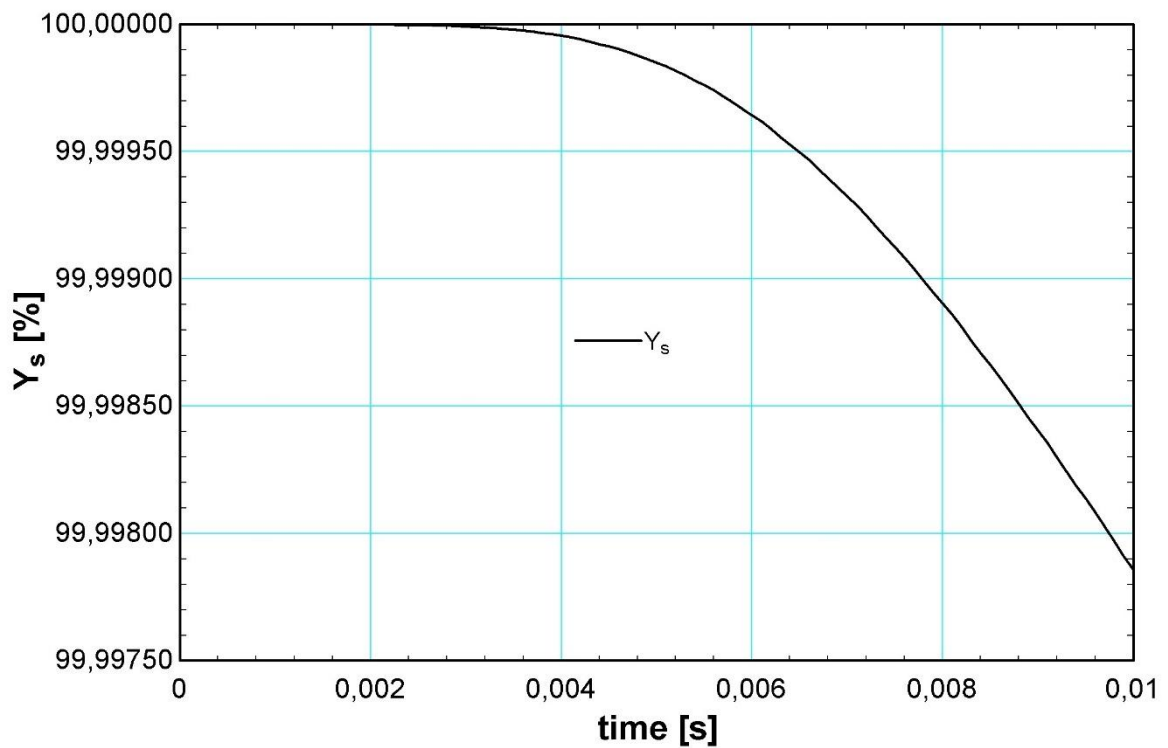


Figure 4.46 – Solid yield Y_s , Case 2, $\tilde{u}_g = 40$ m/s.

The summary of all parameters analyzed in case 2, considering the observations and effects are in table 4.2.

Table 4.2 – Observations and effects for case 2.

Variable parameter: \tilde{u}_g [m/s]			
Parameter	Unit	Observation	Effect
C	kg/m^3	Drying rate	↑
h_m	m/s	Mass transfer	↑
T	K	Temperature change rate	↑
h_t	W/m^2K	Heat transfer	↑
u_p	m/s	Particle velocity	↑
z_p	m	Particle vertical displacement	↑
Y_p	%	Particle yield	↓
Y_s	%	Solid yield	↓

4.3 Case 3

Case 3 simulated the torrefaction of particles of different sizes (50-150 μm), frequency of 60 Hz, and gas amplitude velocity of 10 m/s. The results were compared with the simulation of the same flow without the presence of oscillation. The reduction in moisture concentration, as well as the increase in temperature, is slower as particle size increases as shown in figures 4.47 and 4.48. This observation is a direct consequence of the increase in thermal capacity, implying a longer time for the particle to raise its temperature. This contributes to a lower intensity of diffusive mass and heat transport in a longer time as well, given that the model considers mass diffusivity varying as a function of temperature.

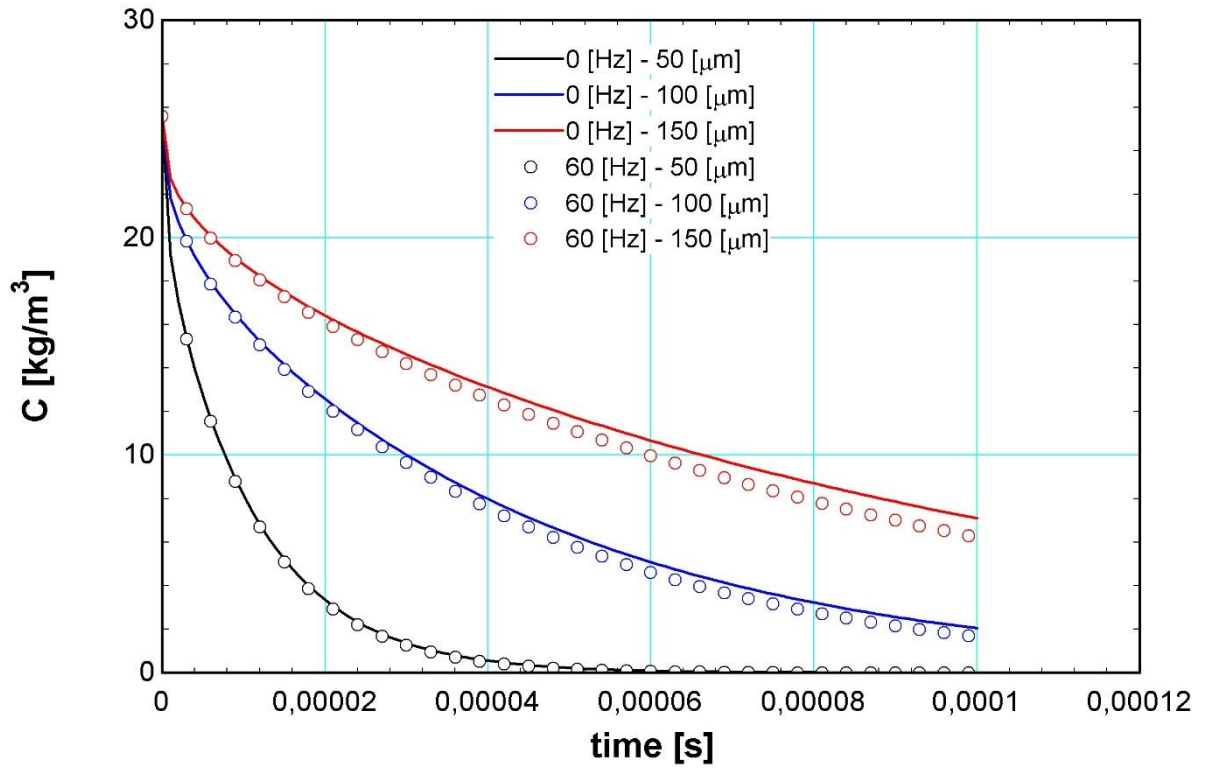


Figure 4.47 – Moisture concentration field, Case 3.

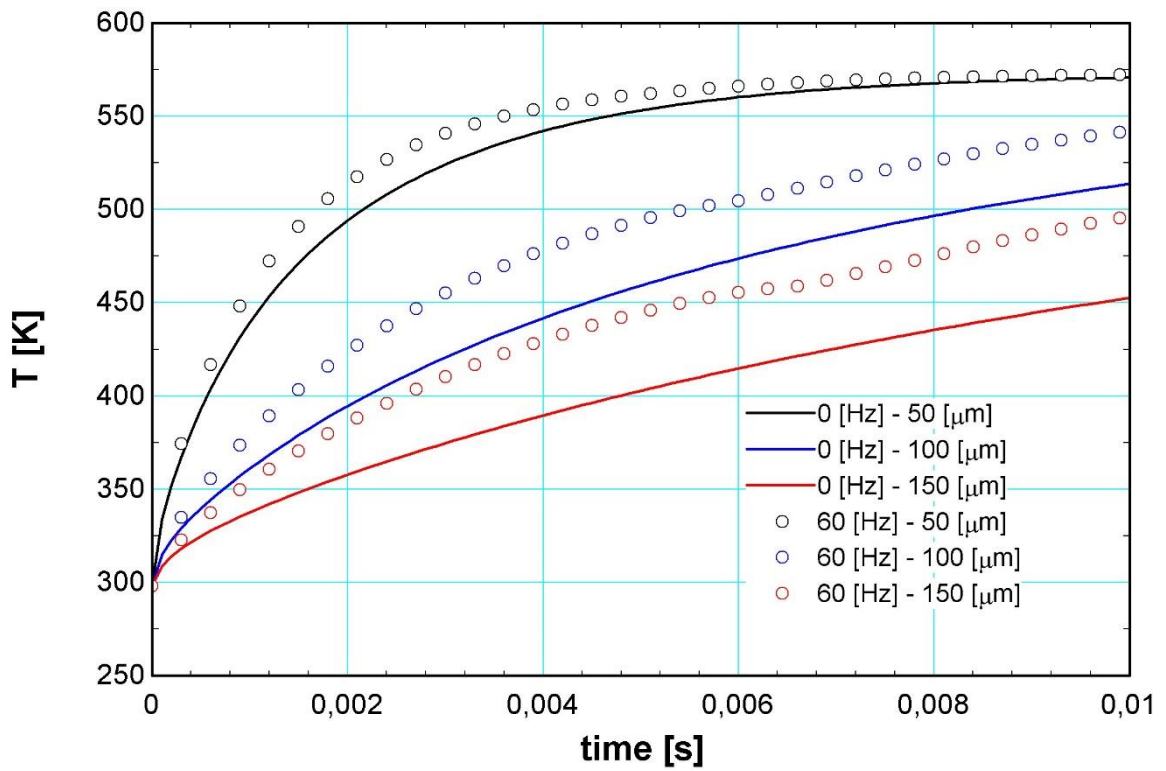


Figure 4.48 – Temperature field, Case 3.

The values of h_m and h_t decreased as the particle size increased as shown in figures 4.49 and 4.50. This is because the contact area for mass and heat flow also increases, on the order of r^2 . In this sense, the concentration and temperature gradients need to be greater and greater to maintain the same drying and heating intensity. As the external conditions of the flow are not changed, the values of h_m and h_t decreased so that the mass and energy balance are met. The effect of frequency is noticeable on larger size particles. Due to the higher displacement inertia, the relative speed is higher, implying higher h_m and h_t values.

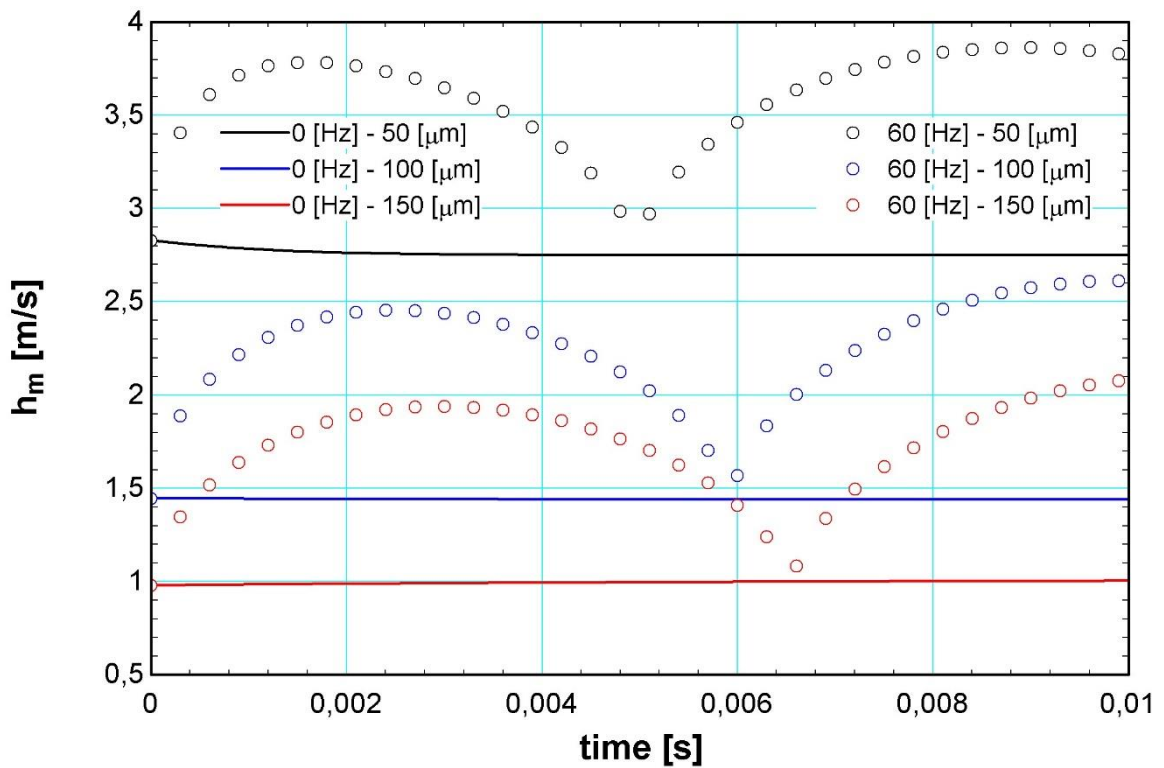


Figure 4.49 – Mass transfer coefficient, Case 3.

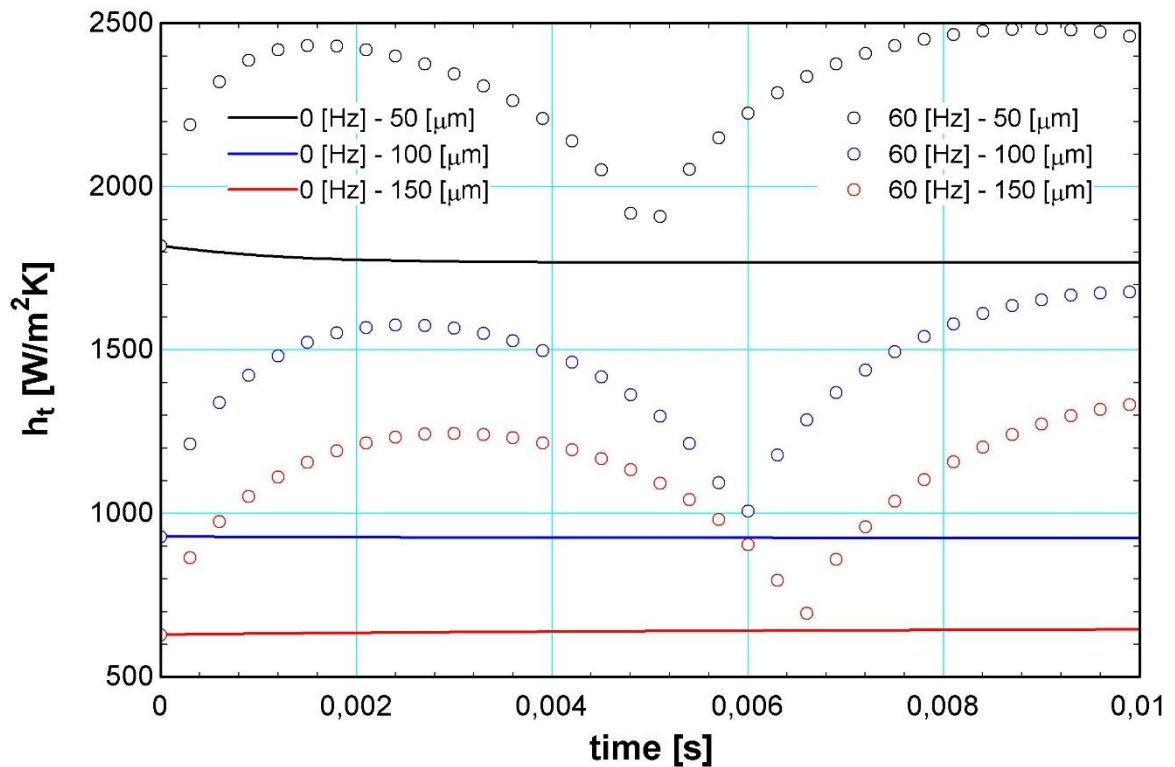


Figure 4.50 – Heat transfer coefficient, Case 3.

Maintaining the same flow, the particle size has a direct influence on the balance of forces between drag force and weight. Heavier particles need a higher velocity to maintain the same acceleration. For constant flow conditions, the particle has a lower velocity and achieve smaller displacements as it increases in size. As the model considers that the particle is free to interact with external forces, it is possible to observe in figures 4.51 and 4.52 that its velocity is negative, as well as the displacement is also for particle diameter of 150 μm and flow without acoustic oscillation. This is because the drag force propelled by the gas velocity is not enough to overcome the particle's weight.

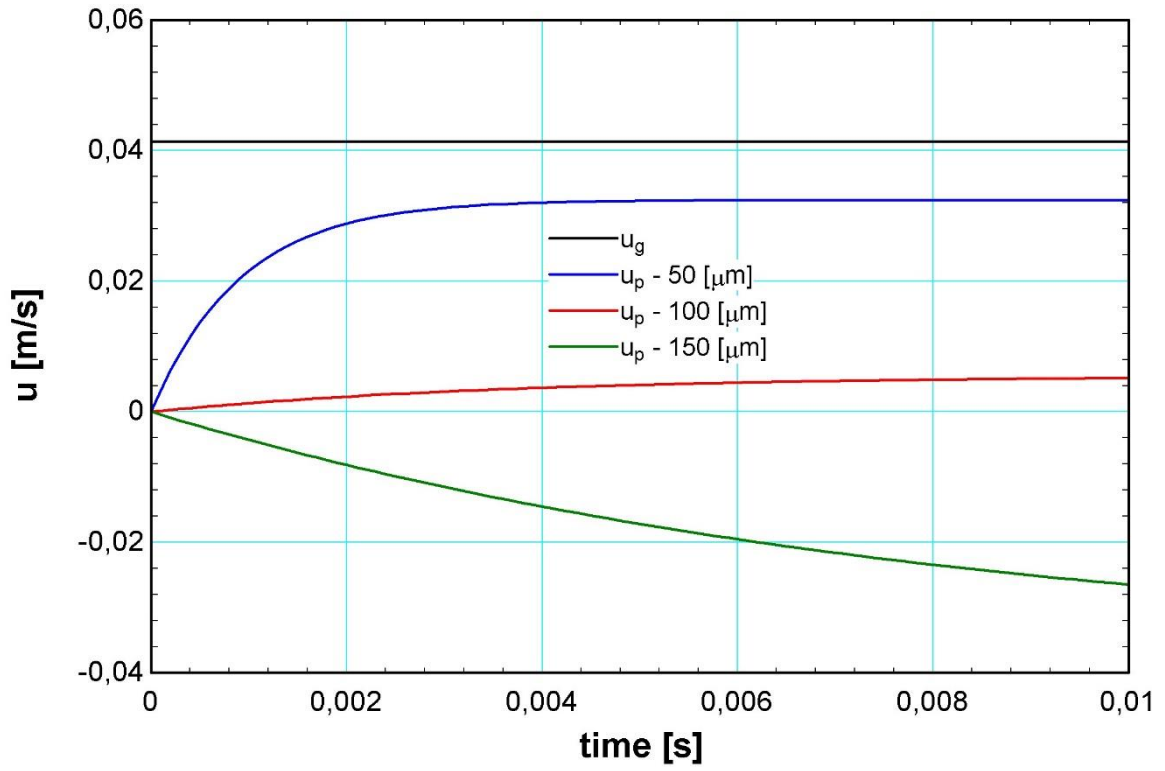


Figure 4.51 – Velocity, Case 3, $f = 0$ Hz.

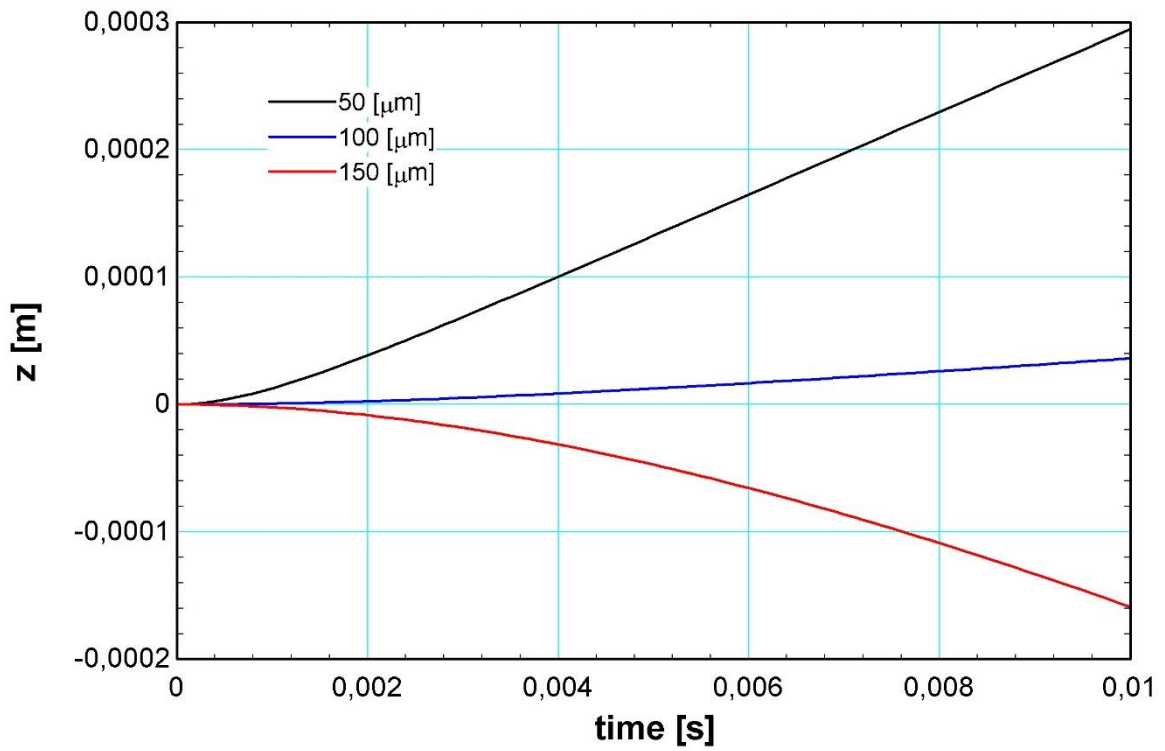


Figure 4.52 – Vertical displacement, Case 3, $f = 0$ Hz.

With the application of the acoustic field, it is observed that even for the larger particle, its velocity does not abruptly detach from the gas velocity. This occurs due to the presence of pressure waves that provide additional forces for the particle to follow an upward movement, as shown in figures 4.53 and 4.54.

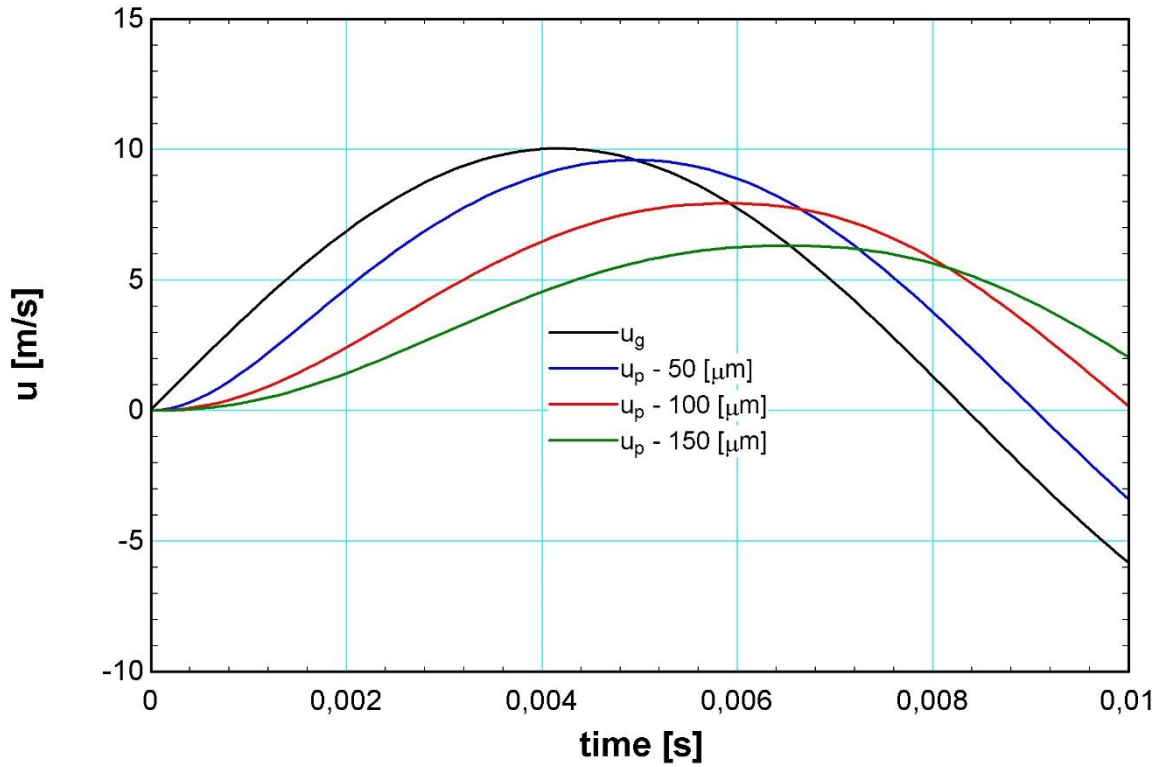


Figure 4.53 – Velocity, Case 3, $f = 60 \text{ Hz}$.

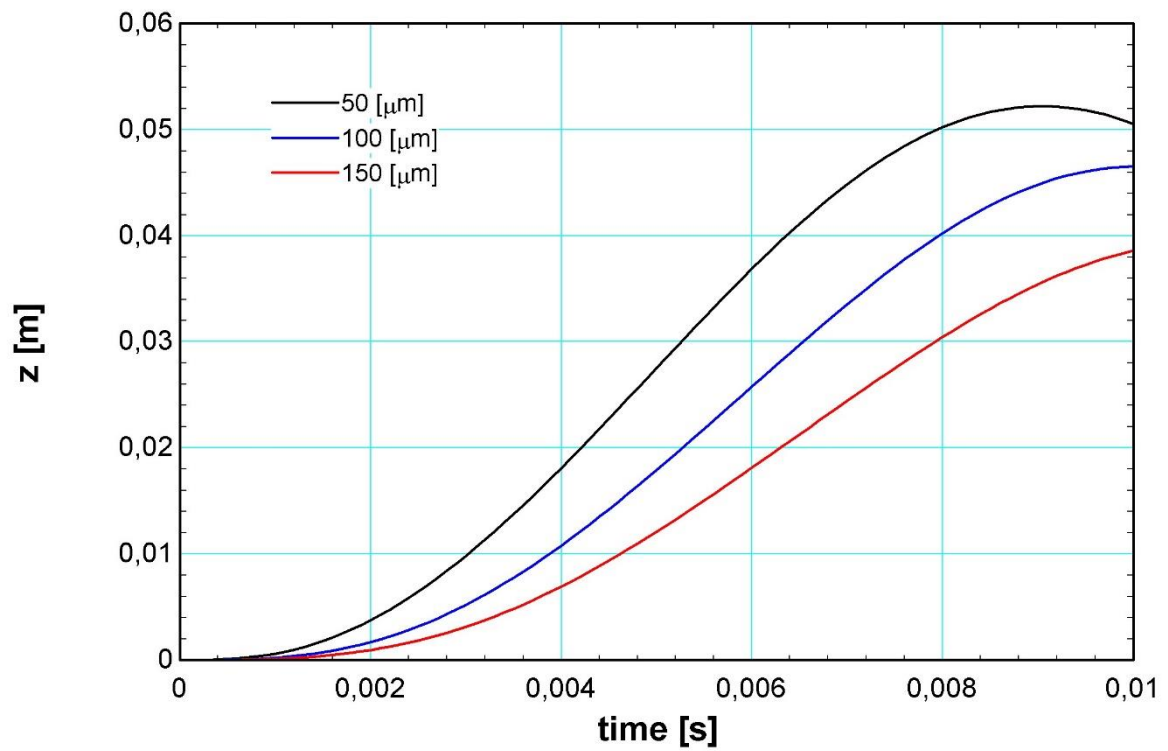


Figure 4.54 – Vertical displacement, Case 3, $f = 60 \text{ Hz}$.

Slower variations in the drying process, due to higher size particles, resulted in less intense Y_p reductions. These observations are described in figure 4.55.

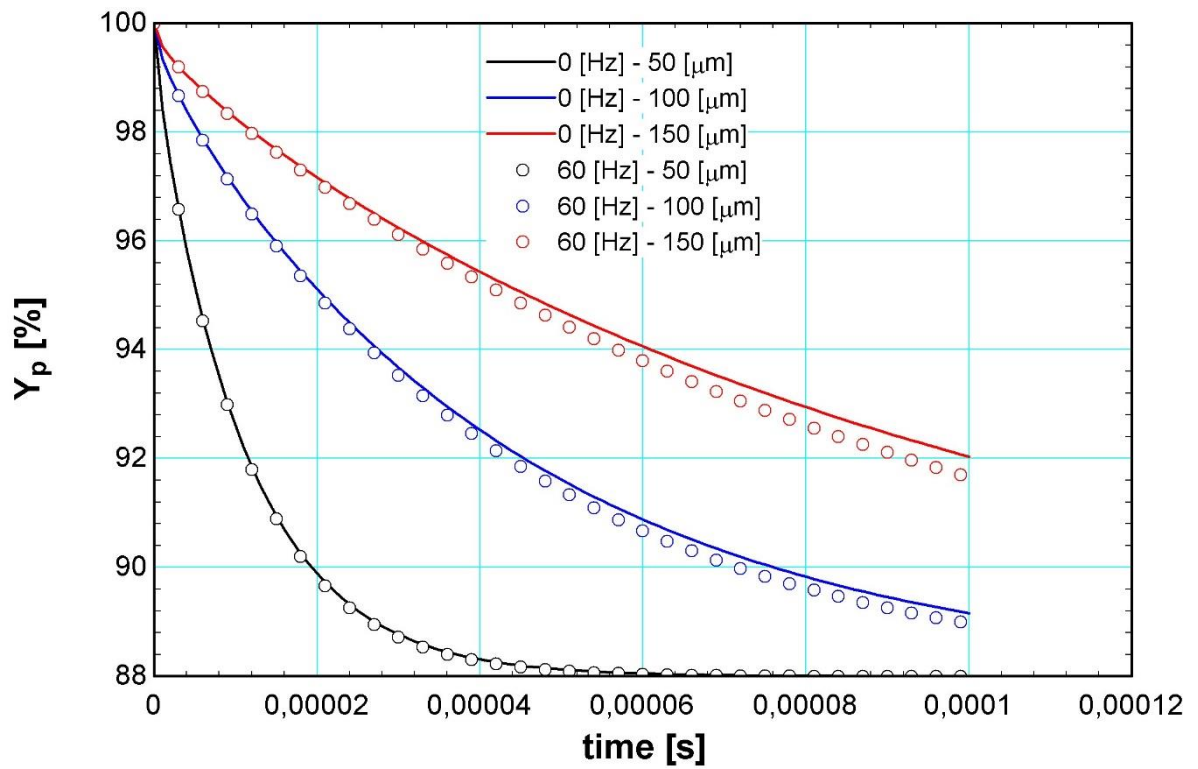


Figure 4.55 – Particle yield Y_p , Case 3.

The increase in particle size implied a decrease in biomass degradation rates. The values of Y_s varying as a function of particle sizes according to figures 4.56, 4.57 and 4.58.

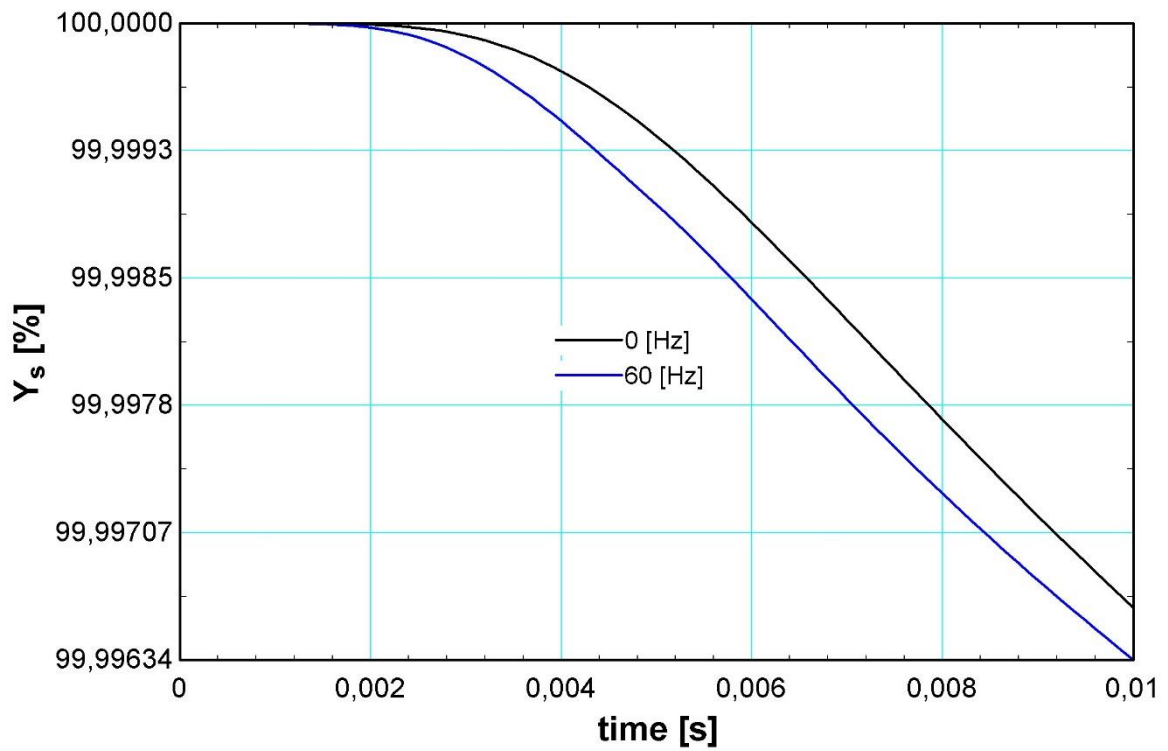


Figure 4.56 – Solid yield Y_s , Case 3, $d_p = 50 \mu m$.

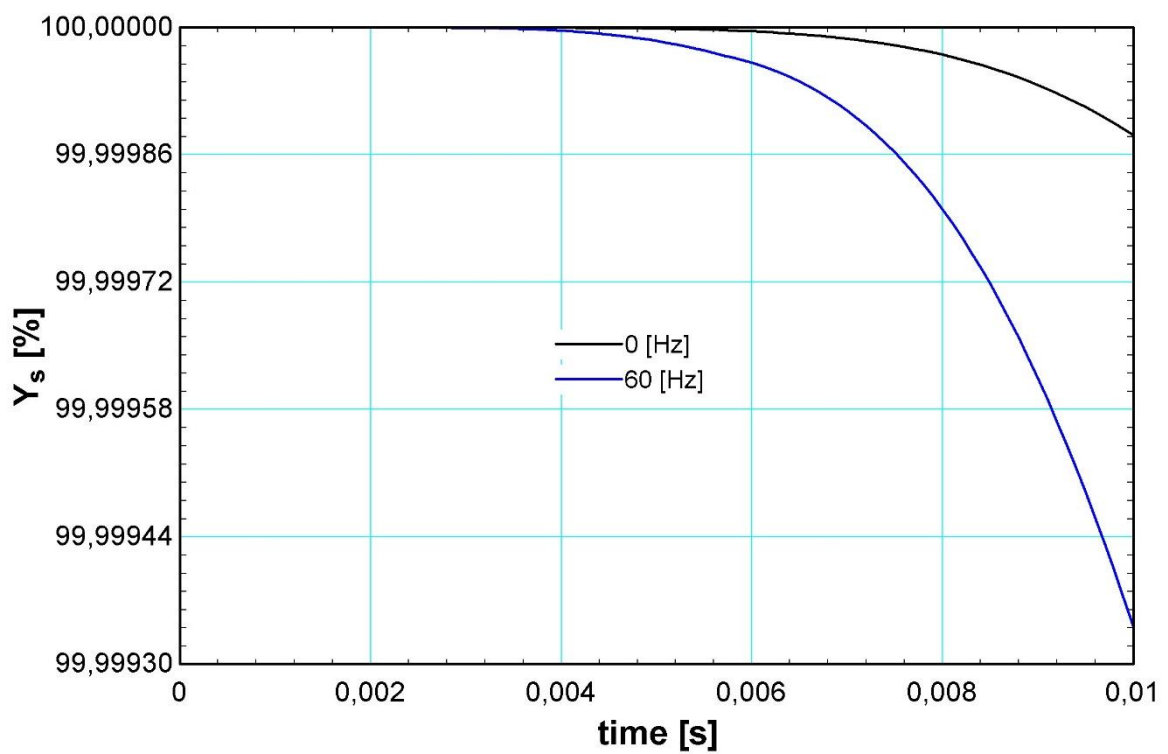


Figure 4.57 – Solid yield Y_s , Case 3, $d_p = 100 \mu m$.

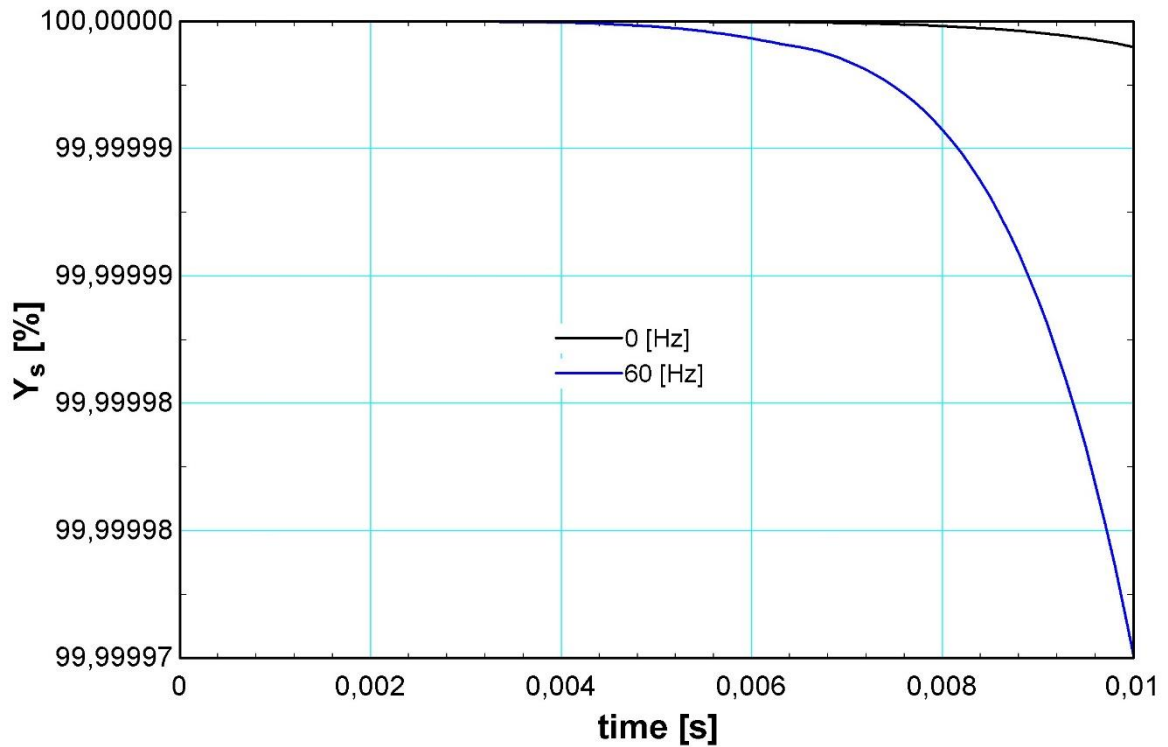


Figure 4.58 – Solid yield Y_s , Case 3, $d_p = 150 \mu m$.

The summary of all parameters analyzed in case 3, considering the observations and effects are in table 4.3.

Table 4.3 – Observations and effects for case 3.

Variable parameter: d_p [m]			
Parameter	Unit	Observation	Effect
C	kg/m^3	Drying rate	↓
h_m	m/s	Mass transfer	↓
T	K	Temperature change rate	↓
h_t	W/m^2K	Heat transfer	↓
u_p	m/s	Particle velocity	↓
z_p	m	Particle vertical displacement	↓
Y_p	%	Particle yield	↑
Y_s	%	Solid yield	↑

4.4 Case 4

Case 4 simulated the torrefaction of a particle of 100 μm , frequency of 60 Hz in the presence of an acoustic field in amplitude velocity of 10 m/s. The results were compared with the simulation of the same flow without the presence of oscillation. Residence time of 1000s is much higher than the scale where the effects of oscillation in the humidity and temperature concentration fields are observed.

Both drying is completed and the particle becomes isothermal in a very short period, so that no acoustic field effects are observed at C and T , which is why graphs were not prepared for these properties in case 4.

The value of h_m increased until drying ended as shown in figure 4.59. After that, the value starts to decrease, but at values much higher than those observed for flow without acoustic field. The increase in h_m varies in a range between 35% and 42%.

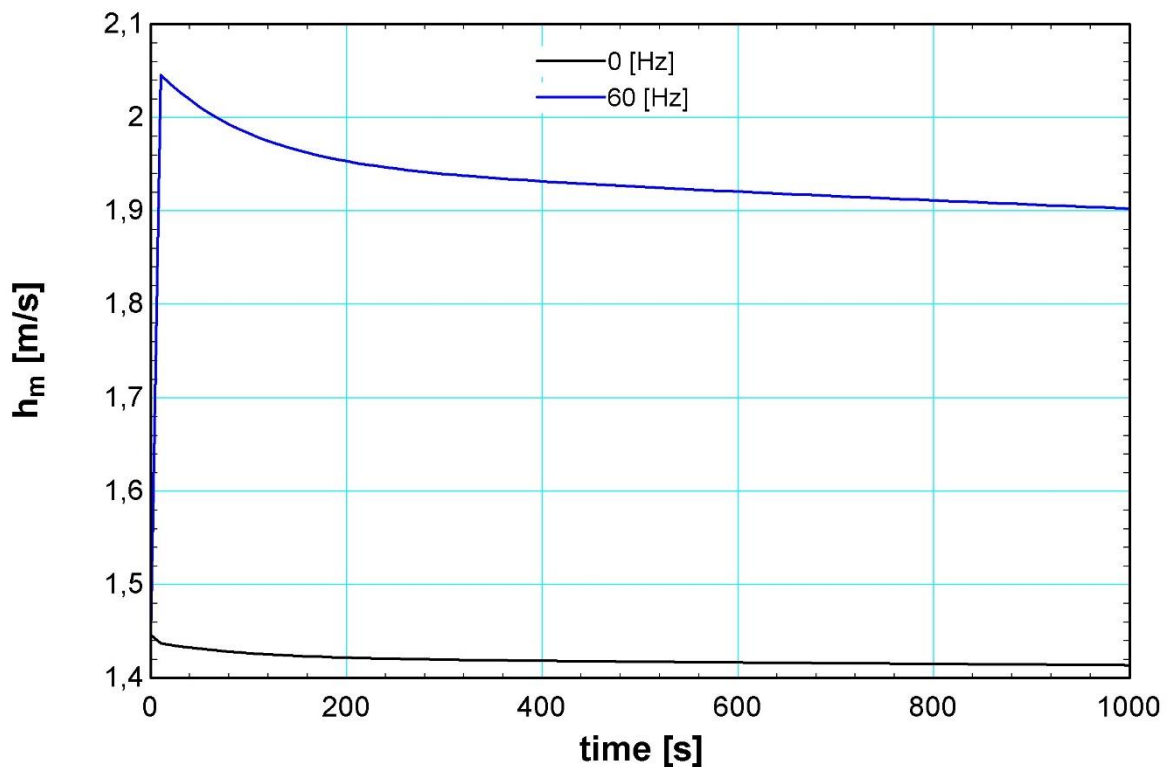


Figure 4.59 – Mass transfer coefficient, Case 4.

The value of h_t increased until the particle becomes isothermal as shown in figures 4.60. In the same way observed in h_m , the presence of the acoustic field keeps h_t values at much higher levels compared to the flow without acoustic field. Likewise, the increase in h_t varies in a range between 35% and 42%.

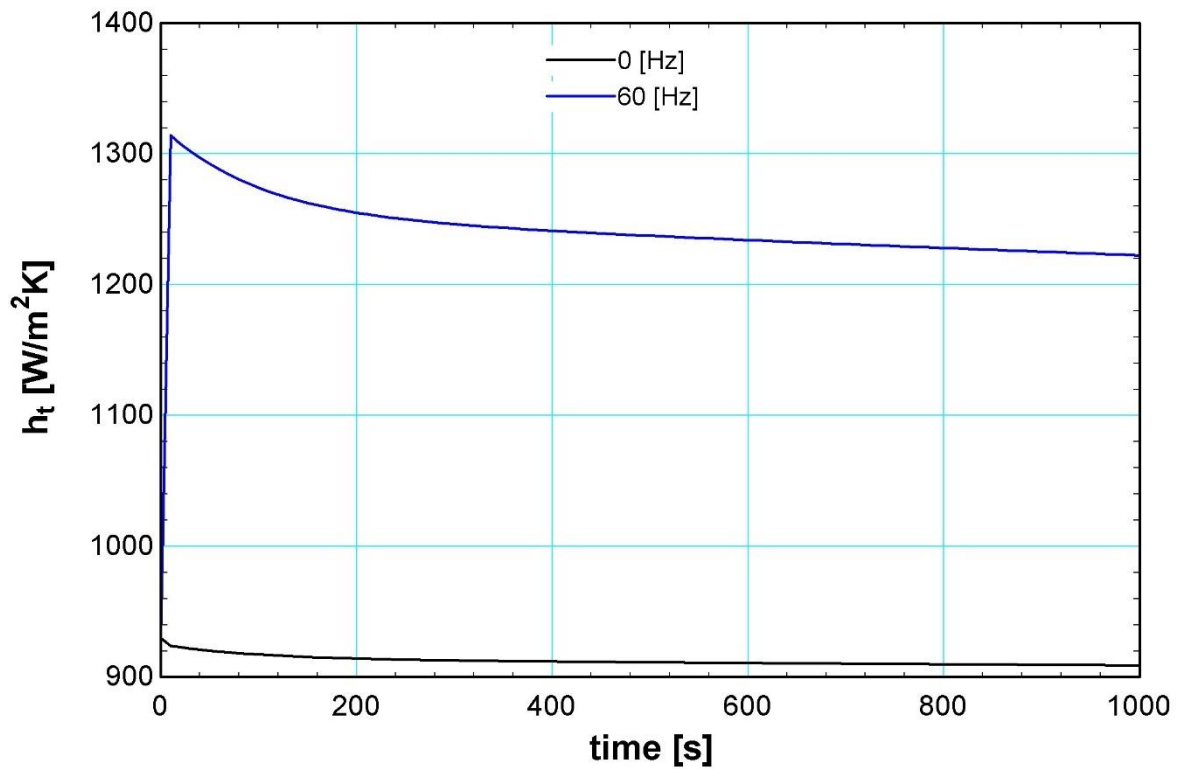


Figure 4.60 – Heat transfer coefficient, Case 4.

The presence of the acoustic field strongly interferes with the balance of forces, resulting in a resultant force that negatively accelerates the particle compared to the flow without acoustic field. This influence manifests itself in the particle's velocity profile as seen in Figure 4.61.

Until drying is complete, the fast mass variation influences the balance of forces until the velocity reaches a peak, when then the velocity begins to increase but slowly.

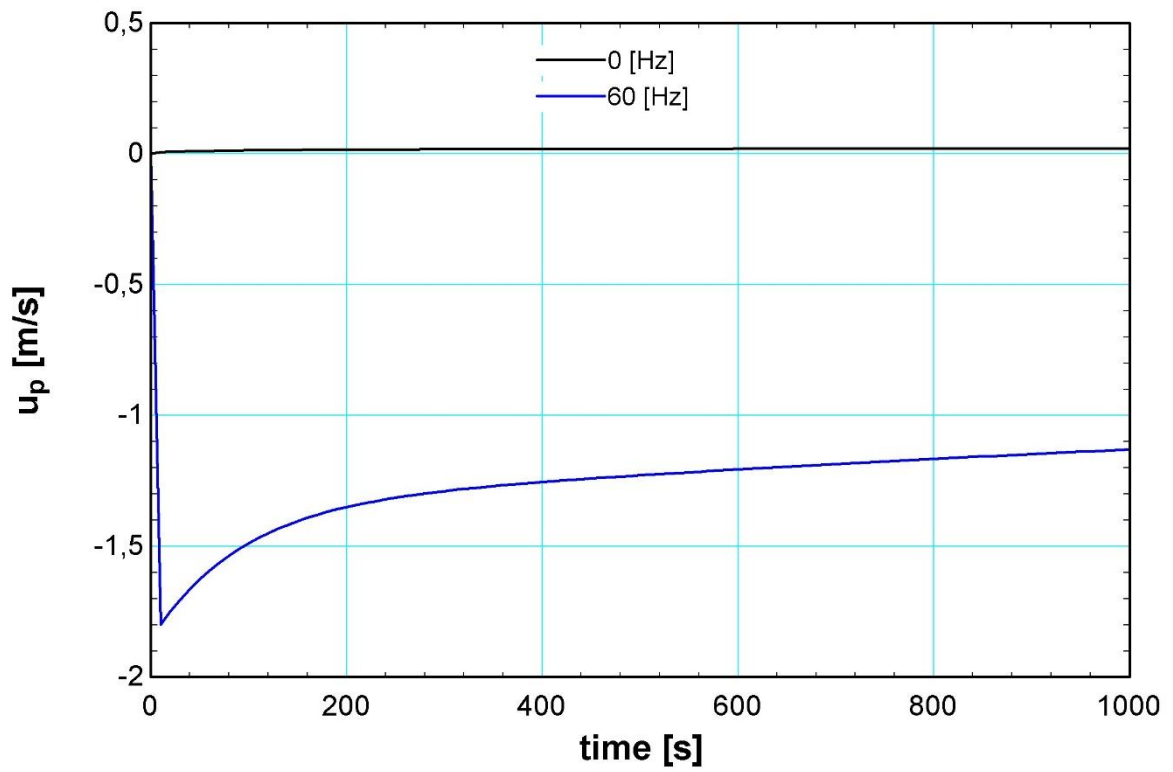


Figure 4.61 – Particle velocity, Case 4.

The occurrence of negative acceleration with the presence of the acoustic field implies a smaller vertical displacement for the particle, as can be seen in Figure 4.62.

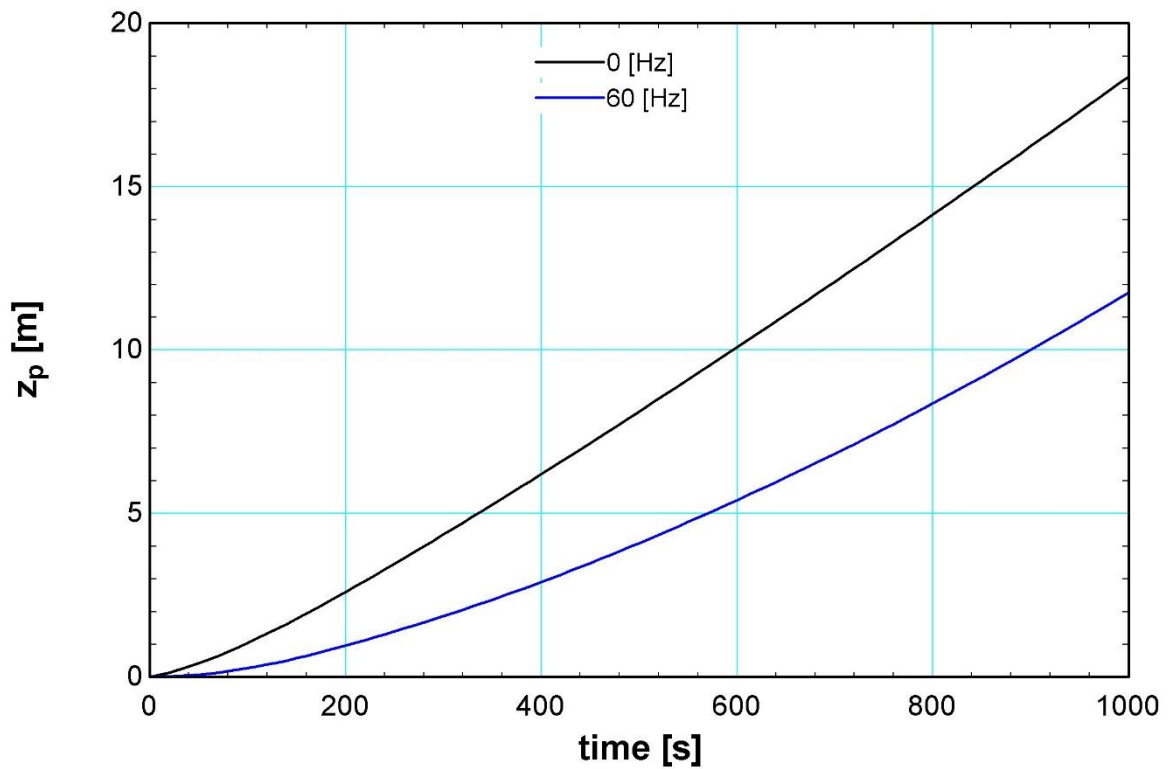


Figure 4.62 – Vertical displacement, Case 4.

For the adopted time scale, the change in mass expressed by Y_p does not derive only from drying but also from thermal degradation. This configuration of the two reduction mechanisms can now be seen in figure 4.63. The presence of the acoustic field does not influence property, given that for this time scale is essentially formed by the degradation term Y_s , which is a function of temperature and time.

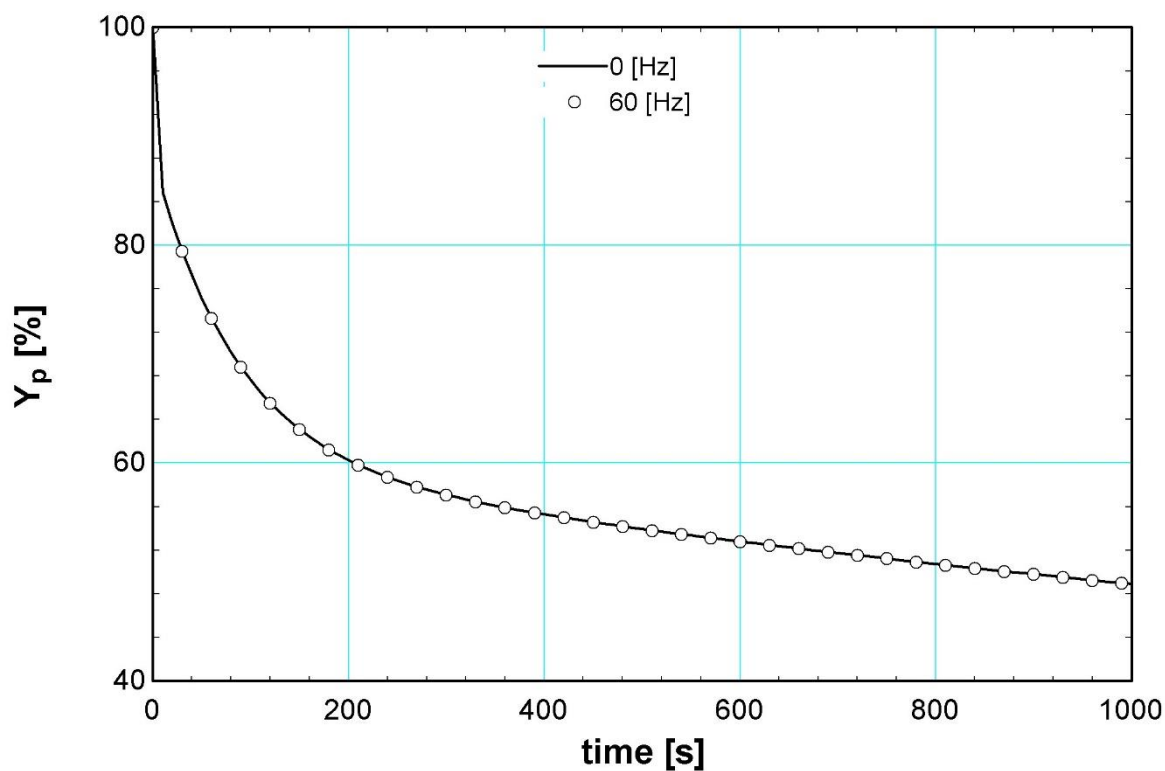


Figure 4.63 – Particle yield Y_p , Case 4.

In thermogravimetric analysis studies, the most common is to demonstrate the variation of the solid mass as a function of time. The solid mass reduction Y_s can be seen in figure 4.64. The acoustic field does not indicate interference in the process as explained in the variation of Y_p .

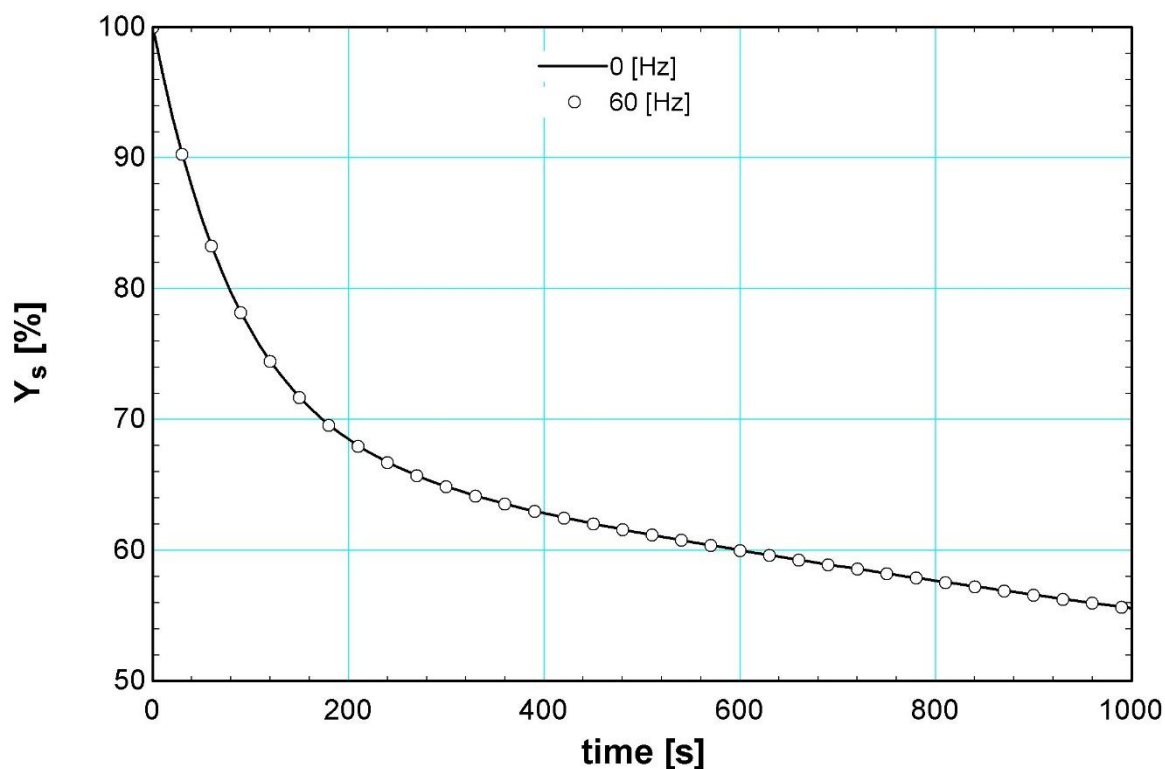


Figure 4.64 – Solid yield Y_s , Case 4.

The kinetic parameters described in Table 3.1 were used to predict the solid distribution using equations 35–39 during torrefaction as shown in figures 4.65 and 4.66. The figures show the conversion of the initial solid (A) into an intermediate solid (B) and finally into a solid (C).

The formation of the first and second volatiles are also presented. Figure 4.65 and 4.66 shows that the conservation of mass is obeyed such that the sum of the fractional composition of each component at any given time always equals 100%. The presence of the acoustic field did not cause interference in the process, due to the reasons already presented about the characteristic time analyzed.

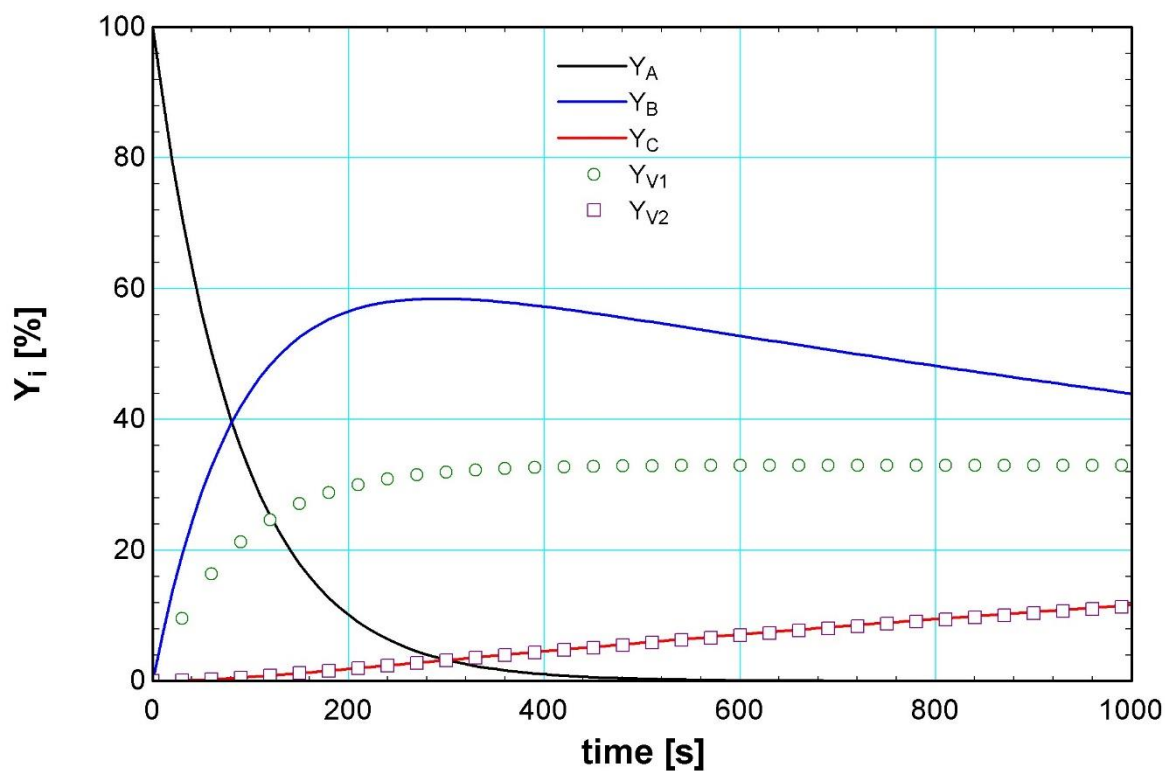


Figure 4.65 – Solid product yield Y_i ($i = A, B, C, V1, V2$), Case 4, 0 Hz.

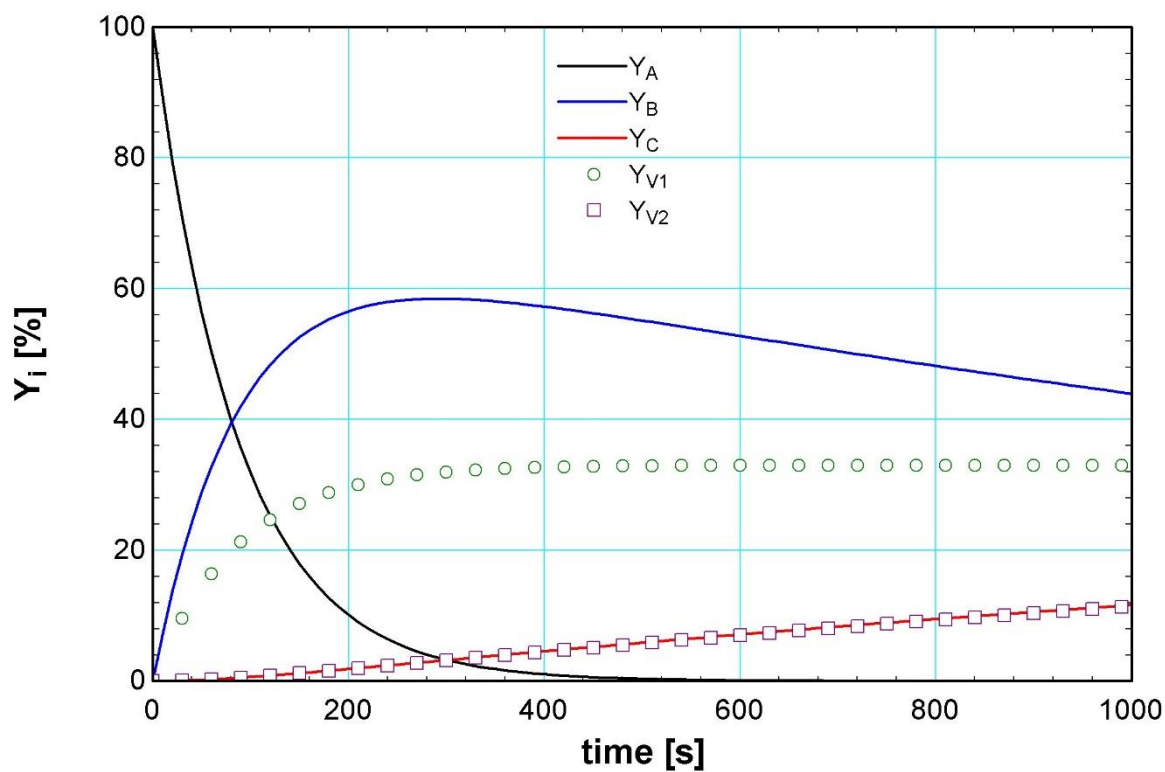


Figure 4.66 – Solid product yield Y_i ($i = A, B, C, V1, V2$), Case 4, 60 Hz.

Figure 4.67 illustrates the overall solid loss product composition with time. This composition profile is in line with the expected de-oxygenation of the solid product that occurs due to the decarboxylation and dehydration reactions. Also of importance is the relatively high carbon yield in the solid product throughout the process. The acoustic field did not cause interference in the product composition.

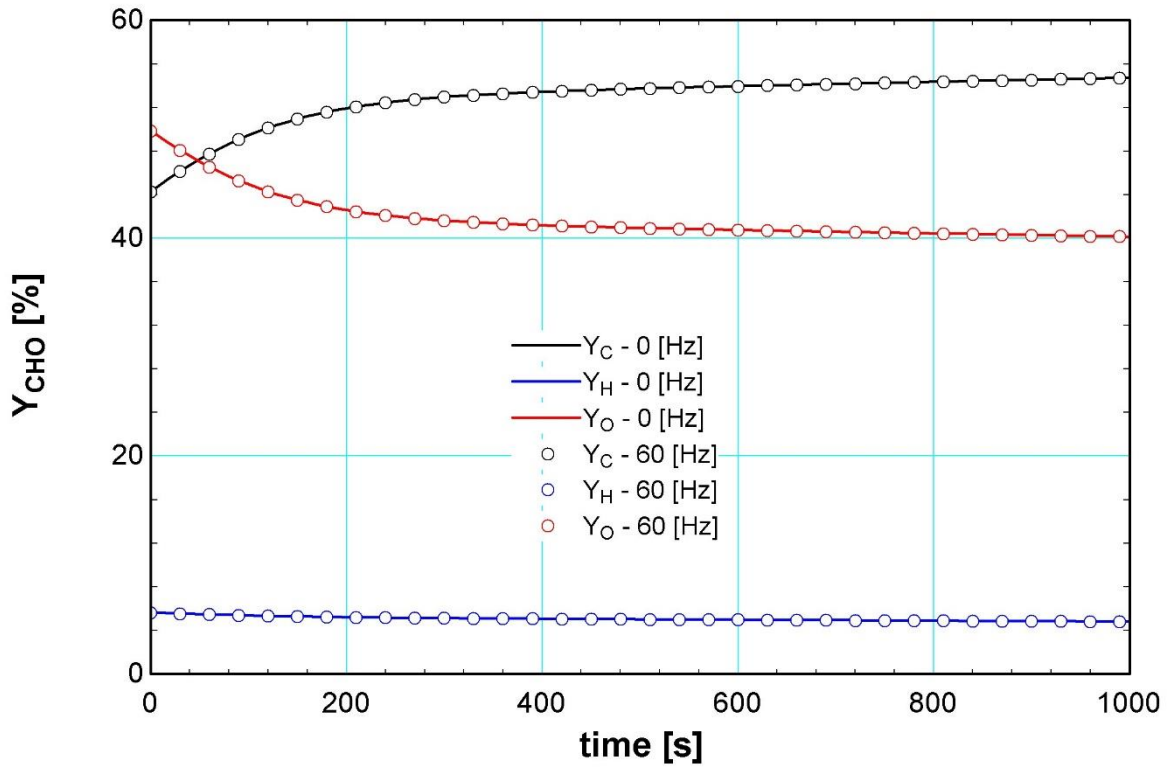


Figure 4.67 – Solid product composition yield Y_{CHO} , Case 4.

The HHV enhancement factor (EF) is calculated as Equation 59 and presented in Fig. 4.68. As shown in figures 4.65 and 4.66, the modification of the chemical composition of the biomass will improve its quality as an energy source, increasing energy density.

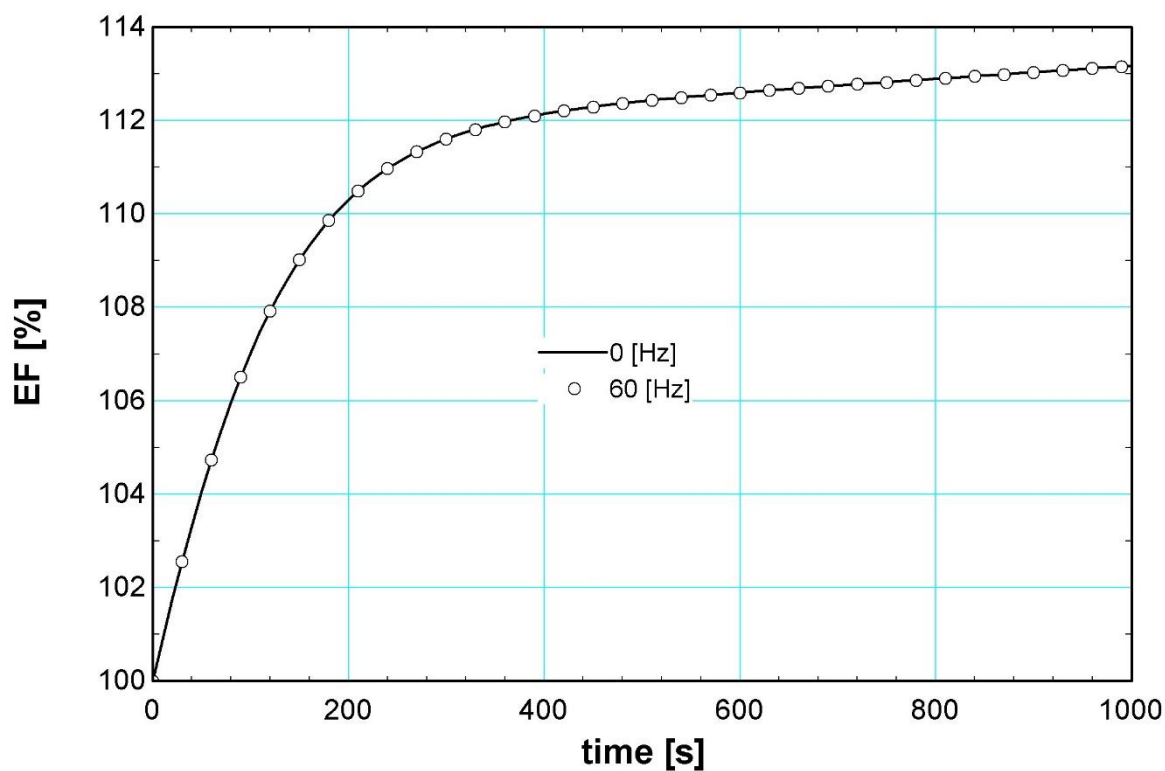


Figure 4.68 – HHV Enhancement Factor EF , Case 4.

Energy yield is 63% after 1000 s, as shown in Fig. 4.69. With these obtained results, it can be conducted with other information to optimize the biomass torrefaction process.

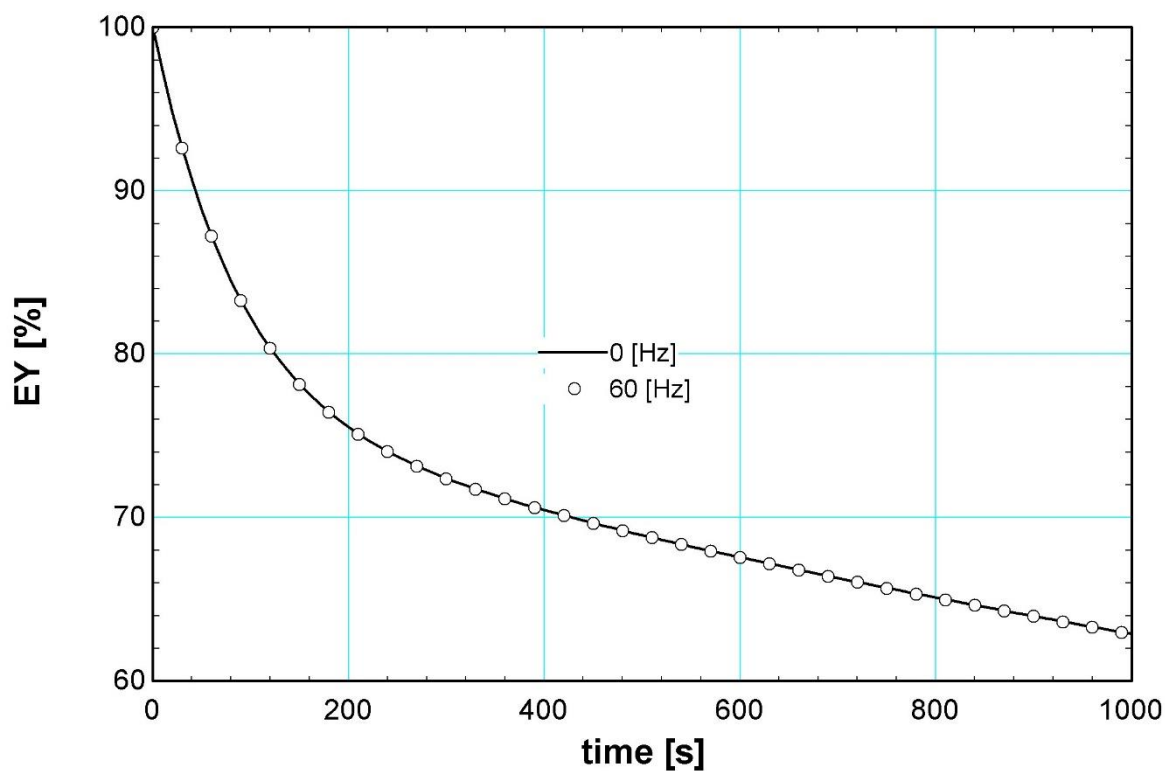


Figure 4.69 – Energy Yield *EY*, Case 4.

Considering the energy perspective of the solid, it is desirable to obtain a high energy yield at the smallest solid volume, to increase the efficiency of the process and benefit the transport of torrefaction products. The energy-mass co-benefit index (EMCI) shown in Figure 4.70 represents this optimal condition. For the analyzed biomass (*Eucalyptus Grandis*), the maximum value of EMCI was 7.63%, located in 420 seconds.

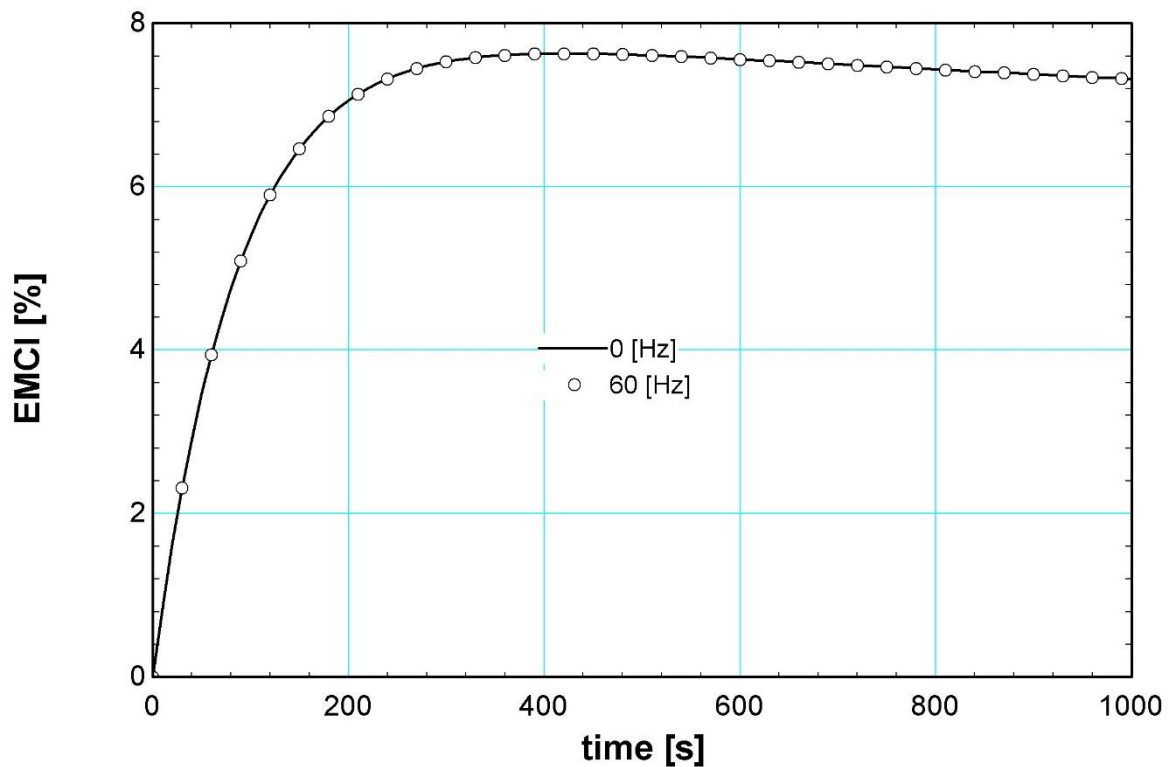


Figure 4.70 – Energy-Mass Co-benefit Index *EMCI*, Case 4.

4.5 Design specifications for a torrefaction reactor prototype

The presented proposal does not intend to go into configuration and sizing details, nor propose evaluations regarding performance parameters. The idea is to guide the construction of a prototype starting from the observations derived from the cases studied, especially considering the reach of the optimal point of the Energy-Mass Co-benefit Index (EMCI) shown on figure 4.70.

There are several configurations of reactors to carry out biomass pyrolysis, however fluidized bed reactors are the most commonly used, favored by their ease of operation and scalability. In a fluidized bed, the gravitational pull-on fluidized particles are offset by the upward fluid drag of the gas. This keeps the particles in a semi suspended condition [61].

A good understanding of the gas–solid motion in the reactor of a fluidized bed unit is very important. As the gas velocity through the solid particles increases, a series of changes in the motion of the particles could occur. At a sufficiently high velocity they are transported out of the vessel (Figure 4.71).

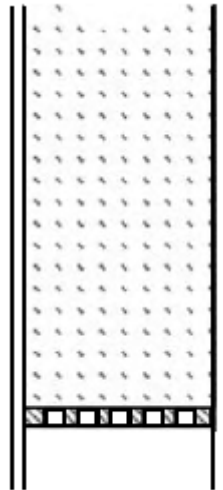


Figure 4.71 - A transport or entrained bed.

Considering the parameters adopted in the simulations, by classification criteria for solid gas contact processes (Table 4.4), the most appropriate definition for the present case is Transport bed (pneumatic or entrained bed).

Table 4.4 - Comparison of Principal Gas–Solid Contacting Processes.

Property	Packed Bed	Fluidized Bed	Fast Bed	Pneumatic Transport
Application in boilers	Stoker fired	Bubbling fluidized	Circulating fluidized	Pulverized coal fired
Mean particle diameter (mm)	< 300	0.03–3	0.05–0.5	0.02–0.08
Gas velocity through combustor zone (m/sec)	1–3	0.5–2.5	4–6	15–30
Typical U/U_t	0.01	0.3	2	40
Gas motion	Up	Up	Up	Up
Gas mixing	Near plug flow	Complex two phases	Dispersed plug flow	Near plug flow
Solids motion	Static	Up and down	Mostly up, some down	Up
Solid–solid mixing	Negligible	Usually near perfect	Near perfect	small
Overall voidage	0.4–0.5	0.5–0.85	0.85–0.99	0.98–0.998
Temperature gradient	Large	Very small	Small	Maybe significant
Typical bed-to-surface. Heat transfer coefficient, (W/m ² K)	50–150	200–550	100–200	50–100

From this section, it was possible to define an essential parameter of the prototype, which is the Overall voidage ε , as the fraction of the total volume which is free space available for the flow of fluids. Based on this definition, we can determine the mass flow rate of biomass \dot{m}_b that can be admitted to the reactor by Equation 71.

$$\dot{m}_b = (1 - \varepsilon) \frac{\rho_b}{\rho_g} \dot{m}_g \quad (71)$$

When the biomass enters the reactor, its temperature is initially raised to drying temperature T_d . The moisture evaporation process begins and heat transfer corresponds to sensible heat until drying Q_{sd} , calculated by the Equation 72.

$$Q_{sd} = \int_{T_0}^{T_d} c_p dT \quad (72)$$

Moisture vaporization occurs in an isothermal process and the latent heat of drying Q_{ld} is calculated in terms of biomass moisture concentration X_0 and enthalpy of vaporization of water $h_{v,H2O}$ by Equation 73.

$$Q_{ld} = X_0 h_{v,H2O} \quad (73)$$

After the end of drying, the temperature of the biomass is elevated until the degradation process begins. During this endothermic process, the sensible heat of pyrolysis Q_{sp} is calculated by Equation 74.

$$Q_{sp} = \int_{T_d}^{T_\infty} c_p dT \quad (74)$$

When the biomass reaches the thermal degradation process, the reactions occur in an isothermal process and the latent heat of pyrolysis Q_{lp} is calculated in terms of the enthalpy of pyrolysis h_p by Equation 75.

$$Q_{lp} = (1 - X_0) h_p \quad (75)$$

The sum of all heat transfer processes \dot{Q} results in the power required to process the biomass torrefaction according to Equation 76

$$\dot{Q} = \dot{m}_b \cdot (Q_{sd} + Q_{ld} + Q_{sp} + Q_{lp}) \quad (76)$$

Knowing the necessary energy demand to carry out the torrefaction, it is possible to use the biomass itself as fuel to supply the heat. The mass supply to be burned \dot{m}_{bb} is calculated by the equation 77.

$$\dot{m}_{bb} = \frac{\dot{Q}}{HHV_b} \quad (77)$$

From these calculations, the main design parameters are extracted for the construction of a prototype to process biomass torrefaction under the influence of an acoustic field. The design parameters are summarized in table 4.5.

Table 4.5 – Prototype parameters

<i>Parameter</i>	<i>Value</i>	<i>Unity</i>
<i>Biomass</i>	<i>Eucalyptus Grandis</i>	–
d_r	4	<i>m</i>
z_r	3,2	<i>m</i>
\tilde{u}_g^1	9,77	<i>m/s</i>
f	60	<i>Hz</i>
T_0	298,2	<i>K</i>
T_d	373,2	<i>K</i>
T_∞	573,2	<i>K</i>
C_∞	0	<i>kg/m³</i>
P_∞	1	<i>atm</i>
ρ_b	166,7[62]	<i>kg/m³</i>
X_0	0,08[63]	–
ρ_g^2	0,6158	<i>kg/m³</i>
\dot{m}_g	0,31	<i>kg/s</i>
ε	0,99	–
\dot{m}_b	0,84 79,9	<i>kg/s</i> <i>ton/day</i>
$h_{v,H2O}$	$2,26 \times 10^6$	<i>J/kg</i>
h_p^3	$1,46 \times 10^6$ [63]	<i>J/kg</i>
Q_{sd}	106134	<i>J/kg</i>
Q_{ld}	180503	<i>J/kg</i>
Q_{sp}	367501	<i>J/kg</i>
Q_{lp}	$1,34 \times 10^6$	<i>J/kg</i>
\dot{Q}	1676	<i>kW</i>
HHV_b	18070	<i>kJ/kg</i>
\dot{m}_{bb}	0,093	<i>kg/s</i>

1 – Calculated from equations [4-6], with manufacturer data [64]

2 – Considered as density of air

3 – Enthalpy of pyrolysis adopted was of Oak, which is a hardwood like Eucalyptus

The daily processing capacity was calculated to be 80 tons per day. This value is compatible with the production of a local logging region [65], indicating that its application could be directed to a real case study in Brazil.

5 CONCLUSIONS

The torrefaction of a single biomass particle in the presence of an oscillating flow is investigated in order to understand the detailed effects of acoustic fields on drying and thermal degradation. The effects of property variation, the intensity of an acoustic field, the frequency and the particle size on the torrefaction of a single particle has been explored.

Increasing frequency or amplitude velocity of acoustic field increases heat and mass transfer from biomass particle, compared to the case with no oscillating flow velocity.

The effect of acoustic field is also more pronounced as the particle diameter increases.

In this work it has been shown that, high intensity acoustic field application induces an oscillating slip velocity over biomass particles, augmenting heat and mass transfer rates. Increased heat and mass transfer rates results in the enhancement of the degradation rate. Application of acoustic field is expected to lead to shorter reactors compared to the conventional ones with the same capacity.

The dimensioning of the reactor based on the concept proposed by EMCI offers an optimized treatment of biomass residues, providing the best relationship between energy densification and volume reduction.

In order to expand the level of understanding of the process of heat and mass transfer and torrefaction of biomass particles in the presence of an oscillating flow field, it is recommended to develop a prototype of a torrefaction unit from specifications resulting from simulations using Eucalyptus as raw material.

REFERENCES

- [1] POTENCIAL DE RESÍDUOS DE BIOMASSA NO BRASIL. Instituto Brasileiro Pellets Biomassa Briquete, 2002. Available in: <https://abibbrasil.wixsite.com/institutobpellets/potencial-biomassa-brasil>. Access in: 09/16/2022.
- [2] EPE [Empresa de Pesquisa Energética] Balanço Energético Nacional (BEN) 2022: Ano base 2021, 2022. Available in: <https://www.epe.gov.br/sites-pt/publicacoes-dados-abertos/publicacoes/PublicacoesArquivos/publicacao-675/topico-638/BEN2022.pdf>. Access in: 09/16/2022.
- [3] EPE [Empresa de Pesquisa Energética] Plano Decenal de Expansão de Energia (PDE2030) 2030: Ano base 2021, 2030. Available in: https://www.epe.gov.br/sites-pt/publicacoes-dados-abertos/publicacoes/PublicacoesArquivos/publicacao-490/PDE%202030_RevisaoPosCP_rv2.pdf. Access in: 09/17/2022.
- [4] Veras Carlos A G, Carvalho Jr João A and Ferreira Marco A. The Chemical Percolation Devolatilization Model Applied to the Devolatilization of Coal in High Intensity Acoustic Fields. *Journal of the Brazilian Chemical Society*, v. 13, n. 3, p. 358–367, 2002.
- [5] Ha, Man Yeong. A Theoretical Study of Augmentation of Particle Combustion Via Acoustic Enhancement of Heat And Mass Transfer. Pennsylvania State University, 1990.
- [6] Ha, M.Y., Yavuzkurt, S., Koopmann, G. and Scaroni, A.W., 1989, "Modeling the Effects of High Intensity Acoustic Fields on the Enhancement of Heat and Mass Transfer from Spheres," 1989 National Heat Transfer Conference, HTD Vol 109, Multiphase Flow, Heat and Mass Transfer, pp. 133-140, Philadelphia, August 6-9.
- [7] Y. Niu, Y. Lv, Y. Lei, S. Liu, Y. Liang, D. Wang, S. Hui, Biomass torrefaction: properties, applications, challenges, and economy, *Renew. Sustain. Energy Rev.* 115, 2019.
- [8] M.N. Cahyanti, T.R.K.C. Doddapaneni, T. Kikas, Biomass torrefaction: an overview on process parameters, economic and environmental aspects and recent advancements, *Bioresour. Technol.* 301, 2020.
- [9] Y.C. Chen, W.H. Chen, B.J. Lin, J.S. Chang, H.C. Ong, Impact of torrefaction on the composition, structure and reactivity of a microalga residue, *Appl. Energy* 181, 2016, 110-119.
- [10] K. Jagodzińska, M. Czerep, E. Kudlek, M. Whukowski, W. Yang, Torrefaction of wheat-barley straw: composition and toxicity of torrefaction condensates, *Biomass Bioenergy* 129, 2019.
- [11] P. Nanou, M.C. Carbo, J.H.A. Kiel, Detailed mapping of the mass and energy balance of a continuous biomass torrefaction plant, *Biomass Bioenergy* 89, 2016, 67-77.

- [12] Z. Ma, J. Wang, C. Li, Y. Yang, X. Liu, C. Zhao, D. Chen, New sight on the lignin torrefaction pretreatment: relevance between the evolution of chemical structure and the properties of torrefied gaseous, liquid, and solid products, *Bioresour. Technol.* 288, 2019.
- [13] R.B. Bates, A.F. Ghoniem, Modeling kinetics-transport interactions during biomass torrefaction: the effects of temperature, particle size, and moisture content, *Fuel* 137, 2014, 216–229.
- [14] B.J. Lin, E.A. Silveira, B. Colin, W.H. Chen, A. P´etrissans, P. Rousset, M. P´etrissans, Prediction of higher heating values (HHVs) and energy yield during torrefaction via kinetics, 10th Int. Conf. Appl. Energy, 2019, 111-116.
- [15] X. Tian, L. Dai, Y. Wang, Z. Zeng, S. Zhang, L. Jiang, X. Yang, L. Yue, Y. Liu, R. Ruan, Influence of torrefaction pretreatment on comcobs: a study on fundamental characteristics, thermal behavior, and kinetic, *Bioresour. Technol.* 297, 2020.
- [16] K.Q. Tran, S. Werle, T.T. Trinh, A. Magdziarz, S. Sobek, M. Pogrzeba, Fuel characterization and thermal degradation kinetics of biomass from phytoremediation plants, *Biomass Bioenergy* 134, 2020.
- [17] S. Zhang, S. Zhu, H. Zhang, X. Liu, H. Zhang, Evaluation of pyrolysis behavior and products properties of rice husk after combined pretreatment of washing and torrefaction, *Biomass Bioenergy* 127, 2019.
- [18] B.-J. Lin, E.A. Silveira, B. Colin, W.-H. Chen, Y.-Y. Lin, F. Leconte, A. P´etrissans, P. Rousset, M. P´etrissans, Modeling and prediction of devolatilization and elemental composition of wood during mild pyrolysis in a pilot-scale reactor, *Ind. Crop. Prod.* 131, 2019, 357-370.
- [19] E.A. Silveira, B.J. Lin, B. Colin, M. Chaouch, A. P´etrissans, P. Rousset, W.H. Chen, M. P´etrissans, Heat treatment kinetics using three-stage approach for sustainable wood material production, *Ind. Crop. Prod.* 124, 2018, 563-571.
- [20] R.B. Bates, A.F. Ghoniem, Biomass torrefaction: modeling of reaction thermochemistry, *Bioresour. Technol.* 134, 2013, 331-340.
- [21] R.B. Bates, A.F. Ghoniem, Biomass torrefaction: modeling of volatile and solid product evolution kinetics, *Bioresour. Technol.* 124, 2012, 460-469.
- [22] C. Di Blasi, M. Lanzetta, Intrinsic kinetics of isothermal xylan degradation in inert atmosphere, *J. Anal. Appl. Pyrolysis* 40-41, 1997, 287-303.
- [23] S. Ren, H. Lei, L. Wang, Q. Bu, S. Chen, J. Wu, Thermal behaviour and kinetic study for woody biomass torrefaction and torrefied biomass pyrolysis by TGA, *Biosyst. Eng.* 116, 2013, 420-426.
- [24] M.J. Prins, K.J. Ptasinski, F.J.J.G. Janssen, Torrefaction of wood. Part 1. Weight loss kinetics, *J. Anal. Appl. Pyrolysis* 77, 2006, 28-34.

- [25] M.J. Prins, K.J. Ptasinski, F.J.J.G. Janssen, Torrefaction of wood. Part 2. Analysis of products, *J. Anal. Appl. Pyrolysis* 77, 2006, 35-40.
- [26] J.J. Chew, V. Doshi, S.T. Yong, S. Bhattacharya, Kinetic study of torrefaction of oil palm shell, mesocarp and empty fruit bunch, *J. Therm. Anal. Calorim.* 126, 2016, 709–715.
- [27] Q.V. Bach, W.H. Chen, Y.S. Chu, Ø. Skreiberg, Predictions of biochar yield and elemental composition during torrefaction of forest residues, *Bioresour. Technol.* 215, 2016, 239-246.
- [28] T. Khazraie Shoulaifar, N. Demartini, O. Karlström, J. Hemming, M. Hupa, Impact of organically bonded alkali metals on torrefaction: Part 2, Modeling, *Fuel* 168, 2016, 107-115.
- [29] T. Khazraie Shoulaifar, N. Demartini, O. Karlström, M. Hupa, Impact of organically bonded potassium on torrefaction: part 1, Experimental, *Fuel* vol. 165, 2016, 544–552.
- [30] L. Shang, J. Ahrenfeldt, J.K. Holm, L.S. Bach, W. Stelte, U.B. Henriksen, Kinetic model for torrefaction of wood chips in a pilot-scale continuous reactor, *J. Anal. Appl. Pyrolysis* 108, 2014, 109–116.
- [31] L. Shang, J. Ahrenfeldt, J.K. Holm, S.S. Barsberg, R.Z. Zhang, Y.H. Luo, H. Egsgaard, U.B. Henriksen, Intrinsic kinetics and devolatilization of wheat straw during torrefaction, *J. Anal. Appl. Pyrolysis* 100, 2013, 145-152.
- [32] S. Gul, N. Ramzan, M.A. Hanif, S. Bano, Kinetic, volatile release modeling and optimization of torrefaction, *J. Anal. Appl. Pyrolysis* 128, 2017, 44-53.
- [33] Q. Nguyen, D.D. Nguyen, H. Voithi, C. He, M. Goodarzi, Q.V. Bach, Isothermal torrefaction kinetics for sewage sludge pretreatment, *Fuel* 277, 2020.
- [34] Edgar A. Silveira, Sandra M. Luz, Rosineide M. Leão, Patrick Rousset, Armando Caldeira-Pires, Numerical modeling and experimental assessment of sustainable woody biomass torrefaction via coupled TG-FTIR, *Biomass and Bioenergy*, Volume 146, 2021.
- [35] K.M. Lu, W.J. Lee, W.H. Chen, S.H. Liu, T.C. Lin, Torrefaction and low temperature carbonization of oil palm fiber and eucalyptus in nitrogen and air atmospheres, *Bioresour. Technol.* 123, 2012, 98-105.
- [36] LRZ Ltd., 1993. Downdraft Gasifiers under 200 kW_e. ETSU, B/M3/00388/04/Rep.
- [37] Natural Resources Institute, 1996. Decentralised Production of Electricity from Biomass. ETSU, B/T1/00351/Rep.
- [38] IUPAC. Compendium of Chemical Terminology, 2nd ed. (the "Gold Book"). Compiled by A. D. McNaught and A. Wilkinson. Blackwell Scientific Publications, Oxford (1997). Online version (2019-) created by S. J. Chalk. ISBN 0-9678550-9-8. <https://doi.org/10.1351/goldbook>.

- [39] A. Demirbas. Biomass resource facilities and biomass conversion processing for fuels and chemicals
Energy Convers Manage, 42 (2001), pp. 1357-1378.
- [40] J.J. Manya, E. Velo, L. Puigjaner. Kinetics of biomass pyrolysis: a reformulated three-parallel-reactions model. Ind Eng Chem Res, 42 (2003), pp. 434-441.
- [41] G. Varhegyi, J.J.M. Antal, E. Jakab, P. Szabo. Kinetic modeling of biomass pyrolysis. J Anal Appl Pyrolysis, 42 (1997), pp. 73-87.
- [42] K. Raveendran, A.K. Ganesh, C. Khilar. Influence of mineral matter on biomass pyrolysis characteristics. Fuel, 74 (1995), pp. 1812-1822.
- [43] H.P. Yang, R. Yan, T. Chin, D.T. Liang, H.P. Chen, C.G. Zheng. TGA-FTIR analysis of palm oil wastes pyrolysis. Energy Fuel, 18 (2004), pp. 1814-1821.
- [44] K. Raveendran, A. Ganesh, K.C. Khilar. Pyrolysis characteristics of biomass and biomass components. Fuel, 75 (1996), pp. 987-998.
- [45] Coombs, J., 1996. Bioconversion Assessment Study. CPL Scientific Ltd, UK (Air – CT92 – 8007).
- [46] EU, 1999. Biomass Conversion Technologies. EUR 18029 EN ISBN 92-828-5368-3.
- [47] M.J.C. van der Stelt, H. Gerhauser, J.H.A. Kiel, K.J. Ptasinski, Biomass upgrading by torrefaction for the production of biofuels: A review, Biomass and Bioenergy, Volume 35, Issue 9, 2011, 3748-3762.
- [48] Hankalin, Ville & Ahonen, Tuukka & Raiko, Risto. (2009). On thermal properties of a pyrolysing wood particle.
- [49] Ranz W, Marshall W. Evaporation from drops. Chemical Engineering Progress, 1952.
- [50] Bruce E. Poling, John M. Prausnitz, John P. O'Connell The Properties Of Gases and Liquids 5E, McGraw Hill Professional, (2000) - 768p.
- [51] Wheeler A, Advances in catalysis, vol. III. New York: Academic Press; 1951. p. 250.
- [52] C. Sheng, J.L.T. Azevedo, Estimating the higher heating value of biomass fuels from basic analysis data, Biomass Bioenergy 28 (2005) 499–507.
- [53] S.M. Lee, J.-W. Lee Optimization of biomass torrefaction conditions by the gain and loss method and regression model analysis Bioresour. Technol., 172 (2014), pp. 438-443.
- [54] Thibault J, Bergeron S, Bonin H. On finite-difference solutions of the heat equation in spherical coordinates. May, 1987.
- [55] The Wood Database. Specifications of Eucalyptus Grandis. Available in: <https://www.wood-database.com/rose-gum/>. Access in: 11/08/2022.

- [56] Thompson, W. S.; Darwin, W. N. 1968. Weight, Volume, and Moisture Content of Sawdust from Selected Southern Species. *Forest Products Journal* September p. 96.
- [57] EES, 2022. Engineering Equation Solver, F-Chart Software, accessed 8 April 2022. <http://www.fchart.com/ees/>.
- [58] Nellis G, Klein S. *Heat Transfer*. 1st ed. New York: Cambridge; 2008.
- [59] Anse AMC, Westerhout RWJ, Prins W. Modelling of flash pyrolysis of a single wood particle. *Chem Eng Process* 2000;39:239–52.
- [60] Pure World Energy. Specifications of C30 Capstone Microturbine. Available in: <https://www.pureworldenergy.com/technology/capstone-products/c30-capstone-microturbine/>. Access in: 01/03/2023.
- [61] Basu, P. (2006). *Combustion and Gasification in Fluidized Beds* (1st ed.). CRC Press. <https://doi.org/10.1201/9781420005158>.
- [62] The Wood Database. Specifications of Pinus Pinaster. Available in: <https://www.wood-database.com/maritime-pine/>. Access in: 11/08/2022.
- [63] Daren E. Daugaard and Robert C. Brown . Enthalpy for Pyrolysis for Several Types of Biomass. *Energy & Fuels* 2003 17 (4), 934-939. DOI: 10.1021/ef020260x
- [64] Made in China. Specifications of Ms-590 Industrial Double Electric Motor Siren. Available in: <https://shuntongdq.en.made-in-china.com/product/tMwJkCpuhyar/China-Ms-590-Industrial-Double-Electric-Motor-Siren.html>. Access in: 02/01/2023.
- [65] Dessbesell, L. Viabilidade Econômica do Aproveitamento Energético da Serragem na Bacia Hidrográfica do Rio Pardo . 2014. 76p.